NTNU – Trondheim
Norwegian University of
Science and Technology

Preservation of Low Frequencies in Broadband Data Processing

Vegard Dahl-Eriksen

Petroleum Geoscience and Engineering
Submission date: June 2014
Supervisor: Martin Landrø, IPT

Norwegian University of Science and Technology
Department of Petroleum Engineering and Applied Geophysics

Preface

This master's thesis was executed for the Department of Applied Geophysics and Petroleum Technology at the Norwegian University of Science and Technology (NTNU) in collaboration with the geoscience company CGG. It was written the spring of 2014 with guidance of the seismic processors in CGG, Erik Hicks and Henning Hoeber, together with Professor Martin Landrø at NTNU.

The problem description was developed by CGG and relates to the recent broadband technology advances in the seismic industry. Processing of such data introduce challenges in how to preserve the broader bandwidth in both the low and high end. As processes and operators in broadband processing generally are applied on full bandwidth data, the isolated low frequency response is not well known. This thesis focuses on how the lowest frequencies react to the different processing modules. The primary goal was to identify possible problems and compare processing methods to conclude with an optimized processing flow that favours the lowest frequencies. Full bandwidth data existed and was low-pass filtered for a direct comparison throughout the different processing stages.

I would like to thank Statoil for letting me work with the ST12018 Sleipner dataset and CGG for investing in the thesis. A huge thanks goes to my main supervisor in CGG, Erik Hicks, for all the hours spent on teaching and discussing. It has been of invaluable importance for the progress made. I will also thank Henning Hoeber and Martin Landrø for always having the answers to my questions and for valuable input during my work. Discussions with Vetle Vinje and Thomas Elboth have also been highly appreciated. My last thank goes to my friends and fellow students for keeping me at good spirit and motivated through the studies that this thesis concludes.

Trondheim, June 2014 Vegard Dahl-Eriksen

Abstract

Recent developments in the seismic industry have introduced data with a broader frequency content than before. Broadband seismic data has led to challenges in the processing since the majority of the available algorithms and techniques were written for the conventional seismic range. This thesis attacks the low frequency response in each of the steps in a seismic processing flow. Some steps were both expected and found to perform well, while others needed comprehensive testing.

The research was carried out by processing two datasets with different high-cut frequencies. The first dataset was low-pass filtered with a high-cut frequency of 10 Hz, while the other dataset was obtained with a high-cut frequency of 20 Hz. A full bandwidth reference dataset was used for comparisons. This dataset was commercially processed by CGG in 2012-2013 with what can be regarded as a modern broadband processing sequence.

The denoise step was found to be improved by extending the window that removes the noise. This is an important observation as the low frequencies in general have a lower signal-to-noise ratio than the higher frequencies. In addition, more noise removed at an early stage may provide cleaner execution in other processing routines. However, the main challenge related to the low frequency response turned out to be the multiple tuning frequency. The nature of shallow water data introduces many multiples. For frequencies with wavelengths equal to or longer than the frequency corresponding to the multiple period, tuning occurs. Difficulties in visualizing and understanding the low frequency data may therefore be experienced. This is especially prominent when adaptation procedures are applied. Research presented in this thesis proves that the low frequency behaviour in the existing adaptation algorithms is improved when higher frequencies also are included. Due to better phase and amplitude consistency, the high frequencies guide the low frequency adaptation towards a better result.

The migrated and stacked results show that the main structures can be seen even for the lowest high-cut dataset used in the processing. The low frequency component of the full bandwidth data turned out to be superior to this dataset, which is an indication of CGG already operating with an acceptable low frequency processing flow. It is, however, still believed that the modifications suggested throughout this thesis will provide a total better processing of the low frequencies.

Sammendrag

Den nylige utviklingen i seismisk innsamlings- og prosesseringsteknologi har introdusert data med flere frekvenser enn tidligere. Seismisk bredbåndsdata har ført til utfordringer i hvordan å prosessere optimalt, ettersom flesteparten av de tilgjengelige algoritmene og teknikkene er konstruert for konvensjonell seismisk båndbredde. Denne oppgaven angriper den lavfrekvente responsen fra hvert av de utforskede prosesseringsstegene. Noen av stegene var forventet å prestere godt, mens andre trengte mer utfyllende testing.

Forsøkene ble utført ved å prosessere to datasett med ulike høykuttfrekvenser. Det første datasettet ble lavpassfiltrert med en høykuttfrekvens på 10 Hz, mens det andre datasettet ble laget med en høykuttfrekvens på 20 Hz. Et datasett med full båndbredde ble brukt som referanse og til sammenlikninger. Denne seismikken ble kommersielt prosessert av CGG i 2012-2013 med det som kan betraktes å være en moderne bredbåndsprosesseringssekvens.

I støyfjerningen ble det funnet at vinduet som fjerner støyen kunne økes. Denne observasjonen er viktig siden signal-støy forholdet til de lave frekvensene ofte er lavere enn for de høye frekvensene. I tillegg vil trolig mindre støy medføre en renere gjennomkjøring av andre prosesseringsmoduler. Den største utfordringen relatert til den lavfrekvente responsen viste seg riktignok å være interferens mellom havbunnsmultiplene. I grunt vann vil slike multipler opptre veldig ofte og regelmessig. For frekvenser med bølgelengde lik eller lenger enn den frekvensen som tilhører multippelperioden, vil slik interferens forekomme. Visualisering og forståelse av den lavfrekvente responsen vil da være vanskelig. Spesielt utfordrende var det å få adaptive metoder til å fungere godt. Resultater oppnådd i denne avhandlingen beviser at de lave frekvensene i adapsjonsprosessen drar nytte av at høyere frekvenser også er inkludert i gjennomkjøringen. På grunn av mer konsekvent fase og amplitude vil de høye frekvensene guide de lavere frekvensene til et bedre resultat.

Det migrerte og stackede resultatet viser at hovedstrukturene kan bli sett i det laveste høykuttdatasettet som ble brukt i prosesseringen. Den lavfrekvente komponenten til det prosesesserte datsettet med full båndbredde ble sammenlignet med dette og funnet bedre. Dette er en indikasjon på en allerede akseptabel lavfrekvent prosesseringssekvens som benyttes av CGG. Det er likevel antatt at modifikasjonenene som er foreslått i avhandlingen vil gi en totalt enda bedre håndtering av de lave frekvensene.

Contents

List of Figures

List of Tables

Chapter 1

Introduction

In 1921, near the Vines Branch in Oklahoma, a historical important experiment was performed. Haseman, Karcher, Perrine and Ohern proved that reflected seismic waves could be used to image the subsurface. They used a small dynamite charge that was ignited in a shallow hole to produce seismic waves. An instrument called a seismograph recorded the waves 300 meters away, and by analyzing this data the researchers identified a dipping reflecting boundary in the very first seismic reflection profile (Dragoset, 2005).

Imaging of the subsurface by using seismic waves is possible because rock properties like density and velocity depends on lithology. When a seismic wave propagates over a layer boundary, a change in impedance may occur. A part of the total wave energy is then reflected and can be recorded at the surface, while another part continues further down and can be reflected from deeper boundaries. There are many ways to acquire and process seismic data, but they all involve different sources and receivers and various ways of manipulating the recorded data. Reflection seismology is today widely recognized as the most powerful tool there is to visualize the subsurface in a large scale. This is of great value to the oil and gas industry that needs subsurface maps to locate hydrocarbons and to decide where to drill. Just like many of the innovations developed today, the Vines Branch experiment was motivated by the importance of improved exploration methods. Thanks to the petroleum industry, many great inventions eventually led to the detailed imaging the seismic companies are capable of delivering today.

Hydrocarbon exploration becomes more challenging as the sedimentary basins mature in terms of complexity of the available resources. Several companies often explore in the same areas and good data quality may be the difference between failure and success. An example of a relatively mature basin is the North Sea. In 1965, the Gerhardsen government awarded the first production licenses to oil companies exploring on the Norwegian continental shelf. ExxonMobil was awarded the very first of the licenses, PL001, but failed to make big discoveries. Several companies have been involved in PL001 since then. Among them are Saga, Elf, Norsk Hydro, Statoil and Enterprise. However, none were able to make any successful discoveries and the license was frequently

returned to the government (Norwegian Petroleum Directorate, 2012). In 2010, Lundin Petroleum made the Avaldsnes discovery in that very first license (renamed PL501). The field is now known as the Johan Sverdrup field and might be the third biggest discovery ever made on the Norwegian continental shelf (Lundin Petroleum, 2012). There are many aspects to consider in petroleum exploration and building a correct geological model from limited information can be difficult. The lack of high resolution seismic data may have been one of the main reasons why it took 45 years to discover this giant. The history of the Johan Sverdrup field should be a motivation for continued research and further development of the seismic technology.

The recent years progress in the seismic industry is of revolutionary measures. Broadband seismic has been introduced with the possibility of broadening the frequency spectrum obtained in both ends. High frequency waves are damped faster than low frequency waves. Hence, low frequencies are more important for imaging of deep layers. Among others, Kallweit and Wood (1982) argues that the limit of vertical resolution corresponds to one-fourth of the wavelength, widely accepted as Rayleigh's criterion. As the wavelength is reversed proportional to the frequency, high frequencies are important for a sharp picture. Broadband seismic therefore means clearer seismic with the possibility of identifying deeper structures. Attention has also been directed towards seismic inversion. This process of extracting rock properties such as density and velocity from the data, can make use of the lower frequencies often missing in conventional seismic. In this way, the dependence on well data decreases and inversion can be performed accurately in more areas. Since PGS presented their GeoStreamer™ solution in 2007 (Carlson et al., 2007), several acquisition and processing methods have been developed for the purpose of producing broadband seismic. CGG acquire such data with their BroadSeis™ solution that was presented in 2010 (Soubaras and Dowle, 2010), while WesternGeco commercialized their IsoMetrix™ system in 2012 (Robertsson et al., 2008). Before this, conventional seismic processing had settled with algorithms and modules handling a common frequency spectrum with conventional geometry. As the spectrum now are pushed towards both ends, an interest in understanding how the well established processing modules handle the lowest and highest parts of the spectrum has developed.

In this thesis, focus will be on the low frequencies and how they respond to common processing routines. All major stages of the seismic processing flow will be examined. Challenges will be highlighted and possible improvements will be discussed. BroadSeis data over Statoil's Sleipner field (ST12018) has been made available for the study. The area is geological non-challenging with mostly flat layers. In addition, full bandwidth processed data exist from recent work in CGG, making good direct comparison by filtering easy. The basics of seismic acquisition and processing will be presented in chapter 2. An introduction to broadband seismic follows in chapter 3, while the theoretical background ends with a review of low frequency generation and recording in chapter 4. The results and findings from the low frequency processing will be given in chapter 5 and evaluated in chapter 6 through a discussion. In chapter 7, the concluding remarks are stated while a recommendation in how to proceed the research is given in chapter 8.

Chapter 2

Seismic acquisition and processing

2.1 Marine seismic acquisition

In conventional marine seismic acquisition, seismic vessels are used to gather data. The typical approach is to tow streamers equipped with receivers behind the ship, which can register the wavefield transmitted by the seismic sources. When a seismic wave experience an acoustic impedance (*velocity* $\times$ *density*) change in the medium where it propagates, some of the energy is reflected and the signal can be registered by the receivers as shown in **Fig. 2.1.** This makes it possible to image changes in the physical parameters in the subsurface. To obtain good reflection data, several aspects of seismic acquisition needs to be considered. The most prominent ones will be explained in this section.

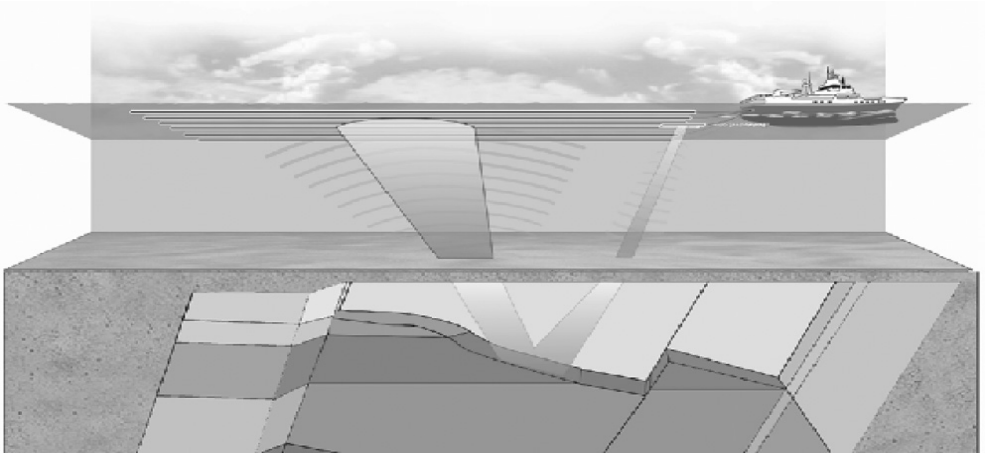

Figure 2.1 – *In a conventional marine seismic experiment, a vessel tows streamers that register waves produced by the source and that are reflected from the subsurface. This data can be used to reconstruct an image of the subsurface geology. Source: Elboth et al. (2012).*

2.1.1 Source characteristics

A seismic source can be defined as a device that release energy into the earth in the form of seismic waves. During the life of seismic exploration, several types of sources have been used in experiments. In land acquisition, dynamite and seismic vibrators are among the more famous alternatives. The preferred choice depends on the situation and is a function of target, geology and budget together with safety and environmental concerns. Water guns have been proposed in the marine setting, but the sovereign winner here is the air gun. The air gun possesses some important qualities that the industry demands. It is controllable, repeatable and predictable and has minor impact on marine life (Landrø and Amundsen, 2010-2011). As the data used in this thesis is acquired with air guns, the discussion of seismic sources will be limited to the understanding of this mechanism and its output.

The air gun releases compressed air, typically around 138 bars, into the water. This generates an expanding bubble with corresponding acoustic pressure development. The strength of this primary signal can be denoted peak-to-peak (P) and is illustrated in **Fig. 2.2.** The expansion of the bubble originates from the pressure difference between the inside of the bubble and the hydrostatic pressure. As long as the pressure inside the bubble is higher, the bubble will expand. When the bubble is at maximum size, the pressure inside will be lower than the hydrostatic pressure and the bubble will start to collapse. In this way, the bubble oscillates between an inside pressure of higher and lower than the hydrostatic pressure, limited by frictional forces or breaking of the bubble as it reaches the sea surface. The physical effect of the secondary bubble pulse is that it emits a non-ideal signal following the primary. A term called primary-to-bubble ratio (P/B) is used to describe this effect, where a high P/B is wanted.

To increase the P and the P/B, source arrays are established. The total strength of an air gun array is linearly proportional to the number of guns in the array, close to linearly proportional to the firing pressure and roughly proportional to the cube root of its volume (Landrø and Amundsen, 2010a). Several guns in some kind of arrangement are therefore desirable, typically 18-48 guns firing every 10-15 seconds. Some of the air guns can also be put very close together making them interact in a way that improves the P/B. This technique is called clustering and is frequently used today. Another important term for bubble characterization is the bubble time period given by the well known modified Rayleigh-Willis formula:

$$T = k\frac{P^{\frac{1}{3}}V^{\frac{1}{3}}}{(P_{\text{atm}} + \rho g D)^{\frac{5}{6}}} \tag{2.1}$$

Here, k is a constant depending on air gun details, P is the firing pressure, V is the gun volume while the denominator represent the hydrostatic pressure. Bigger bubbles needs more time for each oscillation cycle than small bubbles with same pressure. This can be seen in the equation where increasing the gun volume increases the time period.

By placing individual guns with different volumes together on a string and put several strings next to each other, the constructive summation of the primary peaks will lead to an increase in P, while the destructive interference of the different bubble peaks will lead to an increase in P/B. In addition, the bubble time period dictates the dominant frequency of the bubble motion according to $F = 1/T$. This must also be considered when constructing the source array. For instance, by increasing the gun depth D, the hydrostatic pressure increases and the bubble time period decreases. This affects the output frequency spectrum. Another challenge related to array configuration is to distribute the output energy in a way such that most of the energy is focused downwards. How the energy radiation behaves is commonly referred to as the directivity of the source array.

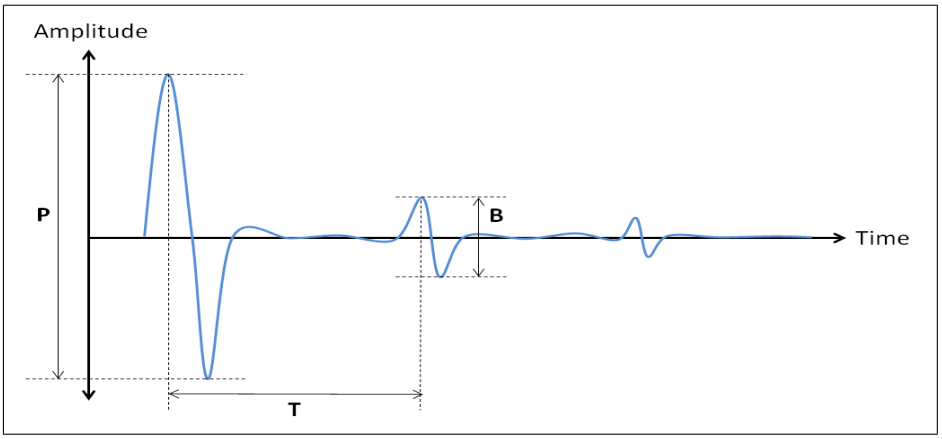

Figure 2.2 – *An exaggerated far field source signature. P is a measure of the primary signal strength. P/B is a measure of the strength of the primary signal compared to the following bubble pulse. T is the bubble time period.*

2.1.2 Receiver characteristics

The towed cables contain receivers that are sensitive to either pressure variations or particle motion. In conventional marine acquisition, the hydrophone is the common apparatus used for pressure recordings. A small cylinder with piezoelectric material in both ends will make contact when they experience a pressure wave. This mechanical deformation produces an electric signal proportional to the amplitude of the seismic wave (Landrø, 2008). The hydrophone measures a scalar field and will therefore gather data independent of measurement direction. In modern cables, the hydrophones are usually evenly arranged in small groups of 3-4 over the cable length, typically separated by a distance of 1.8 meters. For approximately every 12.5 meters, the different hydrophone elements are summed such that noise deviations are cancelled. These 12.5 meter recordings are often referred to as channels in the language of seismic processing. It must be emphasized that these numbers might differ from contractor to contractor.

The geophone is capable of converting the particle velocity into an electric signal. The apparatus usually consist of a magnet and an inductor. When a relative motion between the two is produced by the seismic wave, voltage is induced in the inductor. This electric signal can be recorded digitally (Landrø, 2008). In contrast to the pressure, the particle velocity is a vector component. The signal direction of interest is the vertical and the geophones have to be designed and equipped on the streamer for the purpose of such measurements. Currents or other flow patterns associated with water motion close to the streamer will contaminate the signal. High quality marine geophone recordings of the vertical particle velocity field have therefore been difficult to achieve.

2.1.3 The ghost effect

The wave emitted by an air gun is approximately spherical and will have components going both up and down. It is widely accepted that the water-air surface can be regarded as a free surface with a reflection coefficient of -1 because of the great difference in acoustic properties. With this, one also assumes flat sea surface. The upgoing part of the signal is reflected at the free surface producing a wave propagating in the same direction as the downgoing part, delayed by the time corresponding to the additional travel path. This phenomenon is referred to as the source ghost. The reflection can be thought of as originating from a source mirrored against the sea surface. With a water velocity of c, **Fig. 2.3** shows that the additional travel time compared to the primary pulse will be $\tau = 2z_g \cos\phi/c$. Exactly the same happens at the receiver side, but here the additional traveltime will be $\tau = 2z_g/c \cos\phi$ as can be observed in the same figure. This wave goes by the name receiver ghost.

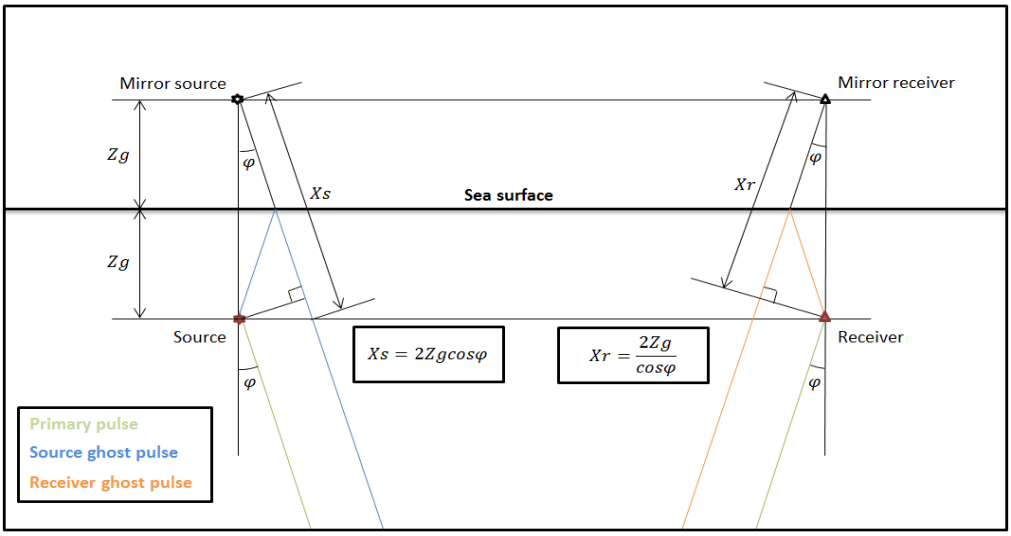

Figure 2.3 – *The ghost effect occurs at both the source and receiver side due to the perfect reflection from the free surface. Their additional travel distance compared to the primary pulse can be seen on the figure.*

The ghost effect has been addressed in seismic exploration for a long time and it's a well known problem. From the above explanation, it is clear that the primary pulse, source ghost pulse and receiver ghost pulse will interfere. To examine how they interact, the zero incidence situation ($\phi = 0$) can be considered for illustration. The additional traveltimes then reduces to $\tau = 2z_g/c$ for both ghosts. The far field response vertically at a distance R below a source deployed at a depth z_g, can be expressed as in Landrø (2011):

$$s(t) = \frac{1}{R}p(t - \frac{R}{c}) - \frac{1}{R_g}p(t - \frac{R_g}{c}), \tag{2.2}$$

where $p(t)$ denotes the notional air gun signal, c is the water velocity while R_g represents the travelling distance for the ghost ($R_g = R + 2z_g$). A sea surface reflection coefficient of -1 is also used. Fourier transform of the source term and ghost term, respectively, yields

$$\frac{1}{R}p(t - \frac{R}{c}) \xrightarrow{\mathscr{F}} \frac{1}{R}P(\omega)e^{\frac{-i\omega R}{c}}$$

and

$$\frac{1}{R_g}p(t - \frac{Rg}{c}) \xrightarrow{\mathscr{F}} \frac{1}{R}P(\omega)e^{\frac{-i\omega(R+2z_g)}{c}},$$

when $R_g \approx R$ in the ghost term denominator. For this to be valid, one assumes $R \gg z_g$. The source term is common in both parts, so Eq. 2.2 can be written as:

$$S(\omega) = \frac{P(\omega)}{R}e^{\frac{-i\omega R}{c}}[1 - e^{\frac{-i\omega 2z_g}{c}}] \tag{2.3}$$

The impact of the ghost in the frequency domain can then be extracted and expressed as a ghost function:

$$G(\omega) = 1 - e^{\frac{-i\omega 2z_g}{c}}. \tag{2.4}$$

From the ghost function, the power spectrum can easily be found:

$$|G(f)| = |2\sin\frac{2\pi f z_g}{c}|. \tag{2.5}$$

From Eq. 2.5, the physical effect from the ghost is revealed. As $|sin(x)|\epsilon[0, 1]$, the function varies between 0 and 2, meaning that it will double the amplitudes at the maximum value and zeroing out the amplitudes at minimum value. Further, maximum

and minimum values are found to be corresponding to specific frequencies. Setting the argument of the sine function to zero gives the so called notch frequencies, while putting the argument equal to $\pi/2$ reveals the frequencies that strengthens the amplitudes:

$$f_{max} = \frac{c}{2z_g}(n - \frac{1}{2}), \qquad n = 1, 2, 3, ... \tag{2.6}$$

$$f_{min} = \frac{c}{2z_g}n, \qquad n = 0, 1, 2, 3, ... \tag{2.7}$$

The effect of the ghost (one ghost at zero incidence) is demonstrated in **Fig. 2.4**, showing that the minimum frequency values act as notches in the frequency spectrum. In addition to lost signal at the notches, the frequencies close to them are also severely attenuated. This is one of the reasons why low frequencies are hard to obtain, since the first notch always will be at 0 Hz. As the above equation proves, these notch frequencies depend on source and receiver depth. It is also worth to notice that if the source is deployed at a different depth than the towing depth, the source and receiver notches occurs at different frequencies meaning that more notches are introduced in the data. On the other hand, by using approximately the same source and receiver depth, the constructive summation of the wavefield means that the signal is enhanced four times at the maximum frequencies. What frequency spectrum that is desirable for the specific survey location can in this manner be decided by the source and streamer depths. Much of the recent technology advancement in the seismic industry relates to the ghost effect and how to obtain information at the notch frequencies. This will be discussed more in the chapter about broadband seismic.

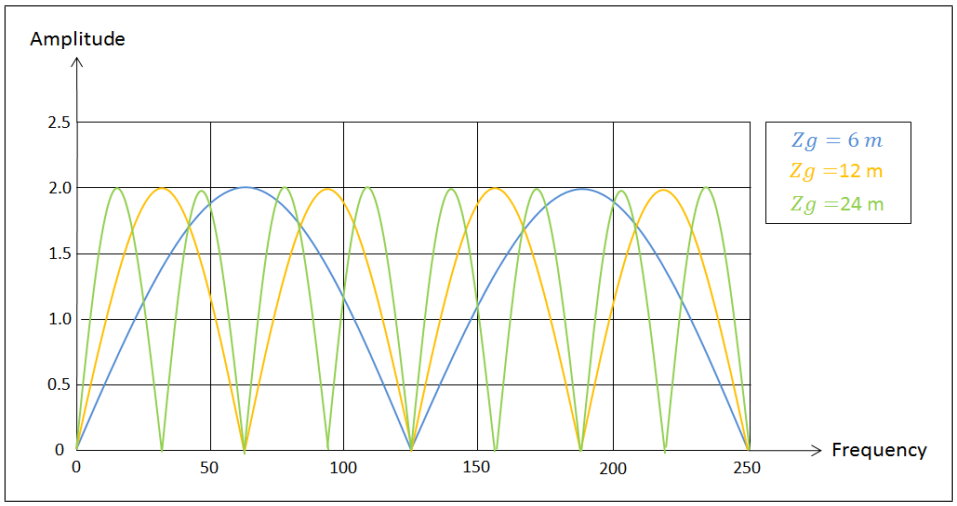

Figure 2.4 – *Pressure ghost response for different streamer depths at zero incidence angle. A source or receiver at 6 meters depth will have a notch at 125 Hz. A depth of 12 meters gives less attenuation around the 125 Hz notch, but introduces another notch at 62,5 Hz. Note that this is a maximum frequency for the source towed at 6 meters.*

2.2 Marine seismic processing

To be able to read the geology from the gathered seismic data, several processing steps need to be performed. The arrangement of these steps, the flow, is tailored to fit the requirements set by factors such as geology of area, target location, time and economics. Many methods have been proposed to most of the challenges. There are, for instance, several demultiple and migration methods that can be applied to the dataset. The most important processes and common obstacles will be described in this section. The main idea is to get an overview of the concepts, not an in-depth understanding of algorithms and processes. The specific techniques used in the low frequency processing part of the thesis will be discussed further in chapter five.

2.2.1 Attenuation of seismic waves

The wavelet from the seismic source has experienced multiple amplitude reducing effects before it reaches the receiver. To successfully recover the true amplitudes, an understanding of the involved mechanisms is necessary. A simplified description of the registered amplitude can be:

$$u(\vec{x},\omega) = f(\omega)e^{i\omega t(\vec{x})}g(\vec{x})\sum t_i(\vec{x})a(\vec{x},\omega). \tag{2.8}$$

Here is $f(\omega)$ referring to the signal pulse and $\tau(\vec{x})$ is the traveltime. The three last terms in Eq. 2.8 represents the geometrical spreading, $g(\vec{x})$, the transmission losses, $\sum t_i$, and anelastic absorption, $a(\vec{x},\omega)$. These terms are well known in the literature and will be discussed further. The x, y and z represent common directions and ω is the angular frequency.

From the acoustic wave equation it can be shown that the amplitude of a spherical wave is inverse proportional to the distance travelled (Sheriff and Geldart, 1995). The energy is distributed according to the surface area of a sphere, hence energy is inverse proportional to distance squared. Since energy and amplitude are related through $E = kA^2$, energy can be considered conserved. With the total wavefield energy kept constant, the strength of the wave has to be reduced when it occupies a bigger area. This $1/r$ factor is called the spherical divergence factor or geometrical spreading. It assumes homogeneous material and a perfect spherical wave. In reality, however, the earth is layered and far from homogeneous. Other methods have therefore been developed in addition, as for instance a technique taking layering and root mean squared (RMS) velocities into account. In Ursin (1990), this method is presented.

The main point of reflection seismology is to image layer boundaries in the subsurface. When the wave encounters a change in impedance, some of the energy is reflected and can be registered at the surface while another part continues further down into the earth to image more layers. This is fortunate as we are interested in the reflections, but it

also means that for each boundary, less energy will continue further down in the earth. Some of the energy will also be converted to other types of waves when experiencing such contrast boundaries. These losses are known as transmission losses and can be estimated theoretically (Landrø, 2008).

The elastic energy associated with the wave motion will gradually be absorbed by the medium. The energy transfer is mostly referred to as heat, but effects as squirt flow and inhomogeneities have also been accepted as possible mechanisms for absorption. A measure of relative energy loss due to anelastic absorption per cycle of wave propagation is the quality factor (Q). Q can be assumed to be frequency independent in the seismic bandwidth. With constant energy loss per cycle, absorption will be larger for the short wavelength high frequencies than for the long wavelength low frequencies. The relation between amplitude and absorption can be expressed as

$$A = A_0 e^{\frac{-\pi f t}{Q}}, \tag{2.9}$$

where A and A_0 represents the amplitude at time t and at $t = 0$, respectively, while f is the frequency. Q-values representing common lithologies are presented in **Table. 2.1**.

One way of compensating for these attenuating effects is to apply an enhancing function to the signal that gradually increases equally to the gradually amplitude decrease. Both geometrical spreading and absorption are proportional with time. Therefore, a scaling of t^n have been the conventional solution to the damping problem where n is some number chosen to fit the specific data. In this way, one does not need to distinguish between the levels of influence from the two effects. This simple technique can be justified by the interpreters desire of having approximately constant amplitudes with depth. An additional gain is therefore often applied just to ensure a smooth seismic section.

Material	**Q**
Sedimentary rocks	20-200
Sandstone	70-130
Shale	20-70
Limestone	50-200
Chalk	135
Dolomite	190
Rocks with gas in pore space	5-50
Metamorphic rocks	200-400
Igneous rocks	75-300

Table 2.1 – *Different Q-values. Source: Sheriff and Geldart (1995).*

2.2.2 Deconvolution

The wavelet emitted from the source and the wavelet registered by the receiver are not equal. When travelling through the earth, the wavelet is altered by the sum of what it encounters on its journey. How the wavelet is altered is interesting as it represent the geology. A seismic trace, $y(t)$, can be expressed as a convolution between the source, $s(t)$ and the reflection coefficient time series, $r(t)$:

$$y(t) = s(t) * r(t). \tag{2.10}$$

The validity of Eq. 2.10 is limited to the assumption of the earth behaving as a linear filter and that the wave propagation can be modelled by filtering of the source signal. The primary goal is to recover $r(t)$, as both $y(t)$ and $s(t)$ are assumed known. Fourier transform of Eq. 2.10 helps for the calculation:

$$Y(f) = S(f)R(f). \tag{2.11}$$

$R(f)$ can then be expressed by Y(f) and S(f) as

$$R(f) = \frac{Y(f)}{S(f)} = S^{-1}(f)Y(f). \tag{2.12}$$

By applying the inverse filter of the source to the dataset it is possible to recover the reflectivity. This process is known as deconvolution. In reality, deconvolution is not as simple because of noise in the data. Modification of the filter might therefore be needed. The deconvolution method can be applied with other type of filters as well. Spiking deconvolution is a deconvolution method that can be executed to increase the ability to separate closely spaced reflectors, while other types of filters can be constructed to, for instance, attenuate multiples.

2.2.3 The stacked seismic trace

Consider a receiver detecting the reflections from the boundaries in the subsurface. The amplitude fluctuations corresponding to these boundaries will occur with some time delay depending on the distance and the velocity field between the surface and the reflections. The recorded amplitude fluctuations with respect to time belonging to this receiver are called traces. The neighboring receiver trace (further away from the source), will usually look quite similar, but as the distance now have changed (and possibly the velocity field), the reflections will occur by a small time delay in the trace. In addition, they might represent different reflection points depending of the ray paths. In seismic processing, it is therefore important to sort the data properly. Several ways of sorting exist. Collection of traces that corresponds to a common source can be placed next to each other so that

the offset (distance between source and receiver) increases. This common sorting is usually called a shot gather or common source gather. The receiver point can also be held fixed such that the traces represent different shots. This technique is often referred to as common receiver gather. Common offset gather is another sorting method where traces from only one defined offset are displayed. However, these techniques display different reflection points. It is desirable to gather all the information from one reflection point. This way of sorting is done in a common midpoint (CMP) gather. The simplest approach for constructing a CMP-gather is to assume flat layers with a velocity profile laterally constant. The CMP will then be located in the middle between the shot point and receiver. In a CMP-gather, the traces are therefore sorted in source and receiver pairs. Using this model, with an offset of x, a velocity of v and a zero offset traveltime of t_0, the traveltime squared can be expressed as:

$$t^2 = \frac{x^2}{v^2} + t_0^2. \tag{2.13}$$

By assuming that twice of the vertical depth is considerable larger than the offset and performing a taylor expansion, one arrives at:

$$t = t_0[1 + \frac{1}{2}(\frac{x}{vt_0})^2 - \frac{1}{8}(\frac{x}{vt_0})^4 + ...]. \tag{2.14}$$

The lowest order is known as the normal moveout (NMO):

$$\Delta t_{NMO} = \frac{1}{2}\frac{x^2}{v^2 t_0}. \tag{2.15}$$

By correcting for the additional travel time as a consequence of offset, the seismic events in a CMP-gather will in theory occur on a straight line. To use Eq. 2.15, velocities are needed. A mathematical function called semblance produces plots that enable the interpreter to pick correct velocities. The basic idea with these plots is that the traces in the CMP gathers are explored with different velocities. A summation of the amplitudes belonging to a corresponding velocity is performed. When the velocity is correct, all the amplitudes representing one reflector is summed, giving an area on the contour plot with a darker color than the surroundings (assuming dark colors represents high values). For successful application of the NMO-correction, an accurate velocity model is critical. When the data has been corrected and occurs on a straight line, a procedure called stacking can be done. The principle of stacking is quite simple. An average of the traces is estimated through a sum-divide process such as the uncertainty related to one trace is considerably reduced. This averaged trace will now represent that specific reflection point. By doing this for all reflection points and putting them together, the primary image of the subsurface can be obtained. **Fig. 2.5** illustrates the process. If the amplitudes versus offset (AVO) response varies greatly or even change polarity, the stacking can be divided into near, middle and far offset stacks.

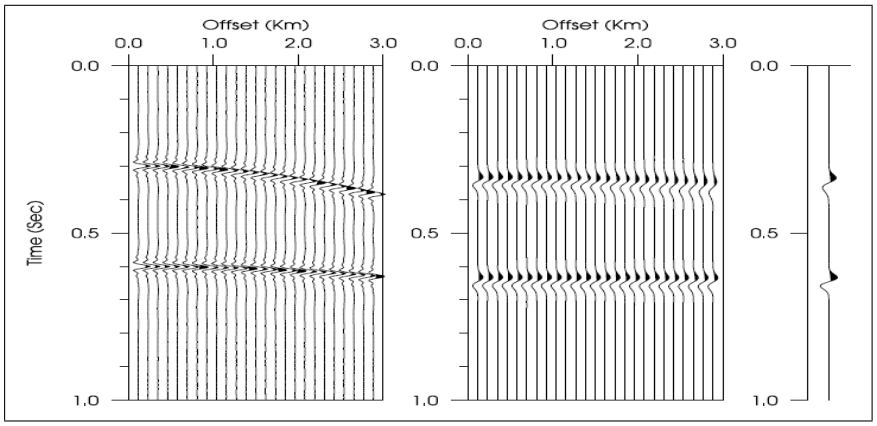

Figure 2.5 – *The left side shows a CMP gather with a moveout corrsponding to the layer interval velocity. After NMO correction, the events align ideally on a straight line, illustrated in the middle gather. This can be stacked to achieve an average trace, displayed on the right side. Source: Arntsen (2011).*

2.2.4 Noise

Recorded seismic data will always contain a component of noise. As a general definition is any recorded energy which interferes with the desired signal considered as noise (Elboth et al., 2008). If the cables were to record without the source firing, the data would consist of the wind and swell sounds together with possible production or interference from other vessels. This can be denoted as the background noise. Instrumentation noise from the mechanical devices and the electronics in the system might also show up as coherent or incoherent energy. When adding the source into the equation, a third type of noise will be detected. Source-generated noise is for instance identified as direct waves, scattered waves and multiples. The overall noise picture is therefore complex and makes denoising, the process of increasing the signal-to-noise ratio (S/N), a challenging task for the geophysicist. All sources of sound in the seismic range can in principle be considered as having influence on the data. For instance will biological activity contribute to the background noise level. However, all noise types cannot be addressed here and the section is limited to the following classification of noise sources, inspired by Elboth and Hermansen (2009), Elboth et al. (2009) and Landrø and Amundsen (2013c):

- Ocean waves
- Turbulent flow and vortexes
- Tugging, birds and strumming
- Cavitation
- Seismic interference
- Multiples

Two direct effects from ocean swells are affecting the streamer. The circular behavior of the particle movement in water due to surface waves will lead to flows across the streamer. These flows increases with the swell size. The vertical movement of a particle, $w(x, z, t)$, was given by Kundu (1977):

$$w(x, y, t) = A\omega e^{-ikz} \sin(kx - \omega t) \tag{2.16}$$

A is the amplitude of the surface waves with positive depth, z, downwards, ω is the angular frequency, k is the wave number ($= \frac{2\pi}{\lambda}$) and g is gravity. Another direct consequence of the swells is the variation in water column height above the receiver system. This leads to a pressure change according to

$$\Delta p = \rho g \Delta h, \tag{2.17}$$

where ρ is density and Δh is the difference in water column height above the streamer. When sitting on the beach, one can often count eight seconds between each wave. This is because these waves have a very long wavelength, typically around $50 - 100$ meters. Ocean wave generated noise therefore arrives as very low frequent signals.

Close to the streamer, the flow can be considered as turbulent. This turbulent layer will further change flow characteristics when the local angle between the streamer and the flow direction exceeds 6-15° Elboth et al. (2010). Ocean currents and vertical movement from Eq. 2.16 make up a total crossflow component over the streamer that is beyond this limit and complicates the situation further. This can induce an unsymmetrical turbulent boundary layer where vortex shedding might occur. This is an unsteady flow and the presence of vortices will be seen in the seismic gather as high amplitude noise. The vertical motion of the streamer can also provoke transversal waves, known as bulge waves, that generate high amplitude noise. The combination of bulge waves and vortex-shedding noise is what is commonly, somewhat misguiding, referred to as swell noise and consists of signal in the frequency range of approximately 1-10 Hz.

It is reasonable to assume some sudden movement in the towing speed during the acquisition due to wave motion. This introduces tugging of the streamer which often can be seen as 3-10 Hz noise components in the seismic gathers. The tug noise increases when the angle between the head and tail buoy increases. This means that tug noise often increases when towing deeper. The first sections of the streamer can also contain some noise related to cable vibrations, also called strumming. They often occur as linear noise in the same frequency band as the tug noise. The devices that control the streamer depth, the birds, are attached to the streamer with a defined interval. Around these bird zones, some extra noise will be introduced, likely because of flow pattern alterations.

When fluid is accelerated, from for instance a propeller, small low pressure zones are formed. If the pressure fall as low as into the vapor pressure zone, small amounts of water will transform to bubbles and suddenly collapse as the pressure stabilizes. These

collapses induce shock waves that can be detected by the receivers. Cavitation noise is normally broadbanded and periodic (Elboth and Hermansen, 2009). Other sources of cavitation might be due to rapid movement of air gun components and perhaps also noise produced by the pistol shrimp (Landrø and Amundsen, 2010b).

The great competition among oil companies and the seismic contractors means that there often is significant activity in the area of exploration. Platforms or other vessels might generate sounds that the sensitive receivers will register. Such seismic interference can occur in several forms, but is often large in amplitude and can typically be seen as diagonally broadbanded stripes on a shot record.

Multiples are a special type of source-generated noise. They are events that have undergone more than one reflection. The amplitudes to the multiples are proportional to the reflectivity coefficients involved and since these are small for most interfaces, only the boundaries with the largest impedance contrast produces recognizable events. The contrast from water to solid ground on the sea floor is very high. Hence, the reflection coefficient is large and the water layer is therefore an example of a layer where multiples may arise. Sheriff and Geldart (1995) distinguish between long path multiples and short path multiples, where the long path multiples have so much longer travel time than the primary that they appear as separate events on the seismic record. The short path multiples arrive soon after the primary, leading to a tail addition and a waveshape alteration. Different multiple types are shown in **Fig. 2.6**.

Methods to reduce seismic noise are discussed in for instance Elboth and Hermansen (2009). Besides improving the equipment technology, there are in principle three ways this can be done. By reducing the towing velocity some of the flow related noise will be less significant. However, reduced towing speed is costly as the total acquisition time increases. Seen from Eq. 2.16, the weather generated vertical velocity flow decreases exponentially with depth. The relative influence of the hydrostatic pressure difference due to wave heights and lows also diminish with depth. By towing the streamers deeper, the S/N will therefore improve. There are, however, other complications related to deep towing, such as tugging and the ghost notches. The third option for denoising of the data is to apply signal processing. Denoising is well established as a major part of the data processing and many methods exist. The main idea and principle for almost all techniques is that they transfer the data to a domain where the signal and the noise component can be separated. The noise is then removed and the data transferred back to the desirable domain. Common methods are described in Elboth et al. (2008). Prediction filtering, Radon-based transforms in combination with muting, wavelet transforms and time-frequency filtering (TFDN) are such examples. A special part of denoising is set to handle the multiples. Demultiple is considered as a separate data processing step. Besides stacking (multiples arrive with slower apparent velocity and will not align perfectly after NMO-correction), several demultiple methods have been developed. A common approach is to make a model of the multiples and then perform a subtraction algorithm to remove them from the data.

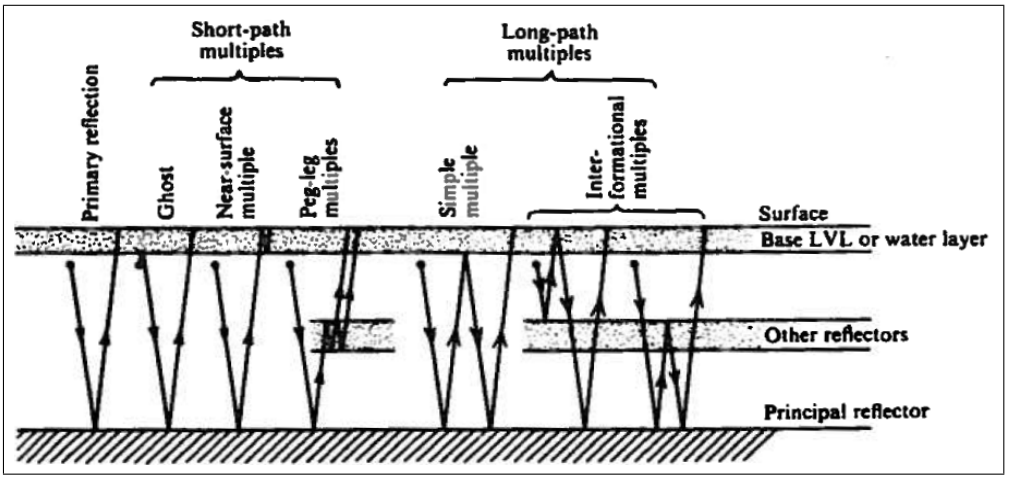

Figure 2.6 – *Different types of multiples. Both short-path and long-path types will occur in a seismic experiment. Source: Sheriff and Geldart (1995).*

2.2.5 Migration

After CMP sorting and stacking, the traces can be plotted next to each other. This will give a first impression of where the layer boundaries are located in the subsurface. By assuming that all layers are flat, this image will be fairly correct. In reality, the subsurface often contain complex geologic structures with dipping lithology. If such dipping layers are present, the assumption of the reflection points directly under the common mid point does not hold up. **Fig. 2.7** explains how dipping layers are erroneous imaged.

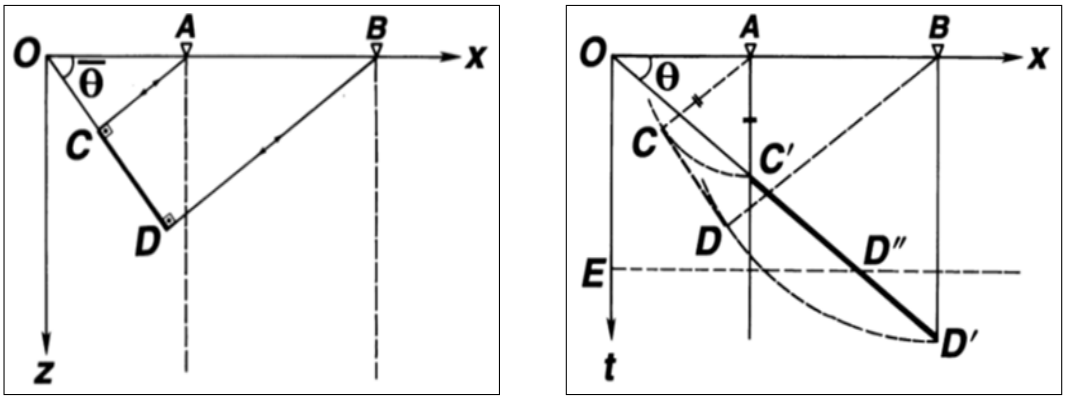

(a) *True position of the segment CD* **(b)** *CD will be observed as C'D'*

Figure 2.7 – *The migration principle. (a) gives the true location of the reflecting surface CD observed at receiver A and B. (b) A reflection from point C will be observed in receiver A as C' while a reflection from D observed in receiver B will be plotted as point D'. Note that AC=AC' and BD=BD'. It is clear that CMP sorting and stacking produces a reflector, C'D', that differs from the true reflector, CD. Source: Yilmaz (2001).*

From Fig. 2.7, it can be seen that the reflector is imaged with a smaller dip, obeying the migration equation:

$$\tan\theta = \sin\bar{\theta}. \tag{2.18}$$

Considering the classical example from Claerbout (1985), where a plane ocean wave is approaching the beach. If there is a storm barrier with a small gap some distance from the shore, the wavefront evolving after passing the barrier will be approximately spherical. The gap is acting as a secondary source according to Huygens' principle where every point on a wavefront can be regarded as a new source of waves (Sheriff and Geldart, 1995). If a receiver was installed on the beach, the recorded wave would have a hyperbolic traveltime trajectory (Yilmaz, 2001). In the seismic data, the reflectors can be thought of as consisting of a continuous series of sources and the superposition of these creates the reflector shape. However, if abrupt changes occur, the end parts of the reflector will not have components that destructively remove the diffraction tales. In general will sharp irregularities be a source of diffractions in the data. Such examples are faults, magmatic intrusions and other local lithology changes. Synclines will also provoke recognizable features in the seismic data. These are often known as bow ties because of their characteristic look. Diffractions and bow ties can be seen in **Fig. 2.8.**

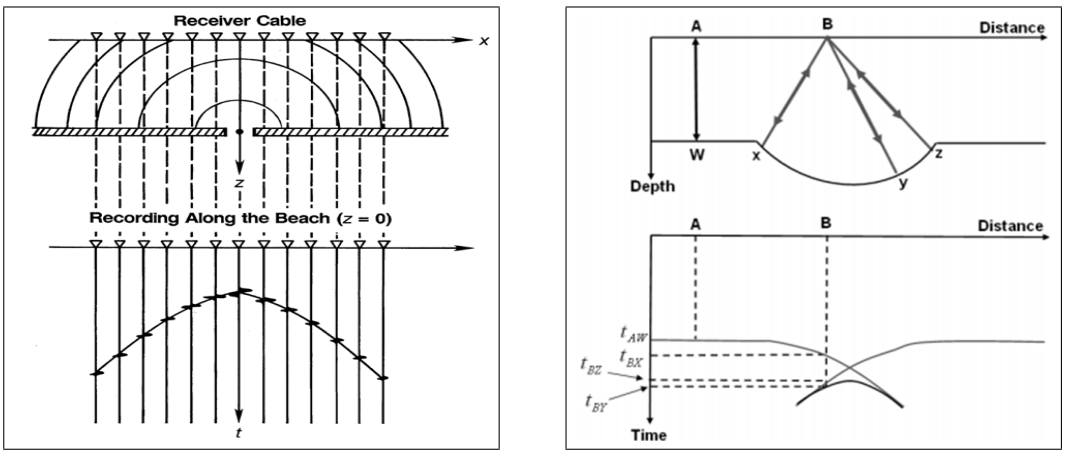

(a) *Diffractions* **(b)** *Bow ties*

Figure 2.8 – *Characteristic features that can be seen in the seismic. (a) Diffraction points can give a hyperbolic traveltime event in seismic gathers. (b) Bow ties occurs from synclines. Source: Left figure from Yilmaz (2001) and right figure from Landrø (2008).*

The purpose of seismic migration algorithms is to move dipping reflections to their true subsurface position, and collapse diffractions. Synclines will then be revealed from the bow ties and the diffractions will become focused to points. This increases the spatial resolution and yielding a seismic image of the subsurface (Yilmaz, 2001). The process is therefore often called imaging.

Several types of migration can be performed and the strategy of choosing the appropriate migration depends on the requirements set by the data, which again is decided by the geologic complexity. Economics does also affect what method that can be applied, as migration is a processing routine that often requires powerful computers to be executed. The main options for migration can be narrowed to time or depth migration handling the data either pre or post stack in 2D or 3D. Inside these classifications, many algorithms exist. To understand how many of these algorithms have developed, the exploding reflector model (ERM) can be considered, first explained by Loewenthal et al. (1976), after inspiration from Claerbout and Doherty (1972). **Fig. 2.9** illustrates the concept of the ERM. The model is based on the idea that imaginary sources can be placed along the reflector. By using half of the true velocity, the traveltime from the source to receiver can be considered as a one-way traveltime from the reflector to the receiver. The ERM assumes stacked data. Applications from this model are therefore often called zero offset migration methods.

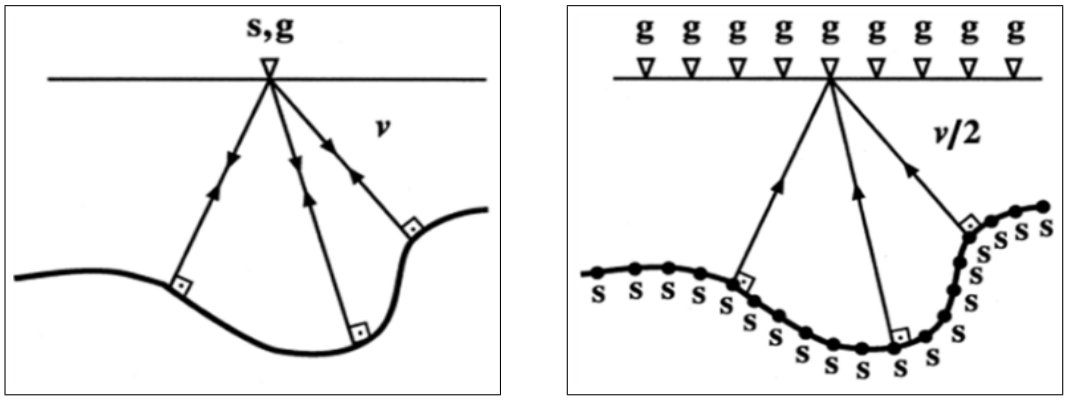

(a) *Normal two-way traveltime* **(b)** *ERM with one-way traveltime*

Figure 2.9 – *The exploding reflector model. (a) Set up for the true recordings with velocity of v and the sources and receivers located at the surface. (b) With the velocity set to v/2 and the imaginary sources placed along the reflecting surface, the wave travels only one way. Source: Yilmaz (2001).*

The migration equation, Eq. 2.18, assumes that the velocity is constant in all directions. It is therefore more illustrating than practical. For successful applications of seismic migration, a good velocity model is critical. In mature areas, information of the velocity model is often available and well known. In frontier exploration, the velocity model must be constructed mainly from picking on semblance plots (see section 2.15.) The reverse process of migration is called modelling and can be done, for instance, after migration to update the velocity profile. In this way, the accuracy of the data will improve if the method is applied again. The core of the migration algorithms is based on an understanding of how the wave propagates.

A description of a compressional wavefield $P(x, z, t)$ in a medium with constant density and compressional wave velocity $v(x, z)$ is given by the 2D scalar wave equation:

$$(\frac{\partial^2}{\partial x^2} + \frac{\partial^2}{\partial z^2} - \frac{1}{v^2}\frac{\partial^2}{\partial t^2})P(x, z, t) = 0 \tag{2.19}$$

Yilmaz (2001) evaluates migrational algorithms that are developed to solve Eq. 2.19. Three main categories are stated:

- Integral solutions
- Finite-difference solutions
- Frequency-wavenumber implementations

As many methods exist in all categories and cannot be addressed here, this section is restricted to an understanding of the ERM and the criterions for imaging using the respective model. With an appropriate wavefield extrapolator, f, the wavefield observed at a receiver, n, expressed by $P(x, z = 0, t)$ can be used to construct $P(x, z_n, t)$. The connection can be given as

$$P(x, z_n, t) = f(P(x, z = 0, t). \tag{2.20}$$

By now following the wavefield backwards in time, one arrives at the true reflector position at t=0, when the imaginary sources are firing. The imaging condition according to the ERM will therefore be:

$$I(x, z) = P(x, z_n, t = 0). \tag{2.21}$$

This operation can be done for all points in the data leading to the migrated image. The main principles of post-stack migration can further be translated to pre-stack migration. The main difference is that the operator needs to be constructed to compensate for the variation in offsets. What method to use has earlier been dictated by computer limitations and economics. The exceptional improvements in computer capacity the latest years make the preferred migration method today almost exclusively a 3D pre-stack method. Other 2D or post-stack methods are more common for testing and quality control than for production projects. The goal of migration is to make the stacked section appear similar to the geologic cross-section in depth along a seismic traverse. The option of choosing time or depth migration is mainly decided by the presence of lateral velocity variations where large variations call for depth migration. If time migration is used, a conversion to depth can be done later for a good geologic evaluation.

Chapter 3

Broadband seismic

3.1 Technology development

Dragoset (2005) summarizes the technology development in the seismic industry since the Vines Branch experiment. The 1929 rise in oil price created more interest and acceptance of seismic reflections as a method in hydrocarbon exploration. At this time, dynamite was used as the source, the receivers were large and heavy and land seismic was dominating. Alternatives to explosive charges were developed in the 1950s for land seismic when Conoco introduced the Vibroseis. At this time, modified land equipment was common in marine seismic. Cables with receivers were used and the boat had to stop for every shot. When the streamer was developed in the 1960s, marine seismic experiments became more common. Both sensors and wires were coupled together in this hollow cable and a direct connection to the data recording system on board the boat was now possible. Stephen Chelminski, founder of Bolt Technology Corporation, revolutionized the marine seismic industry further when he invented the PAR air gun in 1964 (SEG, 2006). The interest for marine seismic exploration was growing. Digital technology drastically changed the nature of seismic instrumentation and in 1967 Exxon performed the first 3D seismic survey near Houston. In the 1990s, solid streamers became available and the GPS satellite network improved the positioning. Today, the receivers are much smaller and efficient than before and PGS' vessel, Ramform Titan (launched 2013), can tow up to 24 streamers of 12 km, covering an area equivalent to nearly 1500 soccer pitches, or 3,5 times Central Park (PGS, 2014). The need for data power has also led to innovations in the processing part of the industry, and many ways of manipulating the data have become available. The more attractive solutions on the market today concentrate on obtaining broadest possible frequency bandwidth. In many ways, broadband seismic can be understood as ghost-free data and the focus on eliminating the ghost effect is therefore the core in all of the proposed solutions. The role of which octaves (the interval between one frequency and another with half or double its frequency) play in the data will be discussed in the next section.

3.2 Broadband benefits

Broadband seismic is a common term directed towards the bandwidth of the useful seismic data in the recordings. Conventional data typically contain frequencies between $8 - 80$ Hz, while the newest broadband systems claim to deliver a bandwidth from 2.5 Hz up to 200 Hz. The advantages that follow from this extended range of frequencies can be recognized mainly from:

- Improved resolution
- Improved penetration
- Improved seismic inversion

3.2.1 Resolution

For clarity, the concepts of phase, polarity and wavelets need to be familiar in order to evaluate seismic resolution. Simm and White (2002) provides a tutorial on these key terms. The phase describes the relative timing relationships of the various frequency components that make up the seismic wavelet. So called zero-phased wavelets are symmetrical with the dominant loop corresponding to the reflection from the acoustic boundary. If the timing between the dominant loop and the impedance contrast are non-zero, the wavelet can be said to be causal. A special case of causal wavelets is when the wavelet is building up the energy in the minimum time. This phase characteristic is often referred to as minimum phase. Common seismic sources, such as explosives and the air gun, have minimum phase signatures. From this definition, the minimum-phase wavelet can have a variety of shapes. Regarding symmetry, the descriptive term is phase rotation where a negative phase rotation delays the main peak and a positive phase rotation advances the peak in time. For the seismic interpreter, the optimal wavelet is the symmetrical zero-phased wavelet. In seismic processing, a shaping filter is therefore often applied to convert to zero-phase. Information of the wavelet shape from either measurements, wells or unique reflections can be used for such source signatures. Another concept in wavelet characterization is polarity. Considering a symmetrical wavelet, the polarity indicates if the dominant loop is a peak or trough when passing a defined acoustic impedance boundary. For a hard reflection, which indicates an increase in acoustic impedance, the polarity convention according to Society of Exploration Geophysicist (SEG) is positive and displayed as a peak. For a soft reflection or decrease in acoustic impedance, the SEG polarity is negative and displayed as a trough. In this discussion of seismic resolution, the wavelet is assumed zero-phased with positive polarity.

Seismic resolution can be divided in temporal and spatial resolution. Temporal resolution is understood as the ability to distinguish two features with different depths from one another. The critical parameter influencing this ability is the dominant wavelength in the seismic signal. The accepted geophysical principle with respect to resolution is the

one-quarter wavelength condition, also known as the Rayleigh criterion (Kallweit and Wood, 1982). This limit defines the minimum bedding thickness needed for resolved recordings. How reflections can be classified as resolved or unresolved is ullustrated in **Fig. 3.1**. The wavelength λ is related to the velocity v and the frequency f as

$$\lambda = \frac{v}{f}. \tag{3.1}$$

This means that the highest frequencies are the controlling factor of the resolution ability in the seismic data. However, the low frequencies do also play an important role. How the high and low frequencies affect the wavelet is illustrated in **Fig. 3.2.** When increasing the high end, it is clear that the main peak is sharpened. When keeping the high frequencies fixed and increasing the low frequency content, one can observe that the side lobes of the wavelet diminishes. This also increases the resolution of the data as these side lobes will be less likely to hide other reflections that coincides with them.

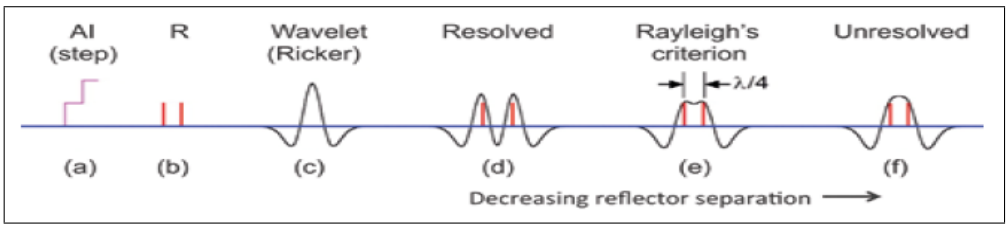

Figure 3.1 – *(a) An acoustic impedance model with two positive increases. This leads to equal reflectivities as shown in (b). (c) With a zero-phased wavelet, the resolved situation in (d) needs to satisfy the Rayleigh criterion in (e) to avoid the unresolved situation in (f). Source: Landrø and Amundsen (2013a).*

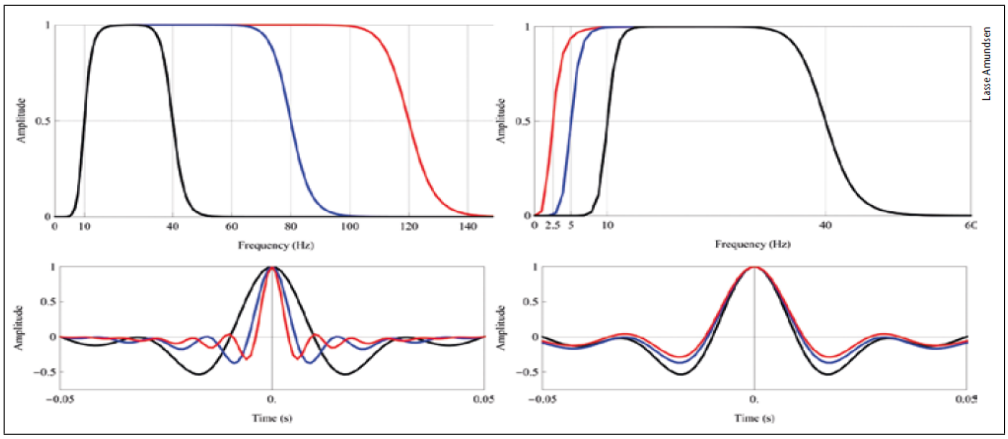

Figure 3.2 – *By increasing the octaves from 2 (black) to 3 (blue) to 4 (red) while keeping the lowest frequency fixed, the dominant loop of the wavelet is sharpened. By extending the low frequency side with the same number of octaves, it is clear that the side lobes diminish while the dominant loop nearly is unaffected. Source: Landrø and Amundsen (2013a).*

Spatial resolution can for instance be described by Fresnel zones, where the Rayleigh criterion also is valid. In this case, the area of where the seismic wavefront is displaced by $\lambda/4$ is defined as the limit of area that can be seen. However, on migrated data this area is considerably reduced. Another way of quantifying spatial resolution is from the shape of the post-migrated spatial wavelet, which can be defined as the migrated point diffractors response after bandlimiting the temporal spectrum. Inspired by this method, first described by Berkhout (1984), Landrø and Amundsen (2013a) found how the high frequencies sharpens the spatial wavelet and that the low frequencies reduces the side lobes. Hence, good temporal resolution is needed for good spatial resolution.

3.2.2 Penetration

The absorption equation was given in 2.2.1. It is convenient to take another look at this equation to understand why broadband data have better penetration ability than conventional data:

$$A = A_0 e^{\frac{-\pi f t}{Q}}. \tag{3.2}$$

Q is assumed to be frequency independent. It is then clear from the equation that the low frequencies have greater penetration capability than the high frequencies. This will be especially important in situations where the lithology is highly absorbing, such as salt and basalt. Presence of such lithologies obscures the seismic image and hides the geology lying below. This area might be important in hydrocarbon exploration. It is well known that salt can behave as a trap for oil and gas and imaging of subsalt layers might reveal unknown accumulations, even in mature basins. Since broadband systems now may deliver frequencies as low as down to 2.5 Hz, broadband data can illuminate areas that up to now have been impossible to see on conventional data.

Kroode et al. (2013) illustrate how seismic waves behave differently for low and high frequencies when inhomogeneities are present. A simple three layer model was constructed where the interface between layer one and two is of a sinusoidal character with wavelengths of 15 meter and amplitudes of 7.5 meter. This irregular surface shape can create a complex scattered wavefield. An important difference between the low frequency (10-15 Hz) and high frequency (50-80 Hz) response when they are subjected to this synthetic model is seen in **Fig. 3.3.** The spectrums indicate an almost undisturbed response for the low frequency part and a complicated affected response for the higher frequencies. Often related to absorbing lithology is the irregular vertical and lateral distribution of these layers. Both salt and basalt comes in many forms which can produce scattered wavefields. In terms of penetration, it can therefore be noted that, in addition to experiencing less absorption, the low frequencies can penetrate inhomogeneities with a coherent wavefront. The sum of the absorption and scattering effects constitute the reason why the low frequencies are more important than the high frequencies for deep penetration, especially below complex lithology.

Another interesting situation discussed in Kroode et al. (2013) is when there is a gas cloud obstructing proper imaging. Commonly, one assumes that absorption is the dominating factor of this problem. However, the authors argue that the problem might be equally related to the velocity model. The low velocity of gas often gives large abrupt contrasts to the surroundings that can results in a complex wavefront. The moveout can therefore vary significantly from trace to trace, leading to difficulties in velocity picking. Here, the lowest frequencies might be helpful to build a more accurate model because they allow better picking. An example in their paper shows a remarkable improvement when basing the velocity model on broadband seismic data rather than conventional data, illustrating that penetration also is improved indirectly from the low frequencies in terms of better velocity estimations.

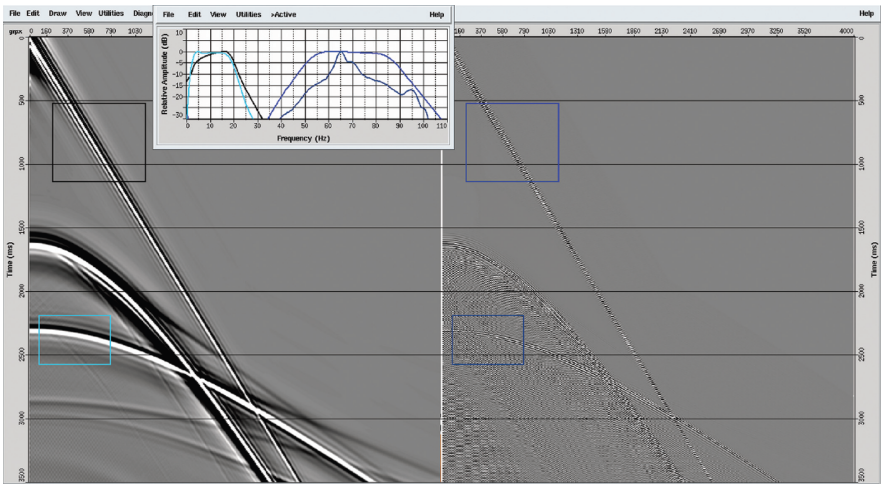

Figure 3.3 – *The synthetic modelling of reflection responses to a rugose layer reveals that the low frequencies, on the left side, are less affected than the high frequencies, shown on the right side. This is best seen from the frequency spectrums of the two, where the layer responses are compared to the direct wave responses. Source: Kroode et al. (2013).*

3.2.3 Inversion

From a geological point of view, the layer boundaries built up from the seismic reflectivity reveal much of the structural evolution of an area. However, the rock properties hiding between are really what an interpreter is interested in for reservoir characterization. To extract properties like p-wave velocity, s-wave velocity and density from the seismic data, another way of visualizing the seismic section is needed. The process of seismic inversion might provide such insight and can act as a bridge between the geophysicist and the geologist. The present inversion technologies can be complicated and ranges from post-stack to pre-stack with implementations of acoustic, elastic or shear wave elastic cases. The final inverted results are influenced by a number of factors, including petrophysical measurements, well log data, well-seismic data calibration, processing and

interpretation of seismic data, the accuracy and ambiguity of inversion algorithm as well as resolution (Desheng et al., 2009). The method developed by Lindseth (1979), often called Seislog, will be discussed for illustration purposes. The simplest 1D case is assumed where the boundary of layer 1 and 2 gives a zero offset reflection coefficient as

$$R = \frac{Z_{i+1} - Z_i}{Z_{i+1} + Z_i}, \tag{3.3}$$

where Z_i is the acoustic impedance of layer i. Z_{i+1} can then be found:

$$Z_{i+1} = Z_i \frac{1+R}{1-R}. \tag{3.4}$$

In this way, the acoustic impedances of each layer can be extracted and displayed on plots with colour scales representing the acoustic impedance values. Huang et al. (1995) showed that the frequency bandwidth has the single largest effect on the inversion. Although he did not examine the low frequency effect, he proved that the result is very sensitive to the high frequency content. In Lindseth (1979), the effect of the low frequencies are better explained. A sonic log with frequencies from $0 - 250$ Hz is composed of a 0-5 Hz component and a 6-250 Hz component. By removing the signal derived by the lowest frequencies, the accuracy decreases. This is illustrated in **Fig. 3.4**. In conventional seismic data, the typical $0 - 5$ Hz signal is missing. If broadband data can deliver such low frequencies, seismic inversion results will be more accurate. This can be especially important in areas where well data are sparse, such as in frontier exploration. A demonstration is given in **Fig. 3.5** where Kroode et al. (2013) performed an impedance inversion for both conventional bandwidth data and broadband data over the same area. The interpretation of how the sand bodies are distributed can clearly be done with a higher degree of certainty with the broadband inverted data.

Full waveform inversion (FWI), introduced by Tarantola (1984), has seen renewed interest recent years because of progress in computer power technology. The method is based on a matching between modelled and recorded data to obtain interval velocities. From an initial velocity model and input wavelet, a computation of a forward-propagating wavefield using the wave equation provides simulated recordings at each receiver location. These can be compared with the real recorded data. The target of FWI is to minimize the difference between recorded and modelled data in a least squares computation. After forward propagation, the wave equation is run in reverse with this difference as a new source. This provides the velocity gradient and in which direction the spatial velocity model must be extended or reduced. The cycle can then be performed again. FWI demands low frequencies and sufficiently long offsets to deliver the first large scale changes to the initial model. Broadband seismic can therefore be very valuable for velocity models obtained from FWI (Kelly et al., 2009). How the inversion is improved by increasing the bandwidth on the low frequency side is illustrated in **Fig. 3.6.**

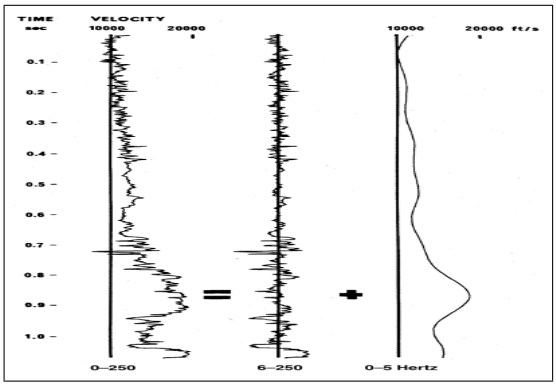

Figure 3.4 – *The correct sonic log on the left consists of the 6-250 Hz in the middle and the 0-5 Hz data on the right. Without the log derived by the lowest frequencies, the accuracy of the velocity representation decreases. Source: Lindseth (1979).*

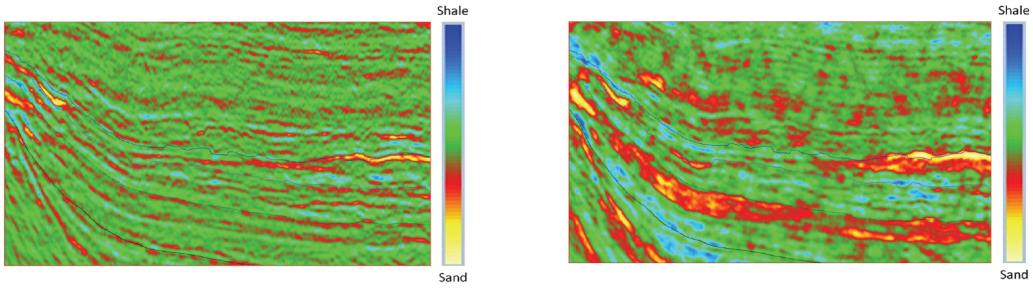

(a) *Conventional data inversion* **(b)** *Broadband data inversion*

Figure 3.5 – *(a) Conventional inversion does not enable easy interpretation of the sands. (b) Broadband data inversion reveals the pinch-out of the sand that not could be seen in (a). This sand body can be seen on the middle right side in (b). Source: Kroode et al. (2013).*

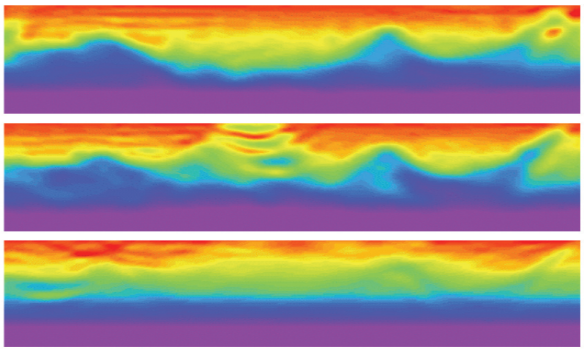

Figure 3.6 – *FWI using three different frequency bands. Top picture shows a FWI with 1,5-5 Hz input, middle picture shows the result with 2-5 Hz, while the lower picture represents 4.5-5 Hz. The geology becomes more visible as the low frequency content is increased. Velocities ranging from 1500 m/s (red) to 6500 m/s (purple). Source: Kroode et al. (2013).*

3.3 Broadband technologies

The notches in the frequency spectrum limits the information extracted from the seismic data. In complex areas and in high end reservoir interpretation, it is crucial to have largest possible bandwidth. The responsible for this limitation are the ghost waves due to the free surface. Appropriate exorcism of these ghosts has therefore been a subject of study since the mid-1950s (Landrø and Amundsen, 2013b). However, the problem has been seriously revisited the latest years due to technological improvements in both acquisition and processing (Moldoveanu et al., 2012). On the receiver side, four main solutions have been proposed that forms the foundation of the leading available solutions on the market today:

- Slant streamer (Ray and Moore, 1982)
- Dual sensor measurements (Berni, 1985)
- Over/under streamer (Sønneland et al., 1986)
- Multicomponent (4C) towed-streamers (Robertsson et al., 2008)

The idea of the slant streamer is that the receiver ghosts vary as the receiver depth varies along the streamer profile. The advantage of this is that the obtained signal contains continuous information from the lowest to the highest recorded frequency. Hence, the ghost notches can be stacked out of the data. At the time this method was presented, the processing technology was not sufficient to successfully handle the streamer profile and especially the ghost-removal process. In 2010, Soubaras and Dowle (2010) of Compagnie Générale de Géophysique (CGG) introduced an algorithm which was designed to remove the ghosts in a migration-mirror migration and a joint deconvolution operation. This formed the flagship of CGG's broadband solution, BroadSeis™. It is based on the concept of Ray and Moore (1982), but uses a variable-depth streamer profile with angle variations rather than a linear solution. WesternGeco does also offer a solution based on the slant streamer principle which they have named ObliQ™.

The theory of pressure wavefield recordings and particle velocity recordings yielding complementary information was understood in the early days of seismic exploration. Berni (1985) patented such a system using combined measurements from hydrophones and geophones. The very first broadband method presented was based on this concept. In 2007, Petroleum Geo-Services (PGS) revolutionized the industry when they introduced the GeoStreamer™, a dual component streamer measuring the pressure and velocity simultaneously (Carlson et al., 2007). Since the pressure ghost notches occurs at frequencies where particle velocity recordings contain information, the measurements can be combined such as separation of upgoing and downgoing wavefields can be accomplished, which is the core criterion of deghosting algorithms.

To reduce weather downtime because of swell noise, the over/under principle was developed after ideas from Sønneland et al. (1986). With two streamers at different depths,

two datasets with different ghosts will be recorded and combined to achieve full bandwidth seismic data. Lack of precise streamer maneuvering in the 1980's made the method difficult to perform in practice. Due to new advanced streamer positioning technology coming forward the latest years, this method is again discussed actively.

From the multicomponent streamer, pressure and 3D measurements of particle acceleration are provided from hydrophones and special accelerometers known as micro electromechanically systems (MEMS). The acceleration data can be used to derive the pressure gradient which in turn composes the missing part needed in wave separation and therefore deghosting (Robertsson et al., 2008). Because of the y-measurements, the multicomponent streamer can also reconstruct the wavefield in crossline direction. This method has been baptized IsoMetrix™ by WesternGeco. GeoStreamer, IsoMetrix and BroadSeis seem to have secured the place as the leading broadband solutions available on the market today. It is therefore of interest to discuss these three technologies further.

3.3.1 PGS' GeoStreamer

The ghost function for zero offset hydrophone measurements, hereby called P-recordings, can be expressed as

$$G_- = 1 - e^{-i\omega\tau} \tag{3.5}$$

with a frequency spectrum of

$$|G_-(f)| = 2|\sin(\frac{2\pi f z}{c})|. \tag{3.6}$$

Here, z is the receiver depth, c is the water velocity, ω is the angular frequency ($=2\pi f$) and τ is the ghost delay time ($= 2z/c$). Since the geophones are measuring the difference between upgoing and downgoing vertical wavefield, hereby called Z-recordings, the particle velocity ghost function becomes

$$G_+ = 1 + e^{-i\omega\tau} \tag{3.7}$$

with a frequency spectrum of

$$|G_+(f)| = 2|\cos(\frac{2\pi f z}{c})|. \tag{3.8}$$

Comparing these frequency spectrums reveal that the notch frequencies for Z-recordings are laying mid-between the notches in the P-recordings. Hence, the two measurement techniques yield complimentary information and may be combined to a broadbanded

signal. This was the motivation behind the first patent received by Berni (1985). For a reflection response of R, the P recordings can be formulated as

$$P \sim RG_{-} \tag{3.9}$$

and the Z-recordings as

$$Z \sim RG_{+}. \tag{3.10}$$

For correct scaling, these can then be combined from the relation:

$$\frac{1}{2}(P + Z) = R. \tag{3.11}$$

However, this theory has been well known for many years and successful progress in ocean bottom seismic (OBS) systems have been accomplished after the introduction by Barr and Sanders (1989). In marine towed streamer acquisition, installation of motion sensors in proper direction has proved to be very difficult. In addition, the high noise level in the streamer cables made the practical applications limited. The lowest frequencies were especially challenging because of strumming interference. The theoretical foundation and potential behind this technology motivated the geophysicists in PGS to investigate the possibility of applying such motion sensors on the streamers in the early 2000s (Landrø and Amundsen, 2013d). After encouraging results on the high frequency content from tests in 2001, a patent was filed and the project continued. However, the low frequencies were still affected by noise. In 2005, PGS filed a new patent, this time they claimed to have solved the low frequency problem. It turned out that the theory behind their method was already available, first presented by Amundsen (1993) and revisited in Amundsen et al. (1995). The relation between P and Z can be expressed as:

$$Z \sim \frac{G_{+}}{G_{-}}P. \tag{3.12}$$

For particle velocity data containing much noise, the Z-recordings can actually be estimated from the P-recordings. By multiplying P with G_{-} and this result with G_{+}, the estimate is obtained. This deghosting-ghosting can also be referred to as PZ summation and constitute a major part of the GeoStreamer success. In practice, PGS uses a low-cut filter on the noise dominated low frequency Z-recordings, and then they estimate this part using Eq. 3.12. The higher frequency Z-recordings with acceptable noise level is then merged with the estimate. After this, the P-recordings are merged, which gives a bandwidth exceeding the conventional range (Tenghamn et al., 2007). The PZ summation is illustrated in **Fig. 3.7.** An important observation is the dependence on high S/N P-recordings. Since the Z-recordings now are providing information at the pressure notch frequencies, the streamer can be towed deeper, yielding less noise in the data.

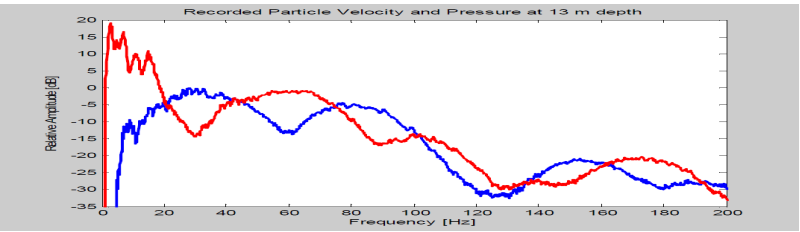

(a) *Raw data*

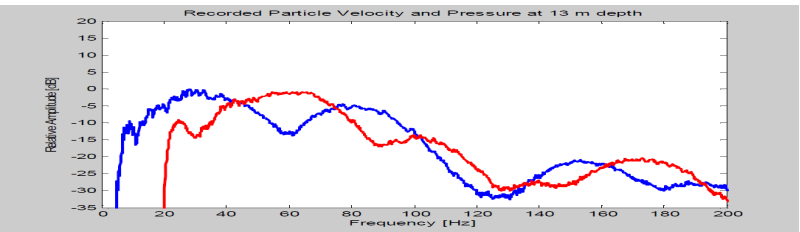

(b) *Low-cut filtered Z-recordings*

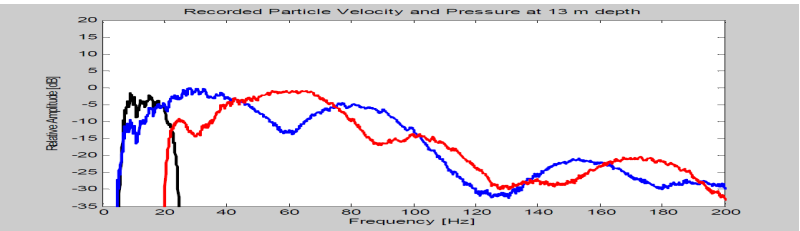

(c) *Estimation of low frequency Z-recordings*

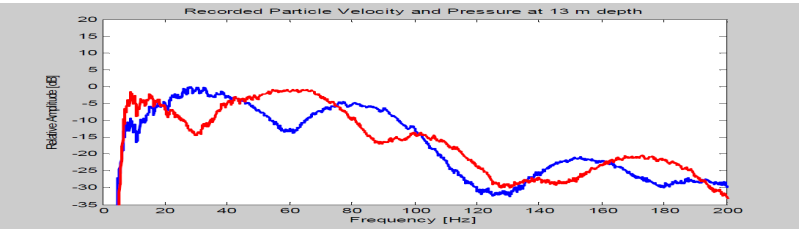

(d) *Merged Z-recordings*

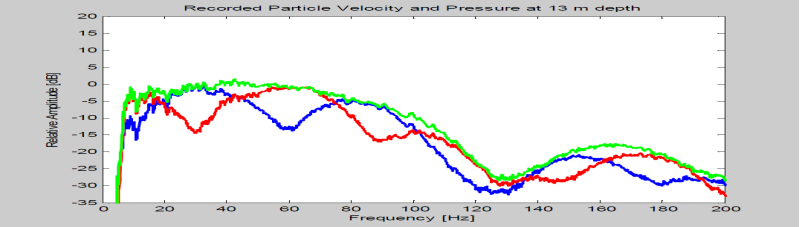

(e) *Merged P and Z-recordings*

Figure 3.7 – *The principle of estimating the low frequency particle velocities. Red = geophone data, blue = hydrophone data, black = geophone estimate, green = total merged data. The noisy low frequency part in a) is filtered to b). The estimated geophone data is displayed in c) and merged into the recordings in d). By combining the two datasets, a broadband signal is obtained, illustrated in e). Source: Tenghamn et al. (2007).*

3.3.2 CGG's BroadSeis

Geophysicists have for a long time been well aware of the possible benefits from the notch diversity obtained from slanted streamers (Ray and Moore, 1982). Despite this, successful applications of the method have been missing. An obvious reason is that the streamer profile introduces challenges in the processing. The beneficial variable receiver ghosts have also turned out to be a problem. Conventional processing algorithms assume a flat streamer with wavelets and ghosts approximately constant against offset. The insufficient processing technology led this method to stay on hold until 2010 when Soubaras and Dowle (2010) from CGG finally succeeded in developing a way of deghosting variable-depth streamer (VDS) data. Although building of the concept of the slanted streamer, CGG's new solution was a further developing of the technology. Their method, which got the name BroadSeis™, uses a curved profile down to a specific depth where the streamer flattens. In general, this enables favourable recordings of high frequencies to be done in the curved part while the low frequencies are favoured in the deep flat part. The streamer profile can further easily be optimized for specific requirements from the acquisition area. How the VDS exploits the diversity in ghost notches is explained in **Fig. 3.8**. The initial presented deghosting solution produces a migrated dataset and a mirror migrated dataset, resulting from an imaginary mirror cable above the surface, that can be combined through a joint deconvolution process. The method is sketched in **Fig. 3.9**. This de-ghosting algorithm was produced for post stack data. Later, the method was further developed to handle pre-stack data (Soubaras, 2012). However, keeping the ghosts untouched through all of the processing stages can be considered as problematic. In general, noise should be removed early in the processing to prevent interference and artefacts when other algorithms are executed. CGG have therefore developed other methods described in for instance Wang et al. (2013) and Poole (2013), which are now commonly used in BroadSeis production projects. Soubaras' method is, however, important as it represent the breakthrough of the BroadSeis adventure. It might also still provide the best deghosting in areas with very complex 3D structures.

With regards to other seismic applications, such as time-lapse seismic (4D) and Amplitude vs offset (AVO) analysis, challenges related to the streamer profile are obvious. How the amplitudes responds to increasing offsets are commonly used as a fluid indicator in petroleum exploration. The derived literature on the subject focuses on conventional flat streamer analysis. For 4D seismic, a key issue of successful applications is the repeatability of the involved surveys. The most prominent issue for VDS is here the receiver location differences. A recent important development for BroadSeis has therefore been redatuming of the data to a desirable level, such as the sea surface, or for 4D, a receiver depth coinciding with a legacy survey. This option has now been implemented in the deghosting methods given above. In this way, CGG can use processing algorithms invented for flat streamers. Soubaras (2012) also shows that BroadSeis is AVO applicable. Recent studies by Hicks et al. (2014) show that 4D-coprocessing of conventional flat streamer data with a VDS broadband monitor can be done efficiently with a well match using the ghost wavefield elimination (GWE) and redatuming method from Poole (2013).

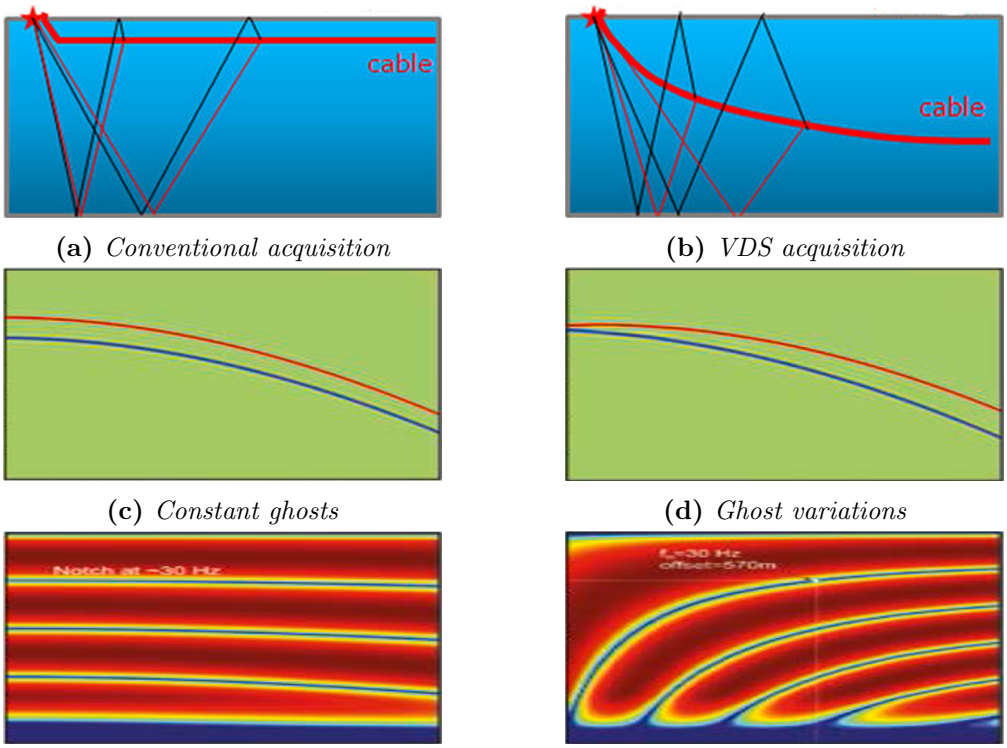

(a) *Conventional acquisition* **(b)** *VDS acquisition*

(c) *Constant ghosts* **(d)** *Ghost variations*

(e) *Constant notches* **(f)** *Notch diversity*

Figure 3.8 – *A comparison between flat streamer and VDS acquisition. The conventional flat streamer in a) and a VDS profile in b). c) and d) provides an illustration of how the receiver ghosts vary along the cable for flat streamer and VDS. This results in constant ghost notches for conventional acquisition and notch diversity for VDS data, showed in e) and f), respectively. Source: CGG (2014b).*

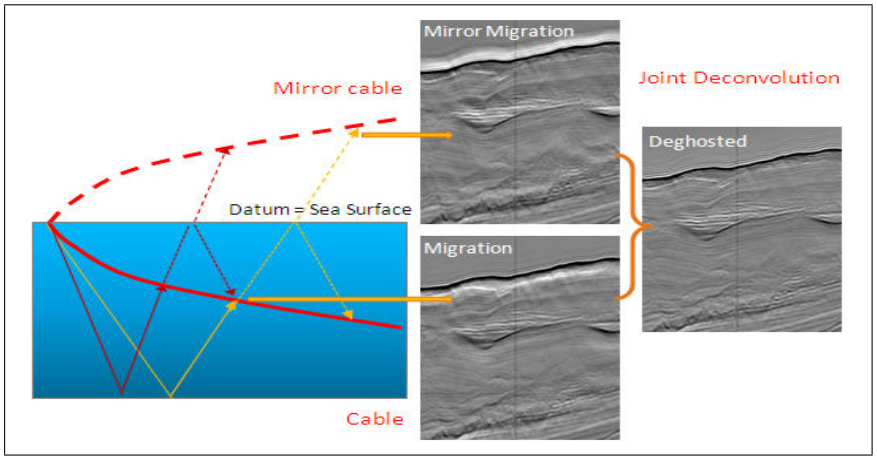

Figure 3.9 – *Deghosting of VDS data can be performed by a migration and a mirror migration that can be combined through a joint deconvolution process. Source: CGG (2014b).*

3.3.3 WesternGeco's IsoMetrix

The IsoMetrix marine seismic service was launched during European Association of Geoscientists and Engineers (EAGE) 2012 annual conference and exhibition. This product was the end result of the biggest engineering project ever undertaken by Schlumberger. It lasted for 10 years and in addition to the newly presented acquisition system, corresponding algorithms and workflows were developed (Harries, 2012). Essential in the technology is WesternGeco's Nessie-6 streamer, delivering data of pressure and MEMS-based measurements of acceleration that can be used to provide vertical velocity, V_z and crossline velocity, V_y. Nessie-6 is illustrated in **Fig. 3.10**. With this information, WesternGeco have the input needed for the PZ-summation explained in 3.3.1. Although their measurements are not used for low frequency estimation, as PGS does with their GeoStreamer data, the receiver ghost can be removed using the same principle of complimentary information given by pressure and particle velocity (Caprioli et al., 2012). The Nessie-6 streamer can therefore be towed deeper providing more low frequencies and hence, be called a broadband seismic method.

However, the core of the IsoMetrix technology is in addition related to crossline acceleration measurements. In the marine setting, due to safety and practical reasons, a certain separation is needed between the towed streamers, typically 50 meters. Inline spatial sampling is often 3.125 meter, which means that cross-line spatial sampling is 16 times sparser. WesternGeco therefore believe that common 3D seismic acquisition actually is more a 2,5D acquisition since the wavefield not can be estimated accurately without aliasing. Aliasing can be understood as misinterpretation of data because of insufficient information. This is explained further in **Fig. 3.11**. From IsoMetrix data, WesternGeco claims to accurately reconstruct the wavefield in cross-line direction, providing full 3D seismic acquisition. This is based on theory from Robertsson et al. (2008). With access to the gradient of the pressure wavefield, the reconstructed signals can be sampled twice as coarse compared to pressure-only data.

To take advantage of the new information, WesternGeco developed a technique with simultaneous reconstruction and deghosting of seismic wavefields. The method is called generalized matching pursuit (GMP) (Özbek et al., 2010). Although it can be used with two component input (P and V_y), the technique yields superior interpolation with three component data (P, V_z and V_y). The advantages of a denser grid in crossline direction are several. Apparently random noise might prove to be coherent, enabling better modelling and subtraction in denoising algorithms early in the processing. Returns from geologic fault planes that run across the streamer spread might be observed. With regards to 4D, good cross-line wavefield propagation understanding is desirable as the data can be matched to the location of the base survey which increases the repeatability (Smith et al., 2013). An example from an IsoMetrix test survey from 2011, illustrating the better interpretability obtained from crossline wavefield reconstruction, can be seen in **Fig. 3.12**.

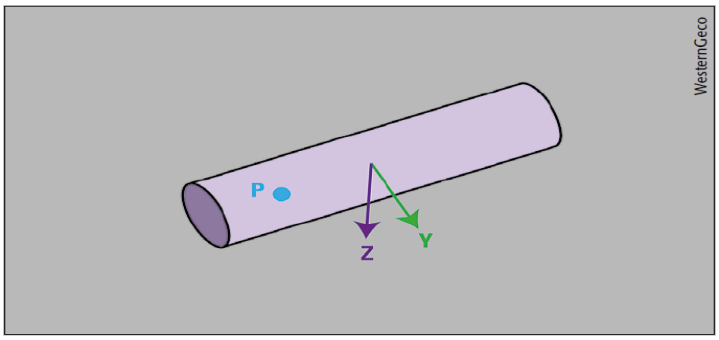

Figure 3.10 – *WesternGeco's Nessie-6 streamer provides hydrophone data in addition to acceleration data in y and z direction. Source: Harries (2012).*

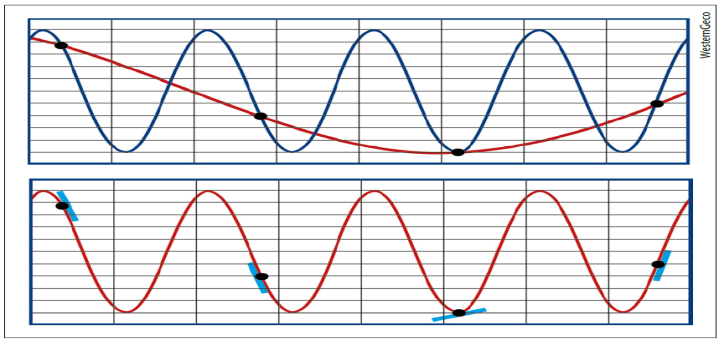

Figure 3.11 – *The blue waveform on the top figure represents the actual signal. The red waveform on the same figure is the reconstructed signal from the pressure recordings marked by the black dots. The lower figure shows that the actual signal can be reconstructed correctly with information of the gradients in addition to the pressure. The phenomenon occurring to the top red waveform is called aliasing. Source: Harries (2012).*

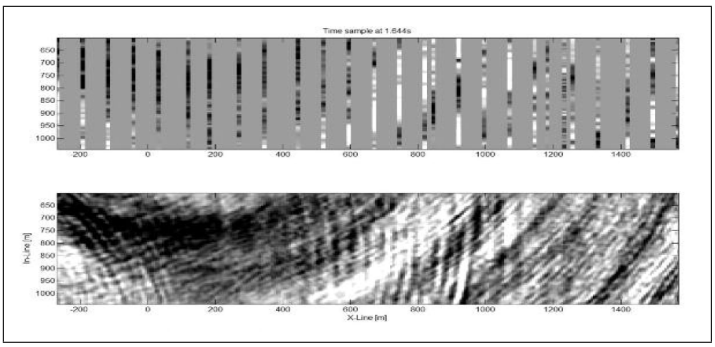

Figure 3.12 – *The figure shows an IsoMetrix test survey from 2011. The streamers were separated by 75 meters and are displayed vertically on the figure. The conventional lines on the top transform to a detailed unaliased crossline wavefield with the IsoMetrix technology, shown in the bottom figure. Source: Harries (2012).*

3.3.4 Source ghost solutions

The receiver ghost problem can, to some extent, be considered solved with the newly born techniques. However, the sea surface is also present on the source side, limiting the information due to the source ghost notch. To inject an even broader bandwidth signal into the earth, this phenomenon must also be investigated. The proposed methods have many similarities to the concepts used on the receiver side. Moldoveanu (2000) presented a configuration based on the over/under idea. It requires flip flop shooting of two sources deployed at different depths with a horizontal separation equal to the shot point interval. The idea is to combine the complimentary ghost functions to obtain the deghosted data. One downside with this technique is that the shot-point density will be reduced. As attention towards the source ghost has increased the latest years, two other solutions have developed.

Based on an old land acquisition technique proposed by Shock (1950), the source ghost can alternatively be attenuated using a beam steering technique. Several sources can be arranged in depth and fired with small time delays equal to the travel times between the sources, allowing the downgoing primary signal to be summed constructively and the ghosts to interfere destructively (Cambois et al., 2009). How the operation is performed is illustrated in **Fig. 3.13.** This requires exact knowledge of the medium between the sources. In contrast to land acquisition, this medium is well known in the marine setting. The water velocity can therefore be used to find the firing time intervals between the different sources. With this defocusing of the ghost waves, infill around the notches will be enabled. On the other hand, the boosting effect will be lost. A specific challenge related to this technique is the radiation pattern. A 3D spatial distribution of airguns across the layer depths is necessary to maintain the same directivity quality as for standard source arrays (Siliqi et al., 2013). This complex configuration and the interaction between the components involved makes it challenging to produce a good model of the source signature. For building high quality source de-signature operators, near-field hydrophones might provide valuable additional information (Poole et al., 2013). CGG base their BroadSource™ (CGG, 2013) solution on this synchronized multi-level source theory. In combination with their BroadSeis acquisition, they claim to deliver frequencies from 2.5 Hz up to 200 Hz (Sablon et al., 2013).

The theory behind PGS' GeoSource™ (PGS, 2011) solution can be found in (Parkes and Hegna, 2011a). The principle is that sources deployed at different depths yields complimentary information and can be combined to achieve ghost free data, as explained in **Fig. 3.14.** The GeoSource is a time- and depth distributed source divided in sub-sources consisting of conventionally tuned sub-arrays at different depths. The acquisition is done in a randomized way where at least one of the sub-sources is fired with a time delay, typically of less than one second. The energy from the different sources will interfere, but this can be handled in the processing with so called de-blending techniques. However, this separation of wavefields represents the main challenge with the technique. PGS claim that the GeoStreamer combined with GeoSource also can deliver frequencies

up to 200 Hz. The many different seismic companies will probably offer equally many solutions to the source ghost problem. However, they are in general all based on a multi-level distribution and either one of the concepts of synchronization or simultaneous sources. For instance does WesternGeco use the simultaneous source principle in their SimSource™ solution (Beasley et al., 2012). Shen et al. (2013) examined theoretical design principles with regards to multi-level sources. They recommend three or four depth levels to be ideal for combining deghosting and operational feasibility.

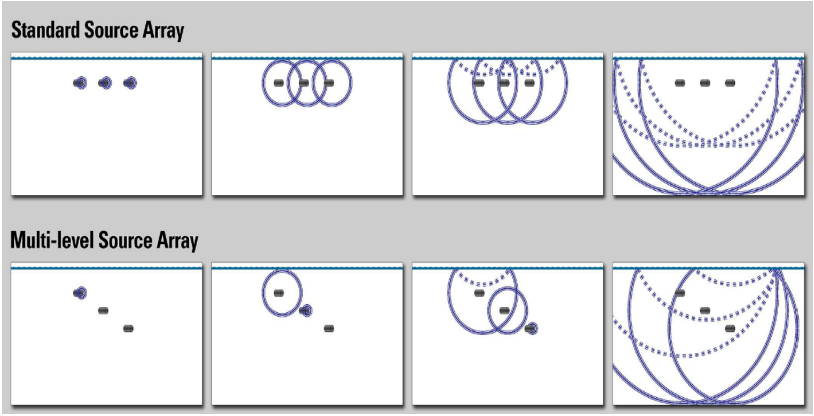

Figure 3.13 – *The idea of the synchronized multi-level sources. Top figure illustrates how a conventional source configuration emits a constructive primary signal, but the ghost propagates with the same strength behind due to the constructive interference. The synchronized multi-level sources, displayed in the lower figure, produces a constructive sum of the first wavefronts, but the ghost wave pattern is defocused and hence, the ghost effect reduced. Source: Parkes and Hegna (2011a).*

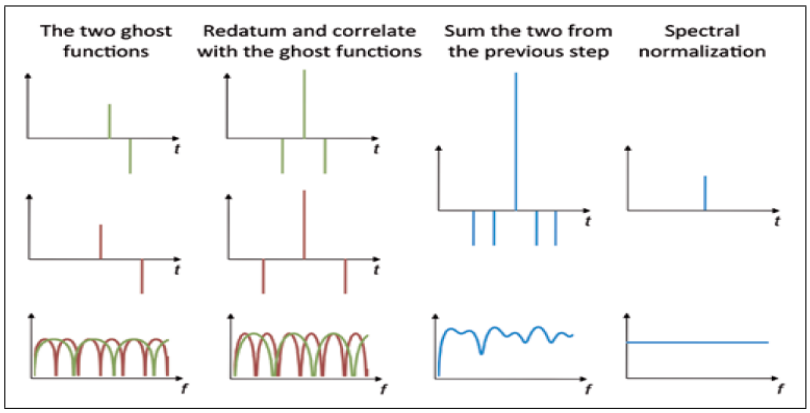

Figure 3.14 – *The principle of the GeoSource. After wavefield separation, the two ghost functions on the left can be correlated and combined as shown in the left middle figure. This attenuates the source notch, as can be seen in the amplitude spectra on the middle right figure. A spectral normalization is applied to obtain smoothly data, illustrated as the right figure. Source: Parkes and Hegna (2011a).*

3.3.5 Data example

In this section, a comparison between conventional data and BroadSeis with BroadSource is given in **Fig. 3.15** to illustrate the remarkable uplift with broadband seismic. The two sections represent exactly the same area.

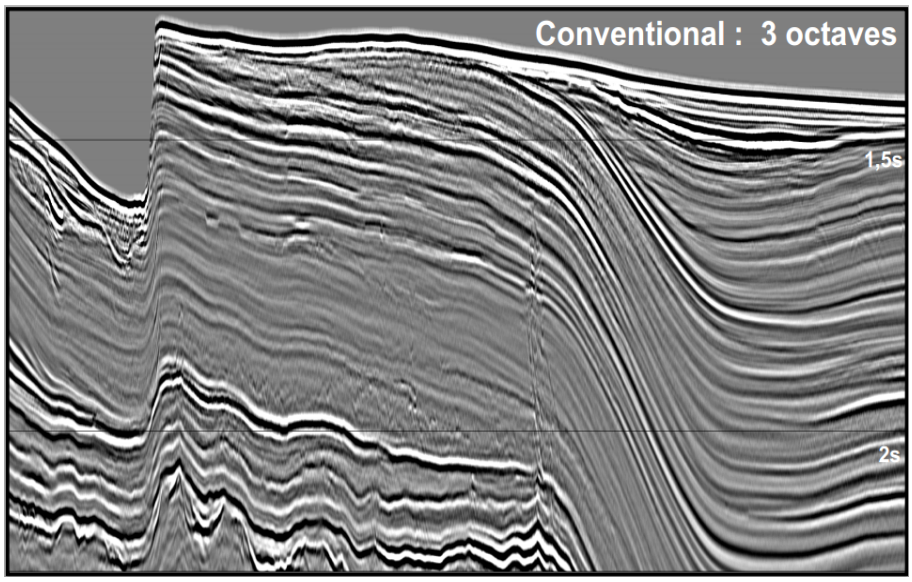

(a) *Conventional bandwidth*

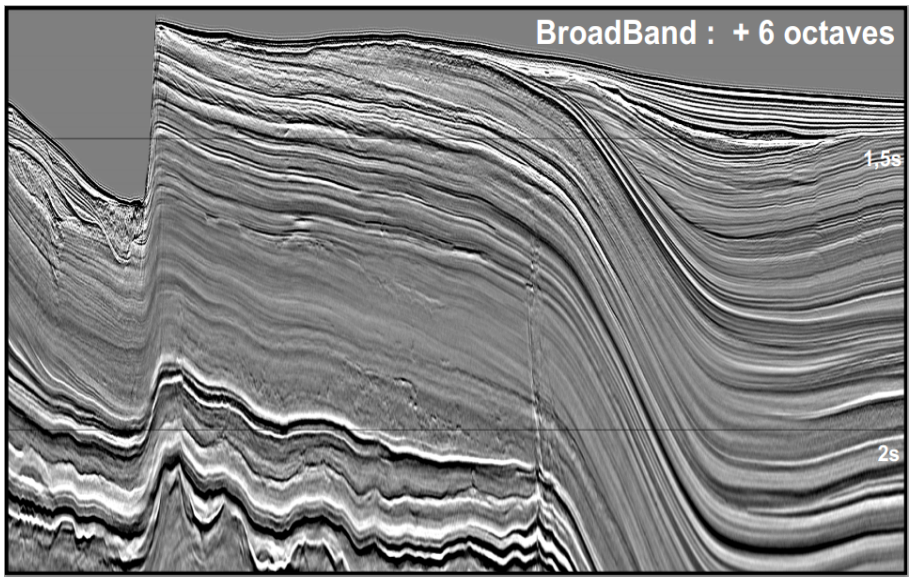

(b) *Broadband seismic*

Figure 3.15 – *A comparison between conventional seismic (a) and broadband data (b). Source: Internal CGG data.*

Chapter 4

Low frequency acquisition

Through the previous chapter, the benefits of an extended amplitude spectrum on the low frequency side was demonstrated. In summary, the low frequencies enable better resolution, better penetration and improved seismic inversion. The described broadband techniques use clever solutions, mainly on the receiver side, to tow deeper where S/N is higher. This enables the low frequencies to be collected better than before. A natural continuation is then to investigate what specific limitations that need to be handled to generate the low frequency content and the recording equipment involved.

4.1 Source output

As given and explained in 2.1.1, the bubble oscillation period can be expressed as

$$\tau = k\frac{P^{\frac{1}{3}}V^{\frac{1}{3}}}{(P_{\text{atm}} + \rho g z)^{\frac{5}{6}}}. \tag{4.1}$$

For an air-gun with a fixed firing pressure and volume, it can be seen from Eq. 4.1 that the time period increases when the hydrostatic pressure decreases. An important relation with the bubble time period is the fundamental frequency, or the resonance frequency:

$$f = \frac{1}{\tau}. \tag{4.2}$$

This means that the fundamental frequency of an air-gun goes towards lower frequencies when the source depth is decreasing. A lower fundamental frequency means that the signal peak in the amplitude spectrum is lowered. From this, it follows that the data

below this value also is improved due to the inclination or envelope of the filter. However, Landrø and Amundsen (2014) show with a simplistic derivation that the bubble oscillations creates notches in the amplitude spectrum according to

$$f_n = \frac{n + \frac{1}{2}}{\tau}. \tag{4.3}$$

The preferred time-period increase will therefore suffer from bubble notches when moving towards lower frequencies. Evidence of this can often be seen in seismic aiming at deep imaging when so called ringing (repeating appearance) can be seen around these low frequent reflections. This indicates that more focus should be directed against bubble attenuation when increasing the gun volume (increasing τ) in the survey. Therefore, if debubble operators are successfully applied, it is reasonable to assume that the low frequency behavior of an air-gun is better when towed shallow.

Unfortunately, the ghost effect from the free surface also affects the low frequency output. For a reflection coefficient of -1, the ghost equation becomes

$$|G(f)| = |2 \sin \frac{2\pi f z}{c}|. \tag{4.4}$$

For $f = 0$, the amplitude of the ghost filter will always be zero. When increasing the frequency, the amplitude gradually increases depending on the other involved parameters. Of specific interest is the depth of the source, z. For deep towing, the source notch is moved towards lower frequencies, leading to a steeper inclination of the ghost envelope. Therefore, towing the source deep favours the low frequency end of the spectrum. A weaker reflection coefficient than -1, would give less pronounced attenuation on the low frequency side of the spectrum (Landrø and Amundsen, 2014).

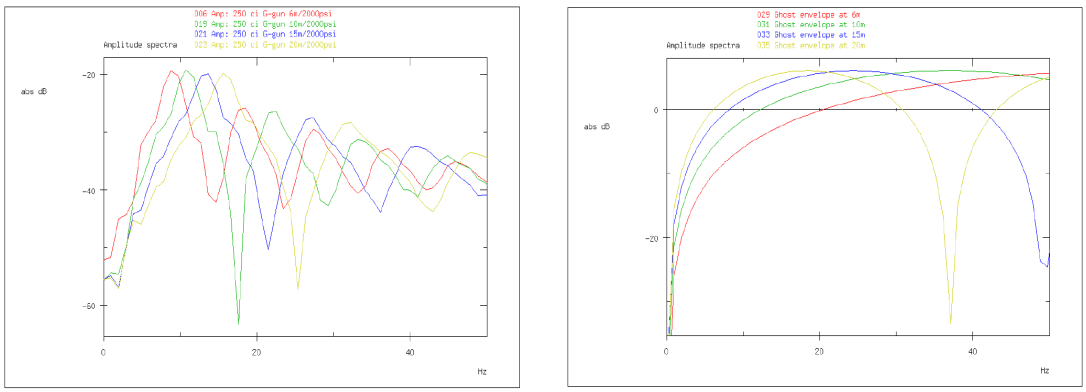

(a) *Fundamental frequency* **(b)** *Ghost attenuation*

Figure 4.1 – *(a) The fundamental frequency decided by the bubble time period is lowered for shallow sources. (b) The ghost attenuation is less when towing deep. Tow depths are 6 (red), 10 (green), 15 (blue) and 20 meters (yellow). Source: Parkes and Hegna (2011a).*

The interesting question is then which tow depth that is desirable for optimal low frequency output. Parkes and Hegna (2011b) found that the reduced ghost attenuation in the low frequency end with increasing depth is counteracted by the increase in fundamental frequency. This was further supported by Landrø and Amundsen (2014). They tested the outputs of sources at depths ranging from $3 - 40$ meters measured with a hydrophone 20 meters vertically below. The measured responses and their low-pass filtered correspondence are shown in **Fig. 4.2.** It can be noted from the figure that the bubble time period responded according to theory. In addition, the bubble pulse damping was significantly larger for the deep sources. The estimated amplitude spectra of the notional source signatures and the far-field amplitude spectra with the ghost added are shown in **Fig. 4.3**. This supports the statement that the two effects goes against each other. However, a logarithmic plot of the far field response with the ghost added using the 3 meter and 7,5 meter source reveals some differences. The shallow source seems to give 10 dB higher amplitude between 0.25 and 0.8 Hz while the deeper source gives 10 dB higher amplitude between 0.8 and 1.5 Hz. From $1.5 - 6$ Hz, they are approximately equal while the deeper source provide 10 dB better data in the $6 - 10$ Hz range. The plot is given in **Fig. 4.4.** The authors state that the simplicity of the test should be taken into account. Nevertheless, the differences indicate that the topic of array design to optimize for the low frequency content not yet is fully explored.

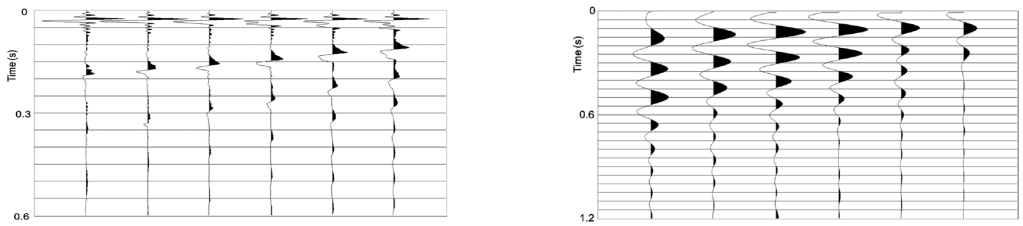

(a) *Full spectrum traces* **(b)** *Low-pass filtered traces*

Figure 4.2 – *Traces corresponding to 3, 5, 7.5, 10, 15 and 20 meters source depths. (a) The bubble time period decreases for the deep sources. (b) The filtered response shows strong attenuation of the bubble pulses with depth. Source: Landrø and Amundsen (2014).*

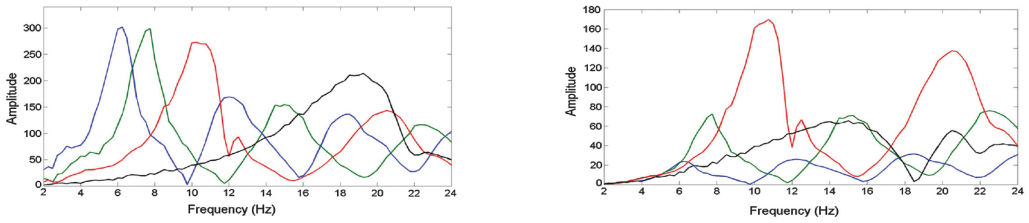

(a) *Without the source ghost* **(b)** *Source ghost added*

Figure 4.3 – *The source depths are 3 (blue), 7.5 (green), 15 (red), and 40 meters (black). (a) The 3 meters source depth gives lowest resonance frequency. However, (b) illustrates that the ghost attenuation severely reduces this benefit. Source: Landrø and Amundsen (2014).*

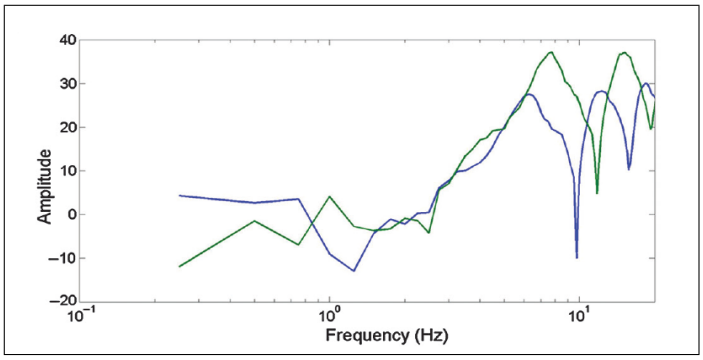

Figure 4.4 – *A logarithmic comparison plot with source depths of 3 meters (blue) and 7.5 meters (green) reveal that there are differences below 10 Hz with regards to where the amplitude spectrums are strongest. Source: Landrø and Amundsen (2014).*

The discussed limitations are hard to overcome. The one factor that might be adjusted is the design of the source array. Eq. 4.1 shows that the firing pressure and gun volume must be increased significantly in order to lower the fundamental frequency. In addition, the typical operating pressure is already close to maximum (Parkes and Hegna, 2011b). Attempts to preserve the energy of the bubble pulse has therefore been done by for instance tuning the bubbles. This will on the other hand affect the primary signal. Another method is described by Hopperstad et al. (2012). By frequency-locking all the sources to behave like one single big bubble in a configuration they call hypercluster, the low frequency output is extended in addition to preserving the middle and higher frequencies. In their research, they conclude that the output below the lowest fundamental bubble frequency is determined by the total bubble energy in the array, not how the air is distributed between the guns in the array. This is demonstrated in their tests where several pressure and volume configurations with the same total energy was used. Their result is shown in **Fig. 4.5** and indicates an equal response below the lowest fundamental frequency in the array, which was around 4 Hz.

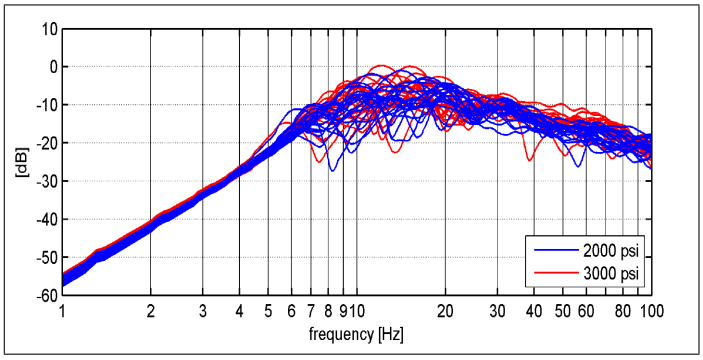

Figure 4.5 – *The total energy of an array is the deciding factor of the output below the fundamental frequency. A total energy of 380 kJ was used in all of the configurations. Above the fundamental frequency, the spectrums differ. Source: Hopperstad et al. (2012).*

4.2 Recording equipment

The dynamic environment of the marine seismic acquisition system allows noise to be generated and recorded by the receivers. All streamers will be subjected to noise and focus in streamer technology has therefore been important for high quality seismic imaging. The main transport mechanism of noise is the axial extensional wave. Whether the source is mechanically or flow generated, the fluid-filled streamer will experience low speed bulge wave effects. However, this can be handled by placing a number of hydrophones in groups or from exploiting the polarity difference, further explained in **Fig. 4.6.** A breakthrough in streamer technology occurred when Dowle (2006) presented the solid streamer. By replacing the buoyancy fluid with a buoyant flexible polymer, the axial extensional wave becomes compressional. The noise will then travel with higher velocity so that the array forming noise reduction principle is impractical. However, Dowle (2006) found that by closing the hydrophone element in a stiff package, the noise related stress and strain were significantly reduced, even for single hydrophones. In challenging weather, the solid streamer can be towed shallower than the fluid-filled with an acceptable noise level. The acquisition downtime will then decrease, which is of high economic value for the seismic companies. A field trial that aimed at comparing fluid-filled streamers and solid streamers was carried out in moderate seas in 2006. The results, shown in **Fig. 4.7**, indicate a noise level for the solid streamer of around 15 dB lower than for the fluid filled. For the low frequencies, this can be especially important. As discussed, the lowest frequencies are important for deep imaging. When travelling this long way, they also arrive with weak amplitudes. From Fig. 4.7, it can also be seen that the background noise level for the solid streamer is approximately 15 μbar. The deepest arrivals in the seismic data might be in the same order. The solid streamer can therefore have a very large impact on the S/N for low frequency recordings.

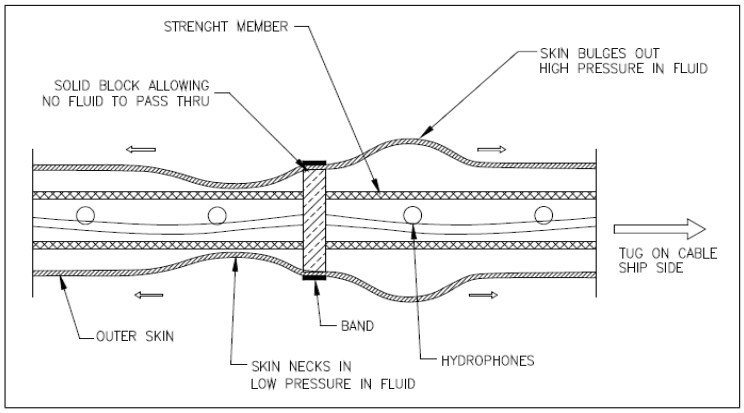

Figure 4.6 – *Bulge waves occur as low-pressure high-pressure waves, leading to bulges on the streamer. By accurately placing hydrophones together in a special arrangement, the polarity differences can be used for noise elimination. In solid streamers, the bulge waves are replaced by compressional waves. Source: Dowle (2006).*

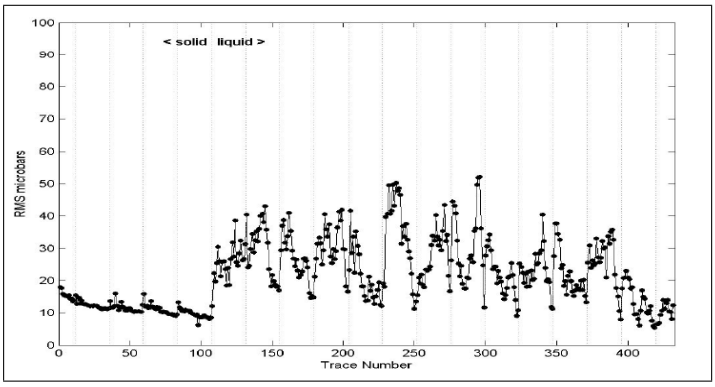

Figure 4.7 – *The solid streamer, plotted as the first 100 traces, clearly contains less background noise than the fluid filled streamer traces that follows. Source: Dowle (2006).*

Elboth et al. (2012) provides an interesting continuation in streamer development. Instead of focusing on the inner part of the streamer, they turned attention to the streamer surface. A specially designed coating material was applied on the streamer creating a hydrophobic surface. The idea is that this smoother surface will, to some extent, prevent turbulent flow around the streamer. Their result showed that a reduction in drag was experienced and the flow noise level below frequencies of 10 Hz was reduced by nearly 50%, shown in **Fig. 4.8**. However, the project was not continued due to difficulties in keeping the coating material attached to the streamer. This could be because of organic activity affecting the coating. This theory was strengthened by the fast degradation that occurred when they tested it in warmer water[1]. It is still interesting that their result showed improvement for the lowest frequencies, indicating that progress might be made in the future with regards to such surfaces.

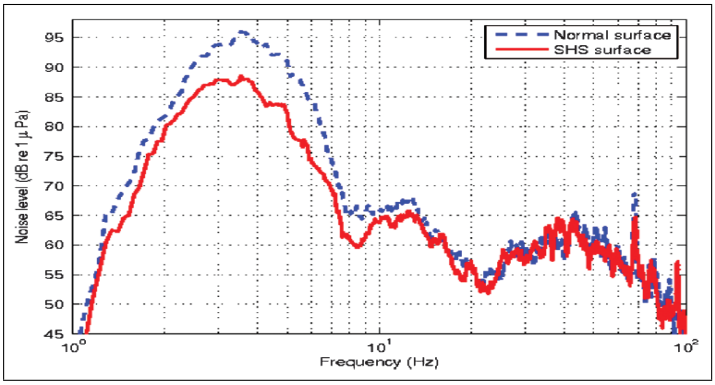

Figure 4.8 – *The superhydrophobic streamer gives a lower noise level below 10 Hz which can be seen as the red graph. The blue dashed line represent the normal surface noise level. Source: Elboth et al. (2012).*

[1]Conversation with Thomas Elboth, May 2014.

Chapter 5

Low frequency processing

As discussed in previous chapters, the recent advancements in the seismic industry has led to acquisition of data that contains a broader range of frequencies. Processing of such data introduces challenges in how to preserve the additional frequencies in both the low and high end. As operators and modules in seismic processing generally are applied on full bandwidth data and designed for the conventional frequency range, the isolated low frequency response in broadband data processing is not well known. This chapter presents the core of the thesis and contains a description of the dataset, methods and parameters tested, results and observations made in how the lowest frequencies react to different processes. The primary goal was to identify possible problems and compare processing methods and parameters to conclude with an optimized processing flow that favours the lowest frequencies. Already existing full bandwidth processed data was filtered for a direct comparison throughout the different processing stages.

5.1 Dataset description

The Sleipner area in the North Sea was discovered in 1974. A more detailed location is provided in **Fig. 5.1**. Today, the area consists of several gas and condensate fields and the production from these makes up approximately 10 % of Statoil's total income each year. In addition, CO_2 is separated from the produced gas and injected into the porous and permeable Utsira formation. This was Statoil's first major CO_2 storage project and is still operational. The total injected gas during the project lifetime constitute of twice the amount the Norwegian car park releases each year (Statoil, 2014). The Sleipner area is therefore well suited for 4D seismic projects, which can help monitoring the gas development. The seismic survey used in this thesis is the ST12018 Sleipner CO2 4D survey. It was acquired from 15 December 2012 to 20 January 2013 with the Oceanic Challenger vessel (CGG, 2014a). Three different datasets were gathered, one conventional survey and two BroadSeis surveys. The project was executed for both Statoil and

the CGG Research and Development (R&D) team with the purpose of providing Statoil with reliable 4D data in addition to test 4D BroadSeis responses for CGG. The research performed in this thesis has been done using one of these BroadSeis surveys. The most important survey details with relation to the testing are given in **Table 5.1**. Some of these parameters are also sketched in **Fig. 5.2**. The relevant source information, such as set up, far field signature and amplitude spectrum, is provided in **Fig. 5.3**.

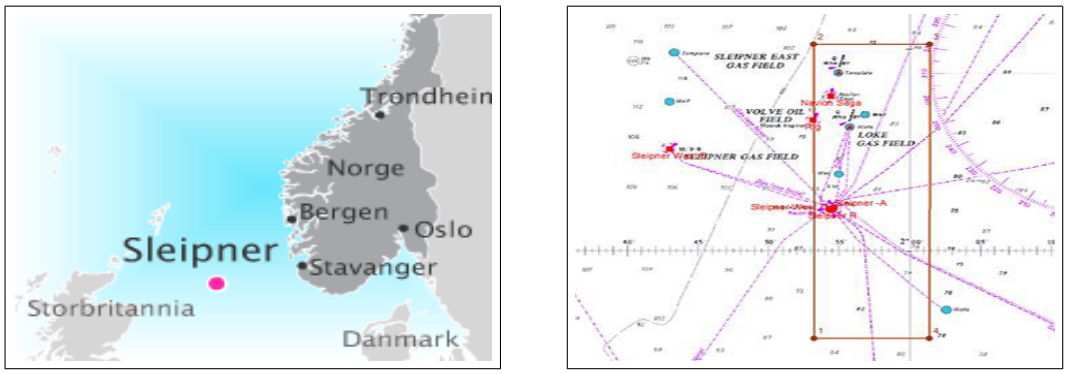

(a) *Location of Sleipner* **(b)** *Survey area*

Figure 5.1 – *(a) The Sleipner area can be found in the southern North Sea west of Stavanger, Norway. Source: Statoil (2014). (b) The survey, represented by the light brown square, is located in an area with several installations close by. Source: CGG acquisition report.*

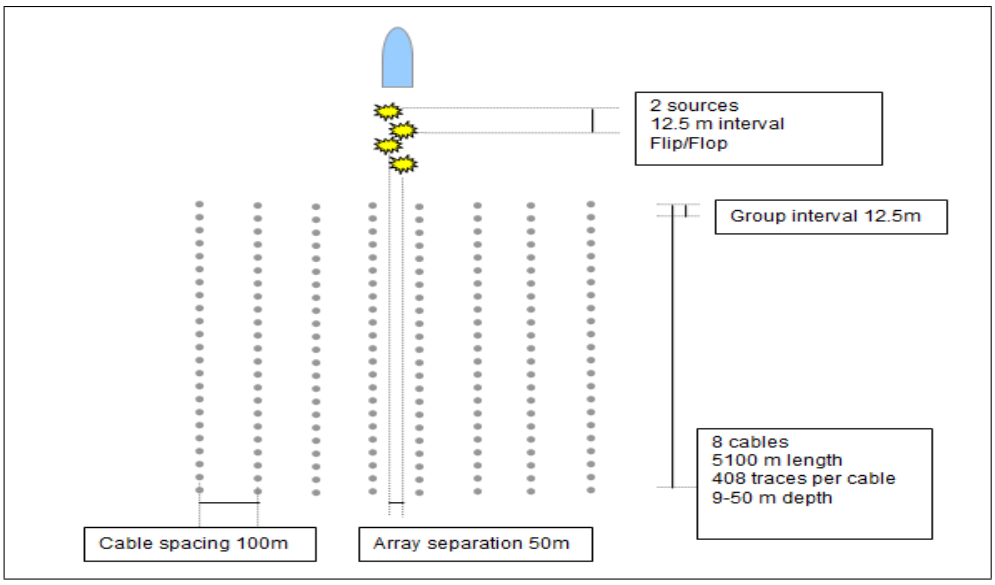

Figure 5.2 – *An acquisition sketch showing some of the main survey parameters. Note that the streamer depth varies according to the BroadSeis profile (not seen in the illustration).*

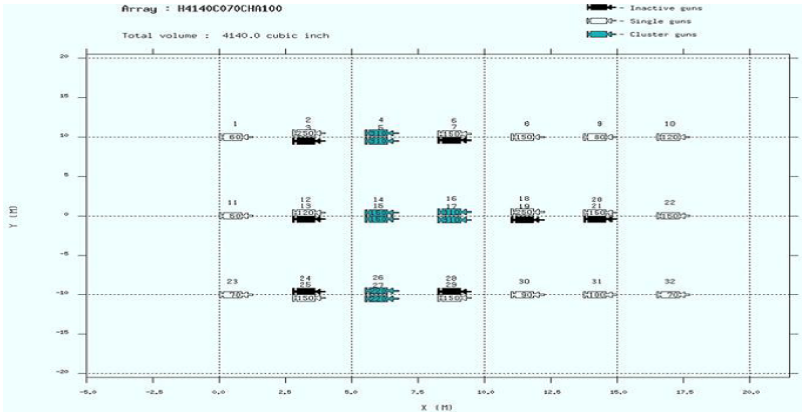

(a) *Array configuration*

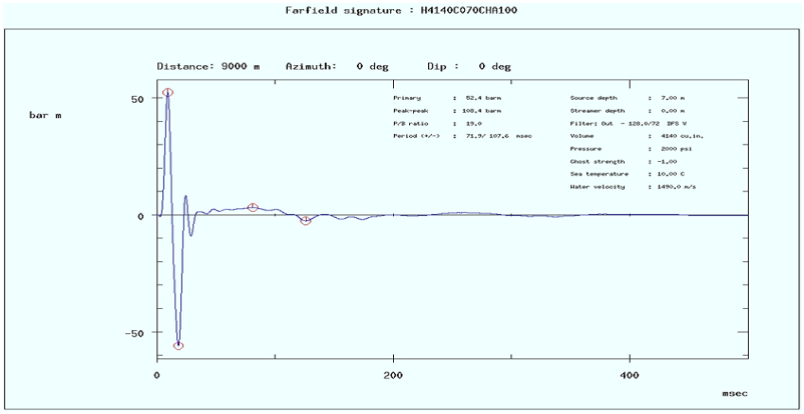

(b) *Far field signature*

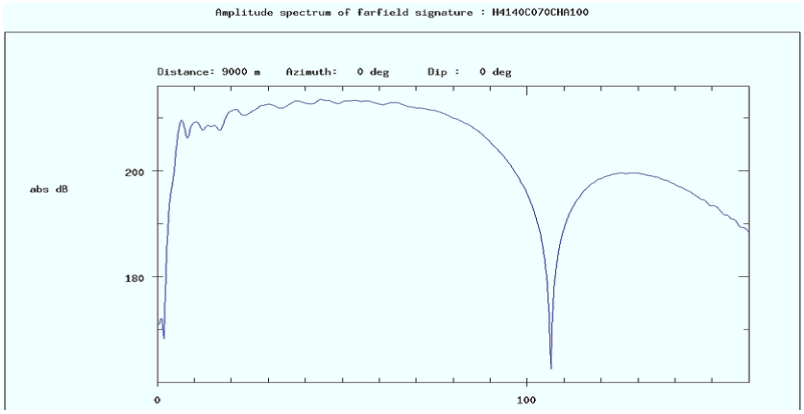

(c) *Source output spectrum*

Figure 5.3 – *Source characteristics relevant for the processing. (a) Air gun distribution in the source array. Black colour represents inactive guns, white represents single guns and green represents cluster guns. (b) The far field signature of the source output. Note the red circles used for calculating P and P/B. (c) The frequency range emitted by the source. Note the notch at around 107 Hz corresponding to the source depth of seven meters. Source: CGG acquisition report.*

Survey definition	
Contractor / Client	CGG / Statoil
Survey name	ST12018 Sleipner CO_2 4D
Survey location	Norway / North Sea
Latitude / Longitude	58°23'06.00"N / 001°57'38.00"E
Number of CMP full fold	3590 CMP km
Line orientation	0.85°/ 180.85°
Number of lines	11
Water depths	81 - 85 m
Water temperature	10°C
Streamer parameters	
Number of streamers	8
Streamer active length	5100 m
Streamer type	Sentinel Solid Seal
Streamer separation	100 m
Number of groups per streamer	408
Group length	12.5 m
Streamer depth	$9 - 50$ m
Offset seismic required	85 m
Receiver parameters	
Record system	Sercel Seal
Record length	4750 ms
Sampling rate	2 ms
Digital low-cut filter	None
High-cut filter	200 Hz
Source parameters	
Source type	G-Gun II
Number of sources	2 x 3 Gun Strings
Source array depth	7.0 ± 0.5 m
Source length	16.50 meters
Nominal air pressure	2000 psi
Volume	2 x 4140 cu.in
Shot point interval	12.5 m
Source centre separation	50 ± 6.25 m
Sub-array separation	10 m
Number of sub-arrays per source	3
Minimum time between shots	7.05 sec
Guns timing	± 1.5 ms
Shooting mode	Flip/Flop
P	108.4
P/B	19

Table 5.1 – *Main information about the survey with regards to survey definition, streamer, receiver and source details.*

Other operational factors such as weather conditions, currents, tides, fishing, shipping activity and vessel speed were reported normal. Common quality control was performed on board the vessel during the acquisition to ensure good S/N. The water depth is almost constant, only varying between 81 to 85 meters, which means that the energy is expected to be distributed consistently throughout the covered area. The accuracy of water bottom multiple modelling should therefore benefit. The geology in the area is not specifically challenging. The reflecting boundaries are almost completely flat from top to bottom. Velocity models exist due to the mature area and the number of seismic surveys that has been acquired here before. The general data quality of the relevant BroadSeis survey is therefore expected to be very high. This makes the survey ideal to be used in a low frequency processing project. High S/N helps demonstrate the isolated low frequency response clearer as unwanted contaminating artefacts to some extent can be avoided. The far field signature and the frequency spectrum, given in Fig. 5.3, will ideally be used in the processing for deghosting/shaping and as a quality control of the frequency range, respectively.

Of special interest in the data is an event occurring at around 2300 ms. This event represents the transition from the Paleogene to the Cretaceous geologic time period. In lithological terms from the southern North Sea, the boundary is defined as the transition from the soft marine shales in the Rogaland Group to the hard limestones in the Shetland Group. During late cretaceous period, the sediment influx into the southern North Sea was very limited. These limestones are therefore almost pure chalk. When chalk deposits are buried below 2000 meters, the increased temperature and pressure might induce a metamorphic process transforming the chalk to a very hard rock called chert (Ramberg et al., 2007). Well 15/9-1 is located close to the survey area and will be used as a representative well. Here, the top Shetland Group can be found at 2743 meter overlain by formations from the Rogaland Group (Norwegian Petroleum Directorate, 2014). Nevertheless, if the chalk in the Sleipner area has been transformed to chert or if it is common chalk, the product of density and velocity is still much higher than in the above sediments. This produces a powerful positive event that easily can be recognized. This event has proved to be very valuable in the project. It has continuously been used throughout the processing steps as its strong response clearly demonstrates how the modules works and if there are problems related to for instance the low frequency response. The event will simply be referred to as "the chalk" in the following discussion of each processing step. A stratigraphic column showing the transition boundary is included in **Fig. 5.4**. A younger formation important for the area does also deserves a few words. Although not directly related to the processing, it represents one of the main reasons for the acquisition of the survey. The Utsira Formation can be found at 824 meters in well 15/9-1 and was deposited as a shallow marine sandstone during the Neogene period. Such sandstones often have high porosity and permeability and are ideal as reservoirs. In the North Sea, the Utsira Formation does not contain hydrocarbons, but is used as a source of injection water. As in the Sleipner example, it is also used for CO_2 storage. A detailed geologic description is beyond the scope of this project, but such information can be found in for instance Isaksen et al. (2002) and references therin.

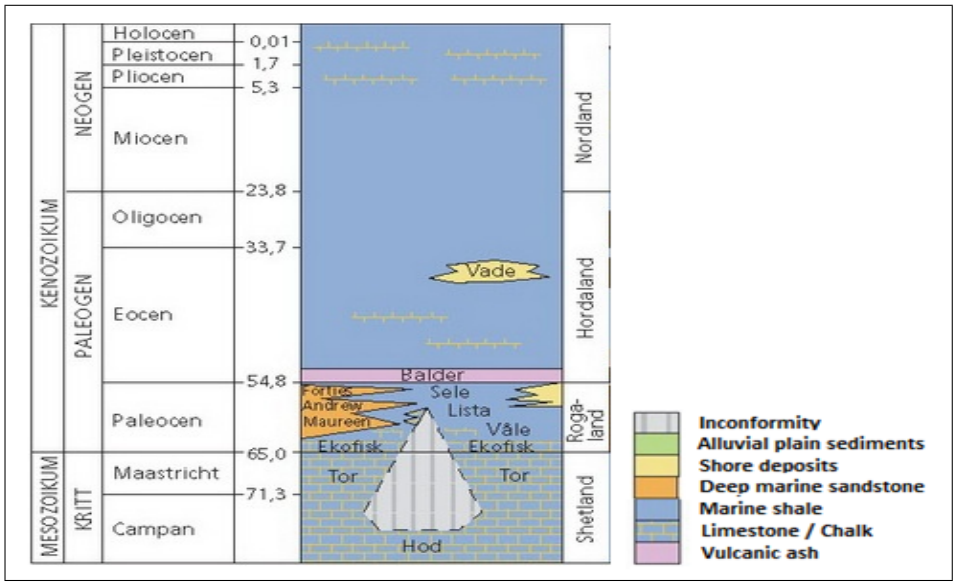

Figure 5.4 – *The transition from the Rogaland Gp. to the Shetland Gp. in the Sleipner area is characterized as an impedance increase due to the soft nature of the Maureen Fm. and Våle Fm. and the hard nature of the Ekofisk Fm. and Tor Fm. laying below. Although this illustration represents the southern North Sea in general, well data from Sleipner confirms that this is valid. Source: Ramberg et al. (2007).*

5.2 Processing sequence

In this project, the full bandwidth processing flow that was used in 2012/2013 when CGG first processed the ST12018 Sleipner CO2 4D survey will be used as the shallow water reference flow. Although the majority of these steps have been applied to the low frequency dataset, some steps were found to need further detailed testing. They were selected according to general importance, the uncertainty related to how the specific step affected the low frequency response and what the full bandwidth filtering showed. The full reference sequence and the applied steps are listed in **Table 5.2.** In the following sections, the processing results will be given and explained. Each step will be divided in four parts. The first part consists of a description of the step purpose and which method that was used. For steps that have been analysed in detail, a deeper understanding of the method will be presented. The second part is where the results are displayed. An endless number of test results could have been included, but unless explaining an important phenomenon, only the result used for the continuation is given. The third part will be a statement of the main observations while the last part consists of an evaluation and a recommendation in how to proceed. The produced work was carried out using CGG developed softwares. The processing was done using Geovation 1, while wavelet models were built in MatCalc. The seismic sections and belonging attributes were extracted from the visualization tools Expose and Tornado.

Main sequence	Full sequence	Tested steps
Pre-processing	1. Raw data	Ok
	2. Low-cut filter	Ok
	3. Swell noise removal	Ok
Linear denoise	4. Linear noise attenuation	Tested
	5. K-filtering and trace dropping	Ok
Deghosting	6. Zero phase designature	Tested
	7. Debubble with source deghosting	Tested
	8. Receiver deghosting	Tested
Demultiple	9. Multiple modelling	Tested
	10. Multiple subtraction	Tested
Corrections	11. Receiver motion correction	Ok
	12. Phase only Q compensation	Ok
	13. Amplitude and tidal corrections	Ok
Interpolation	14. Binning	Ok
	15. 3D regularization	Tested
	16. Residual noise attenuation	Not applied
Imaging	17. PSTM preparation	Ok
	18. Common offset denoise	Not applied
	19. PSTM	Ok
	20. Radon demultiple	Not applied
	21. Mute and stack	Ok

Table 5.2 – *Full reference sequence where the applied steps are denoted "ok" and the steps that needed a more comprehensive testing are denoted as "tested". The steps denoted "not applied" were included in the reference flow, but not in the low frequency sequence.*

5.2.1 Pre-processing

Before focusing only on the low frequencies, preparation of the raw data in the same way as for the full bandwidth processing was done. The raw data is shown in **Fig. 5.5.** By applying a low-cut filter of 2.5 Hz, the majority of the hydrostatic pressure noise is removed. This can be seen in **Fig. 5.6.** The next module applied was for detection of traces with unusual high energy, often occurring because of crossflows. If such traces were detected, their amplitude values were replaced by zeroes and then interpolated from nearby traces. The detection is done by calculating the ratio of the trace energy and average assumed energy. If this value is bigger than a decided number, the trace is considered contaminated. The result after this process can be seen in **Fig. 5.7** and can further be regarded as the starting input to the low frequency processing. A spectrum comparison of the raw data, data after low-cut filter and data after both low-cut filter and bad trace removal is included in **Fig. 5.8.** Unless stated otherwise, the presented shot gathers will be given from 0 to 4500 ms with full offset displayed.

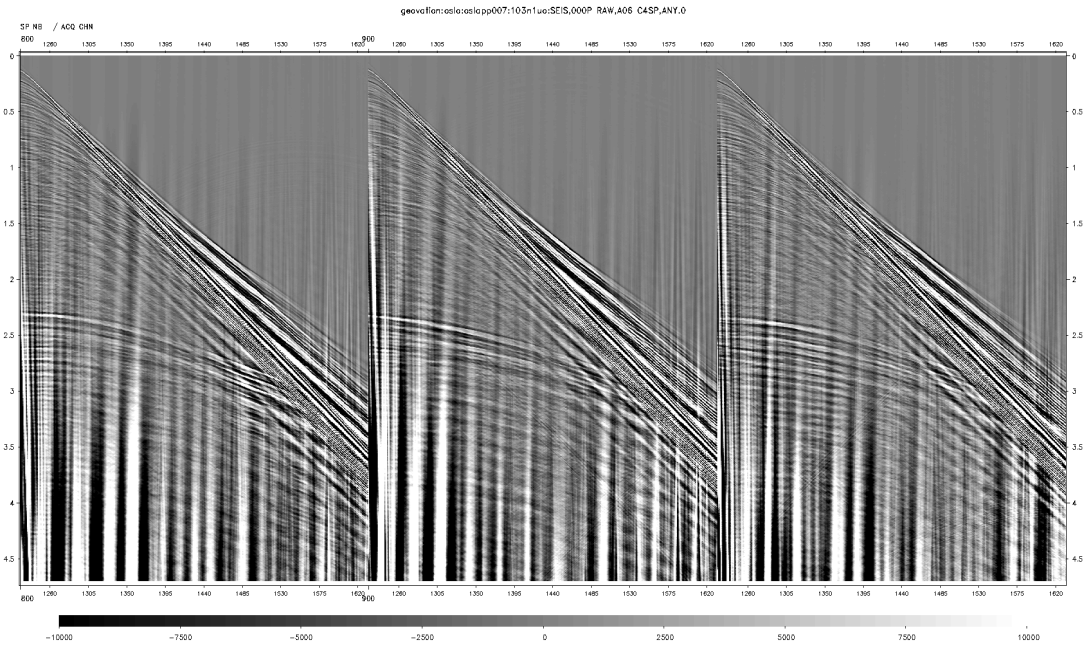

Figure 5.5 – *Raw data.*

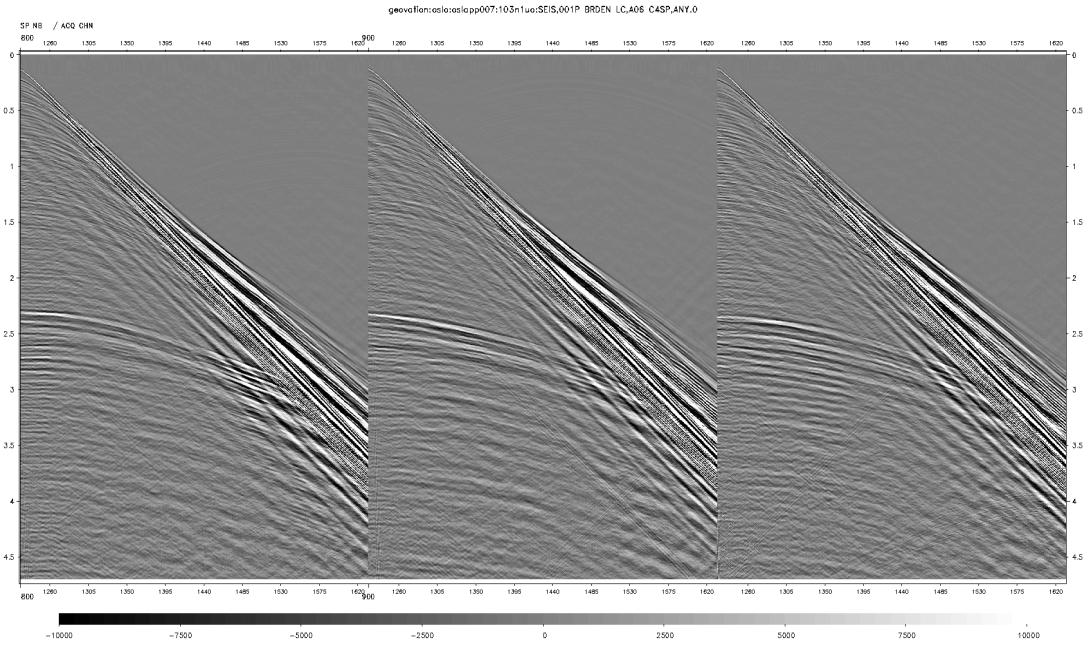

Figure 5.6 – *2.5 Hz low-cut filtered data.*

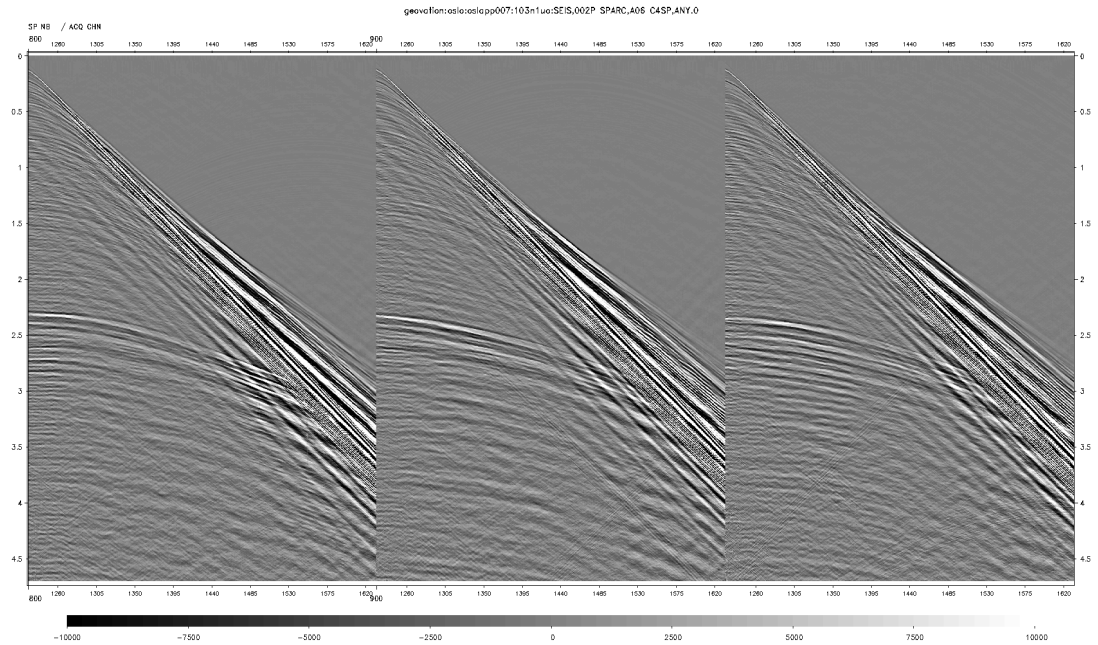

Figure 5.7 – *Bad trace removal applied.*

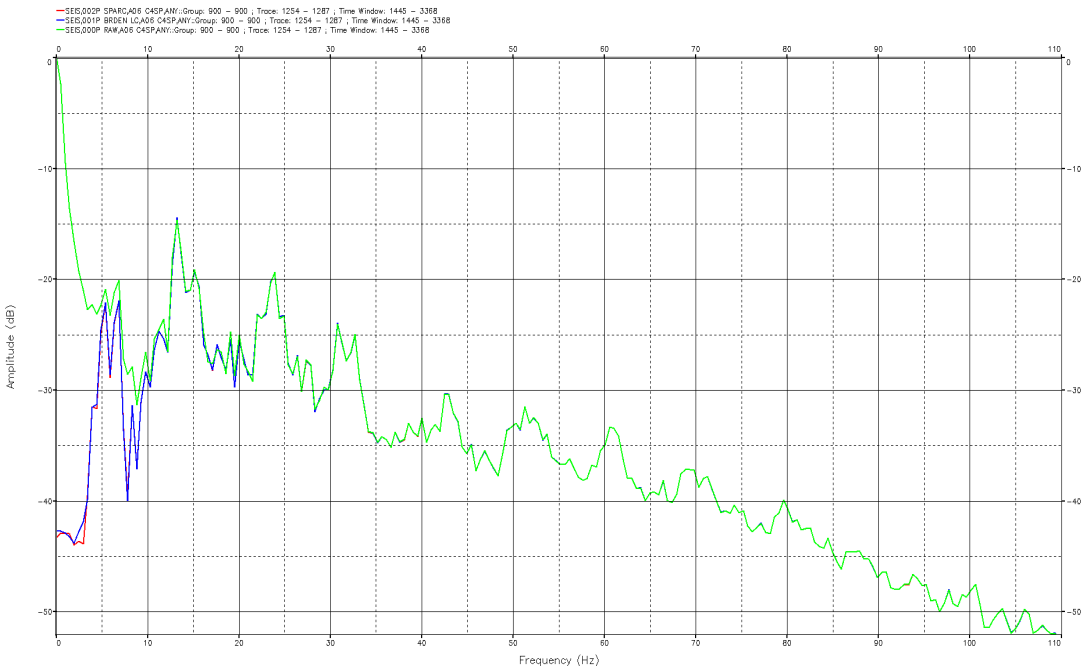

Figure 5.8 – *Raw data (green), low-cut filter (blue) and bad trace removal (red).*

5.2.2 High-cut filtering

The next step was to decide the ideal frequency range for the testing. It was important to set the high-cut value as low as possible to observe the response of the lowest frequencies, but high enough to still distinguish between the main events. The frequency with a wavelength equal to the multiple period will be referred to as the "multiple tuning frequency" in the following sections. In this data, the multiple period is approximately 100 ms, hence the multiple tuning frequency was expected to be around 10 Hz.

Method

The filtering process used is time-invariant. The operator requires input of an operator length, high-cut frequency and cut-off frequency. The operator length is the length of the impulse response of the convolution operator. The high-cut frequency is the value where attenuation of higher frequencies begin, while the cut-off frequency is the higher frequency limit of where signals shall pass through. The interval between the cut-off frequency and the high-cut frequency will be referred to as the slope. From the above definitions, it is clear that the slope defines how fast the attenuation will be applied from the high-cut frequency. Very steep slopes might introduce edge phenomenons, while a very slack slope is undesirable as we want to limit the spectrum to observe the selected low frequencies only. A summary of the elements in the process is listed in **Table 5.3.**

Parameters tested	**Description**
High-cut frequency	The upper value of where signal pass unaffected through
Cut-off frequency	The upper value of where signal is allowed to pass through
Slope	Difference between cut-off and high-cut. The zone of where attenuation begins and ends
Operator length	Length of the impulse response of the convolution operator

Table 5.3 – *Tested high-cut filter parameters.*

Results

Test of operator lengths revealed no specific effect on the data. The target was then to find the optimal frequency range to work with. Several combinations of high-cuts, cut-offs and slopes were tested and the main selected combinations can be seen in **Fig. 5.9**, **Fig. 5.10** and **Fig. 5.11.** Their spectrums are compared in **Fig. 5.12**, which reveals good similarities where frequencies are overlapping.

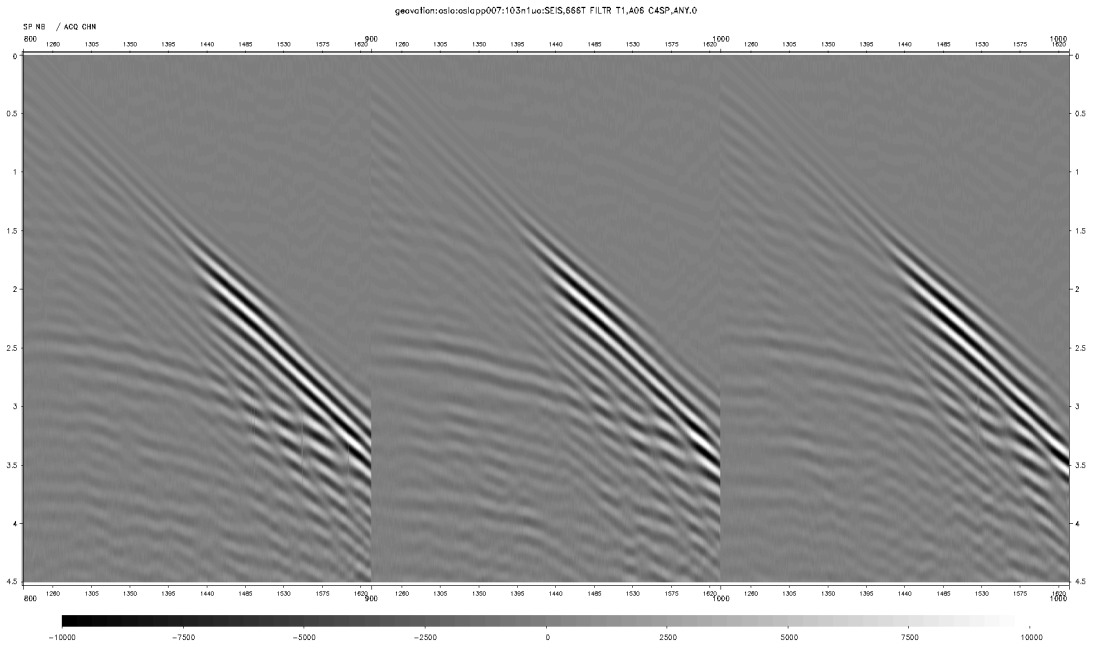

Figure 5.9 – *5 Hz high-cut data with 10 Hz cut-off.*

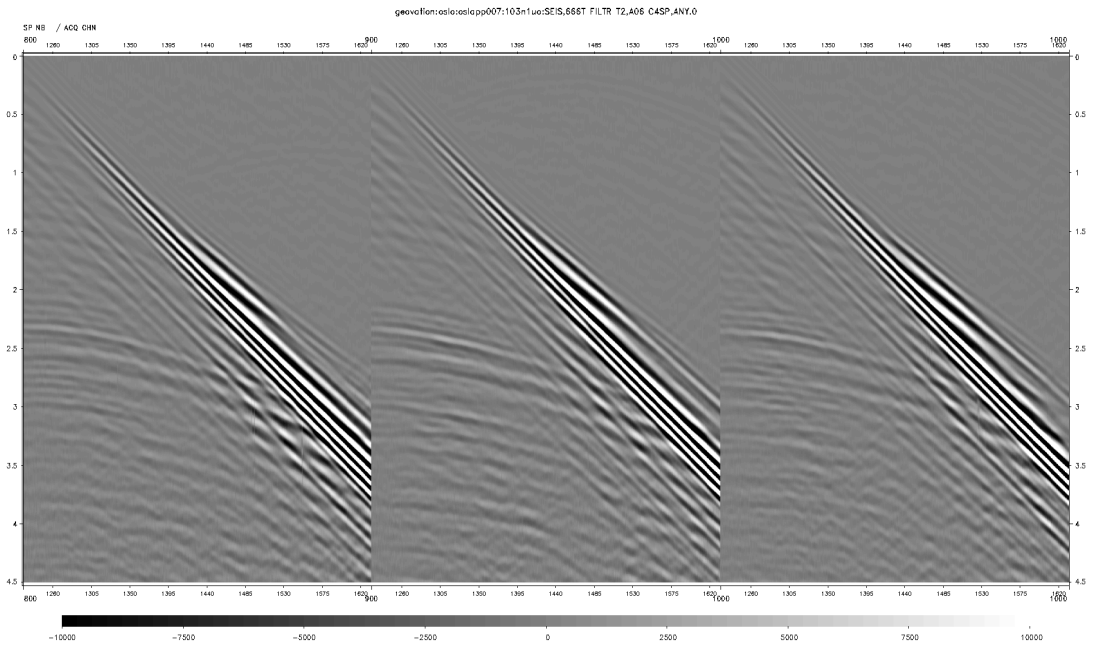

Figure 5.10 – *10 Hz high-cut data with 15 Hz cut-off (D1).*

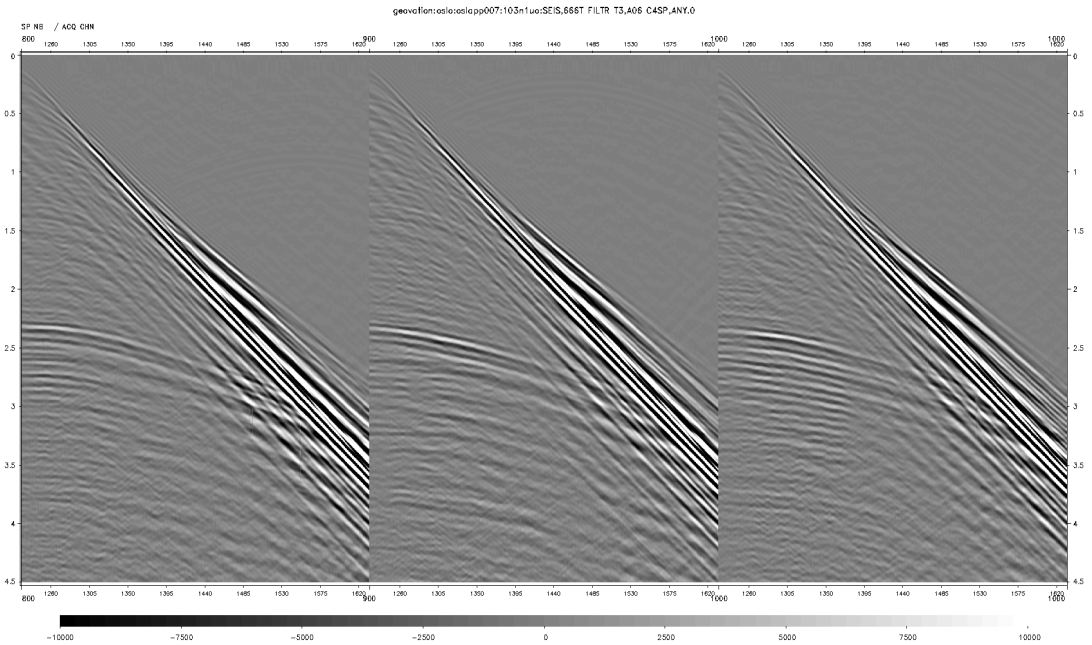

Figure 5.11 – *20 Hz high-cut data with 25 Hz cut-off (D2).*

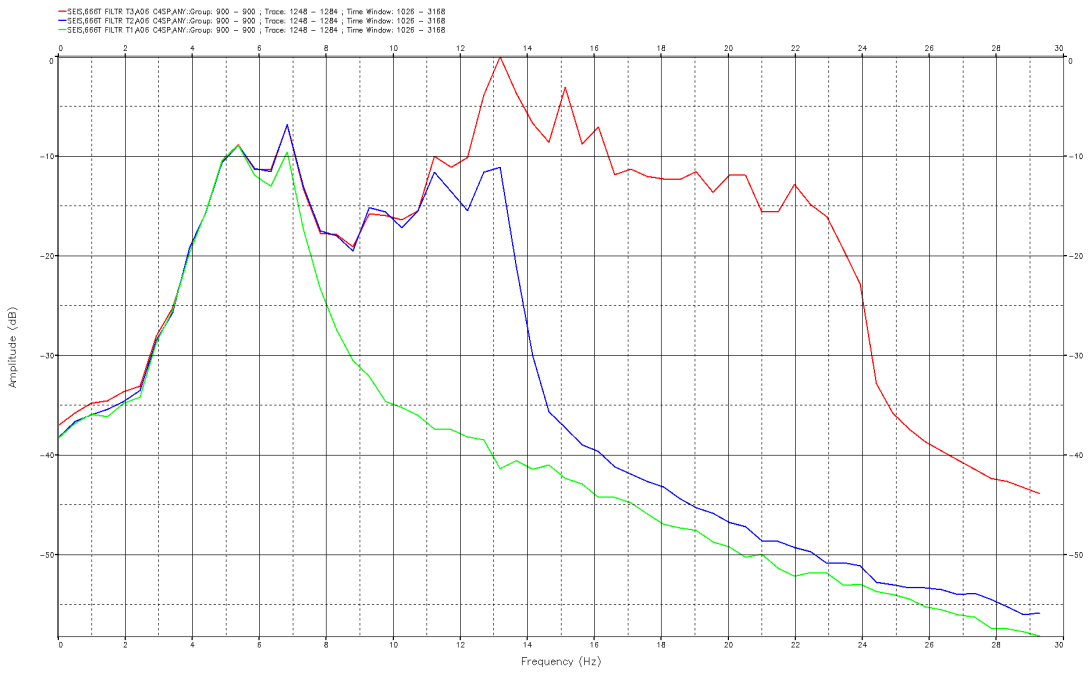

Figure 5.12 – *Spectrum for high-cut data of 5 Hz (green), 10 Hz (blue) and 20 Hz (red) with 5 Hz slopes.*

Observations

- A slope steeper than 5 Hz was found to introduce ringing.
- The operator length was not found to affect the low frequencies in the filtering.

Evaluation and continuation

As can be seen in Fig. 5.9, the events are very hard to separate. This was expected since the high-cut is below the multiple tuning frequency. In Fig. 5.10, the events are clearer, but only the chalk can be observed with a good level of confidence. A high-cut of less than 10 Hz was therefore decided too low for reliable results in further processing. Fig. 5.11 represents the 20 Hz high-cut data and can be used to quality control the lower high-cut data by filtering down to the same frequency range. This dataset was not found to differ much from the full bandwidth data when full bandwidth data was filtered with a 20 Hz high-cut. The continuation will involve the following datasets:

- 10 Hz high-cut with 15 Hz cut-off. This dataset will be processed and is denoted dataset 1 (D1).
- 20 Hz high-cut with 25 Hz cut-off. This dataset will be processed and is denoted dataset 2 (D2).
- Already existing full bandwidth processed data. This dataset will be used for comparison through low-pass filtering and is denoted full bandwidth dataset (FBD).

5.2.3 Linear denoise

The target of this step was to attenuate noise in the water layer. In addition, a K-filter was applied as in the FBD processing. In both D1 and D2, aliasing should not be a problem because of the low frequency content only.

Method

The operation aims at removing linear noise based on a user-defined model. It creates a model of the linear noise that is removed from the data to be processed. It operates with shot gathers as input and transforms the data to the τ-p domain where the linear events will plot as points defined by the slope and interception in the t-x domain. Parabolic events will separate from linear events in the τ-p domain. The idea is then that certain combinations of τ and p, that represents the noise, can be removed before a transform back to the original domain is performed. The values to be removed are decided by the user and the method can be executed on desirable locations in the data. Here, the defined model attenuates linear events of approximately 1500 m/s, corresponding to the

water velocity. The adjustable parameters in this process are mainly the parameters defining the cone size that removes data and the sliding windows. In addition, frequency bands or time intervals can be isolated for milder, harder or no attenuation. The module was run in both the shot and receiver domain to attack as much of the linear noise as possible. The method is expressed graphically in **Fig. 5.13**, while parameters tested and their sensitivities can be seen in **Table 5.4**. The K-filter was also tested to eliminate the possibility of unforeseen problems.

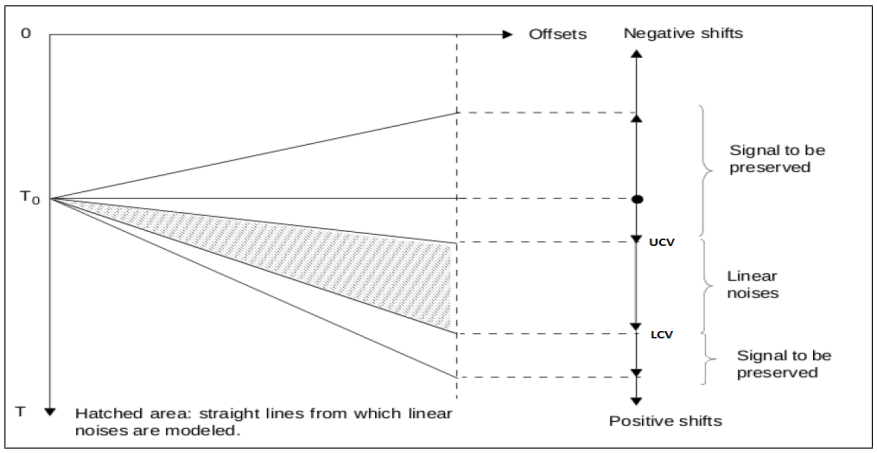

Figure 5.13 – *The algorithm removes linear events in the hatched area (cut-window) after a Radon transform. The cut-window is defined by an upper cut value (UCV) and a lower cut value (LCV) that can be adjusted. The hatched area can be slided through the data using different windows and operator lengths. Source: Modified from CGG documentation.*

Parameters tested	**Description**	**Sensitivity**
Cut window	The lines situated between an upper and lower limit are used to build the linear noise model	Very sensitive
Frequency range	The frequencies used in the operation can be decided as an interval	Not sensitive
Time window	Total time window used in the process defined by a lower and upper time	Not sensitive
Temporal sliding window	Length of the temporal elementary processing block and overlap between two successive blocks	Sensitive
Spatial sliding window	Length of the spatial sliding window and overlap in number of traces	Sensitive
Weighting	Frequency bands can be weighted differently	Not sensitive

Table 5.4 – *Tested parameters in the linear denoise algorithm.*

Results

The sensitive parameters were further tested and modifications done to the full bandwidth processing values. The cut window could be increased, especially on the LCV side. Both the temporal and spatial sliding window were also increased to approximately double value. D1 denoised data with the FBD parameters are shown in **Fig. 5.14** and D1 denoised data with the modified parameters are included in **Fig. 5.15.**

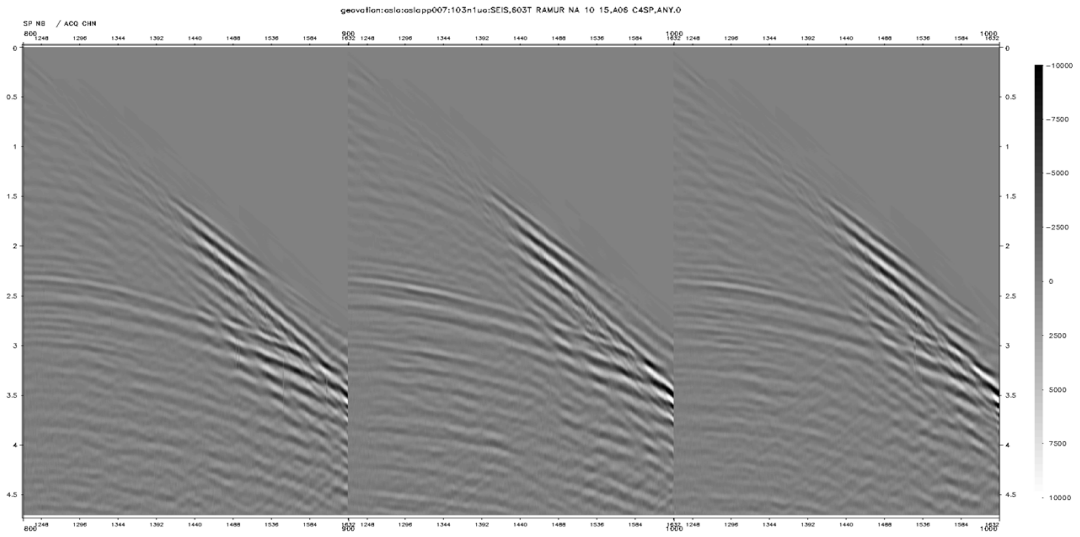

Figure 5.14 – *D1: Denoise using FBD parameters.*

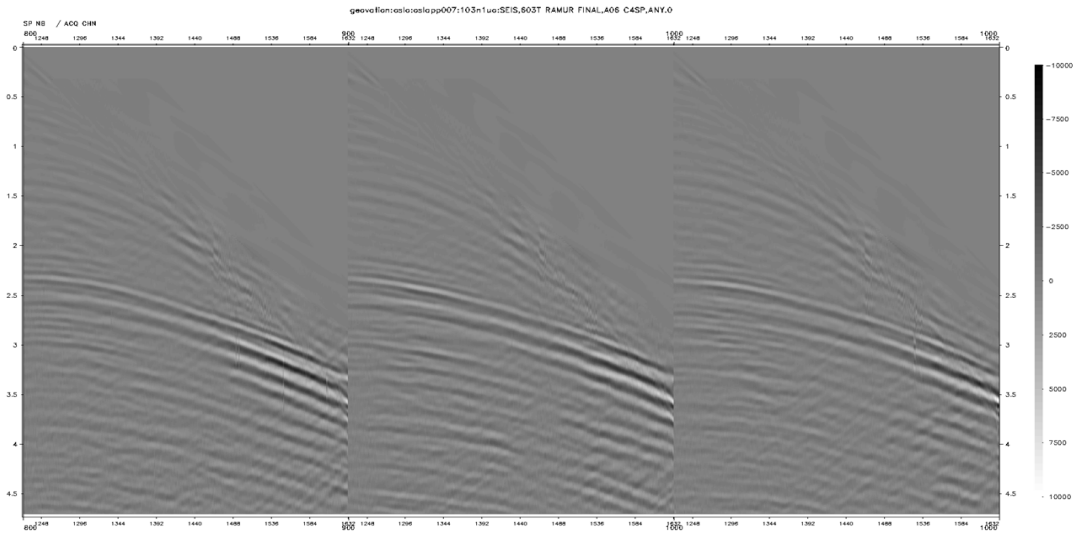

Figure 5.15 – *D1: Denoise using modified parameters. Note the better continuity, especially around the chalk at far offsets.*

To control that the modified denoise process not harmed the primaries, a difference plot between the input and the output was made. This difference shows the data removed. As can be seen in **Fig. 5.16**, the majority is of a linear character. The same modified parameters were also applied to the FBD and the difference between this input and output was obtained. The result is shown in **Fig. 5.17** where events crossing the linear trend may be observed. This means that primaries were removed and the modifications too strong for the full bandwidth.

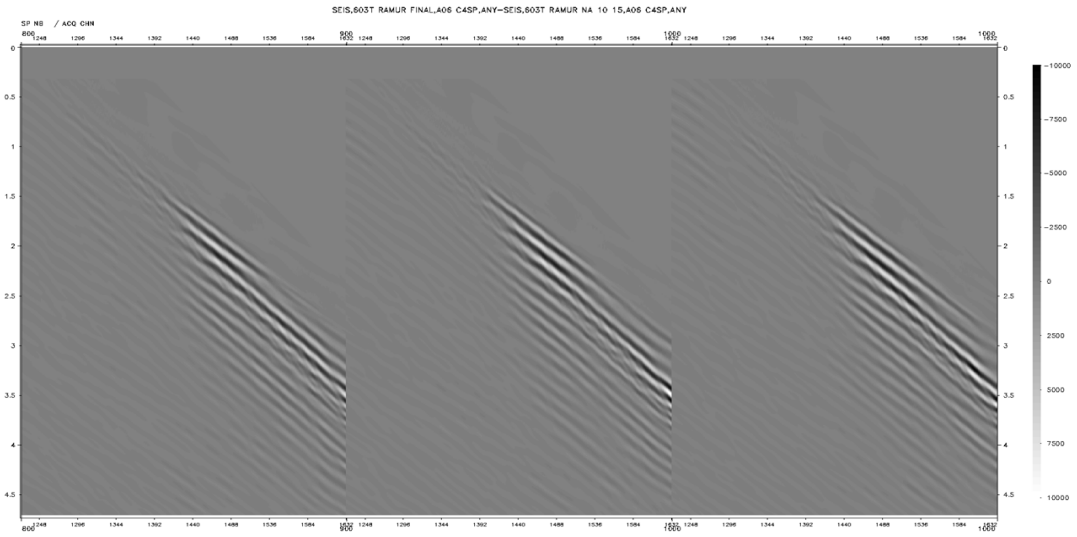

Figure 5.16 – *D1: Difference section with modified parameters.*

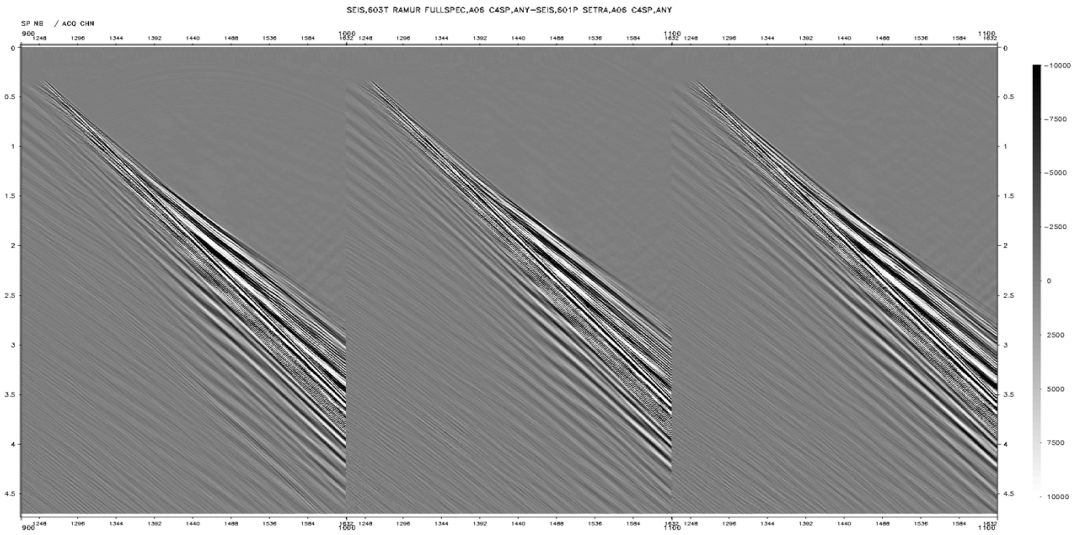

Figure 5.17 – *FBD: Difference with modified parameters. Some vague crossings may be observed, especially at the shallow sections.*

Since the seabed response only can be found in a limited offset interval, due to the minimum offset required and the critical angle, the denoise algorithm might see the seabed as a linear event with a velocity of around 1500 m/s. The common approach is therefore to cut the seabed area from the input and paste it onto the output after linear noise attenuation has been executed. However, an important observation was made with regards to the low frequency seabed response. Apparently, the shallow water makes the direct wave and the seabed arrival tune together, creating an unrealistic seabed representation. In many processing operations, the seabed wavelet is an important input so this needed to be explored better. The problem is explained in **Fig. 5.18**, while **Fig. 5.19** presents a possible better solution where the linear denoise method has been applied all the way up to the seabed with parameters tested for the seabed only. It turned out that larger sliding windows and a larger cut area were optimal for this as well.

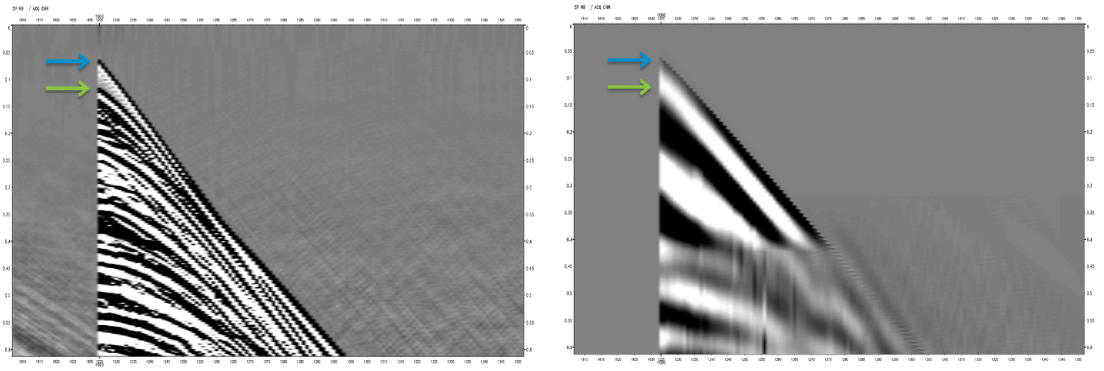

(a) *Full bandwidth data* **(b)** *D1 data*

Figure 5.18 – *The first event on (a) marked by a blue arrow is the direct wave and the second event marked by a green arrow is the seabed response. In full bandwidth data, they can easily by separated. (b) In the low frequency case, tuning of the two results in an unrealistic seabed representation. The first 600 ms are displayed with an equal gain for the two pictures.*

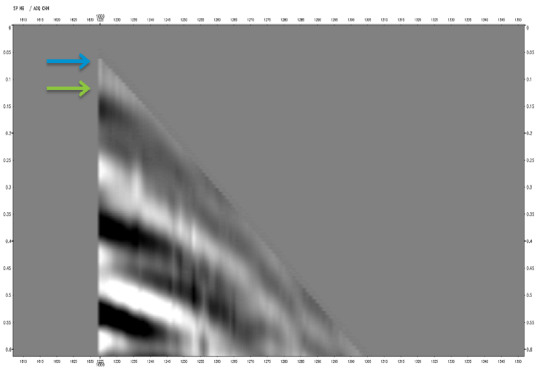

Figure 5.19 – *D1: Denoise performed up past the seabed. The green arrow shows that small parts of the seabed might be revealed behind the tuning when denoise is applied instead of the cut and paste method. The first 600 ms are displayed.*

A K-filter was also applied and the difference between the energy before and after can be seen in **Fig. 5.20.** No differences could be observed on the shot gathers.

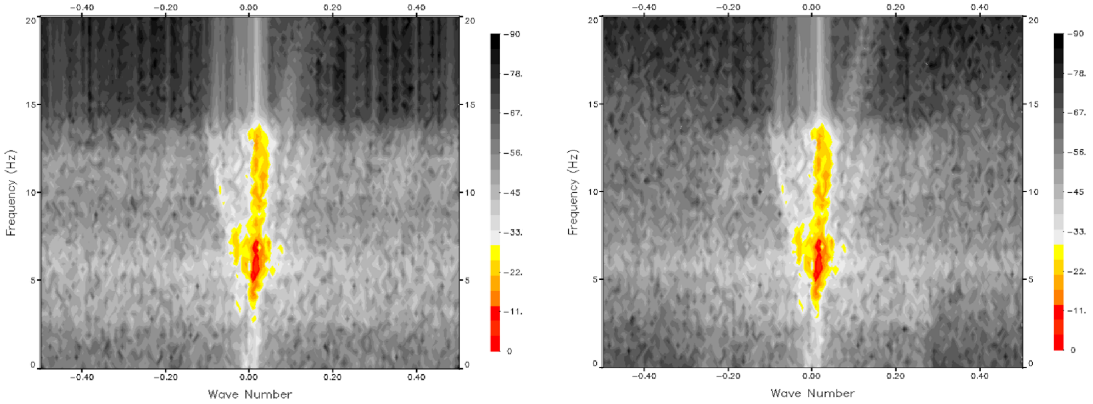

(a) *D1: Before K-filtering* **(b)** *D1: After K-filtering*

Figure 5.20 – *The energy distribution before (a) and after (b) K-filtering is as good as identical. The K-values removed can slightly be seen as a cut around -0.25 and 0.25.*

Observations

- The cut area can be increased without loss of primaries compared to full bandwidth processing.
- An increase in both the temporal and spatial sliding window creates visually clearer and more continuous events.
- Special care is needed when handling the seabed because of tuning with the direct wave. Linear noise attenuation may be applied over the seabed.
- K-filtering is not necessary, but do no harm to the low frequencies.

Evaluation and continuation

The possibility of removing more noise from the data at an early stage is a valuable observation. Less noise reduces artefacts introduced from other modules and enable better visualization of the lowest frequencies. Since the seabed response is contaminated by the direct wave for the low frequencies, it can be recommended to split the linear noise attenuation in two frequency bands. The lower band can manage a tougher cut and should go up past the seabed. The increase in the sliding window size might have to do with the longer wavelength corresponding to low frequencies. Because of the problematic seabed reflection, processes needing a seabed input wavelet, such as surface related multiple elimination (SRME) might struggle. The modified linear noise attenuation parameters will be used in both D1 and D2 in the processing continuation.

5.2.4 Deghosting

The deghosting step was divided in two parts where the first constitutes of zero-phasing of the wavelet, attenuation of bubble effects and removal of the source ghosts. The second part was reserved for removal of the receiver ghosts.

Method

The first module applied produces a zero-phased wavelet with a flat spectrum. It shapes the wavelet such that the source ghost and the receiver ghost of the source ghost are included in the signature. The module reads the input signature and computes a designature filter that is applied to the traces (1D) in the input data. It also applies a gain to the spectrum that can be weighted differently for defined frequency bands. Ideally, a directional designature operator derived from the near-field hydrophones is desirable to improve the resolution and preserve AVO (Poole et al., 2013). However, the signature provided from the acquisition proved to be inaccurate. A synthetic input signature was therefore used in the full bandwidth processing and will be used here as well. The bubble operator was produced from synthetic data and included in the module. The synthetic input wavelet, the operator and the output designature with their corresponding frequency and phase spectrums can be seen in **Fig. 5.21**.

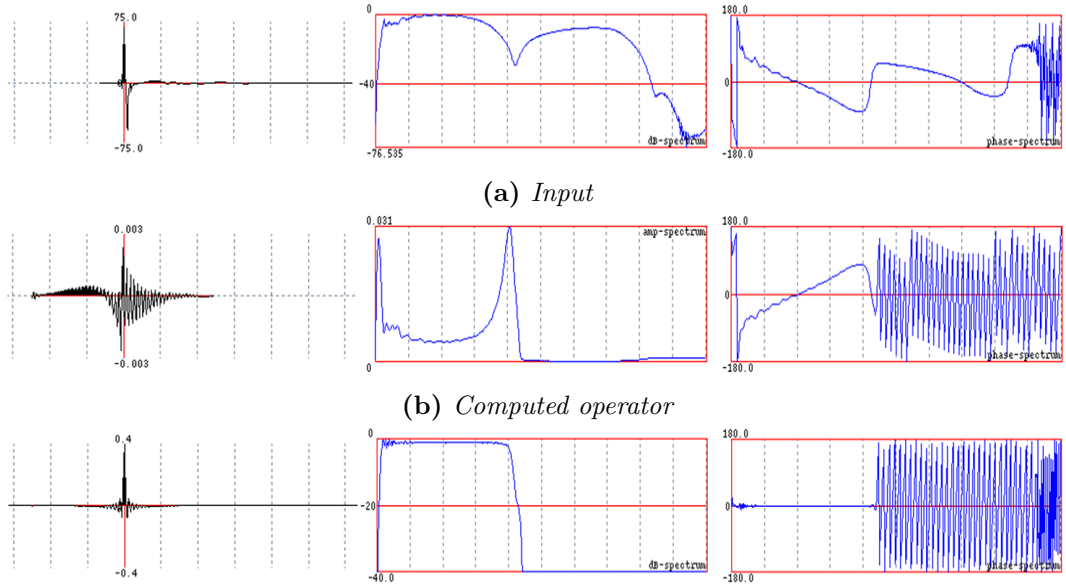

(a) *Input*

(b) *Computed operator*

(c) *Output*

Figure 5.21 – *The source ghost and zero-phasing shaping process. (a) The synthetic wavelet, displayed in time, frequency spectrum and phase spectrum, was used as input to compute the operator in (b). The operator was applied to each trace in the input, ideally giving the zero phased wavelet with the flat spectrum and consistent phase as shown in (c).*

A recently developed receiver deghosting technique was selected as the last step in the deghosting process. The method is explained in Poole (2013) and will be referred to as the ghost wavefield elimination (GWE) method. The idea is based on the least squares linear Radon equations. A transform from the frequency domain can be done with

$$d = Lp, \tag{5.1}$$

.

where d is the input shot gather, p is a frequency slice in the τ-p domain and L is the linear transform operator. Since the time shifts in L are linear with offset for plane waves, the equation is limited to flat streamer data. To correctly align up-going or down-going energy in the case of variable-depth streamer data, modifications to Eq. 5.1 are needed. After correcting the traveltime elements, the up-going (L_u) and down-going (L_d) terms can be joined to one single linear equation which both redatums and reghost:

$$d = L_{ud} p_{z_0}, \tag{5.2}$$

where $L_{ud} = L_u + RL_d$, R is the free surface reflection coefficient and p_{z_0} is the ghost free τ-p transform at sea surface datum. By formulating the problem in this way, a point in the Radon domain splits to one primary and one ghost in the t-x domain. The ghost part can then be subtracted from the input data. **Fig. 5.22** illustrates the two principles where the primary and the ghost registered by a receiver corresponds to different surface locations and the inverse process that produces a receiver ghost model.

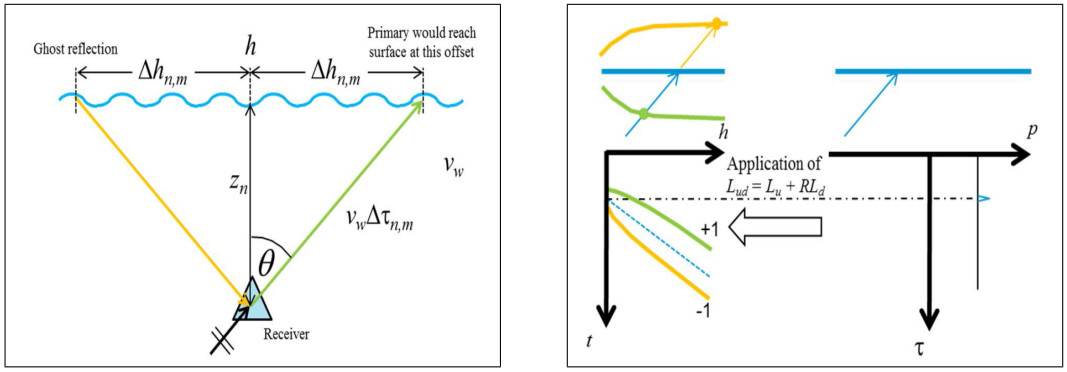

(a) *Surface geometry* **(b)** *The inverse transform*

Figure 5.22 – *(a) The upgoing primary ray (green) arrives at surface offset $h + \Delta h$, but will reach the receiver at an earlier time of $-\Delta t$. For the downgoing ghost ray (yellow), the surface has already been reached (at $h - \Delta h$) earlier by a time Δt. This is corrected for in the modified versions of the traveltimes which are included in L_u and L_d. The depth, z_n and water velocity, v_w, are also components included in the modified traveltimes. (b) demonstrates how a point in the τ-p domain transforms to a primary reflection (green) and a mirror reflection (yellow) with the new formulation. The mirror reflection can then be subtracted from the data. Source: Poole (2013).*

Results

There were not many parameters that could be adjusted in the first shaping module. Testing of this process was therefore limited to quality control of how the low frequencies were handled. The isolated model of the bubble was extracted for illustration purposes and can be seen together with its frequency spectrum in **Fig. 5.23.**

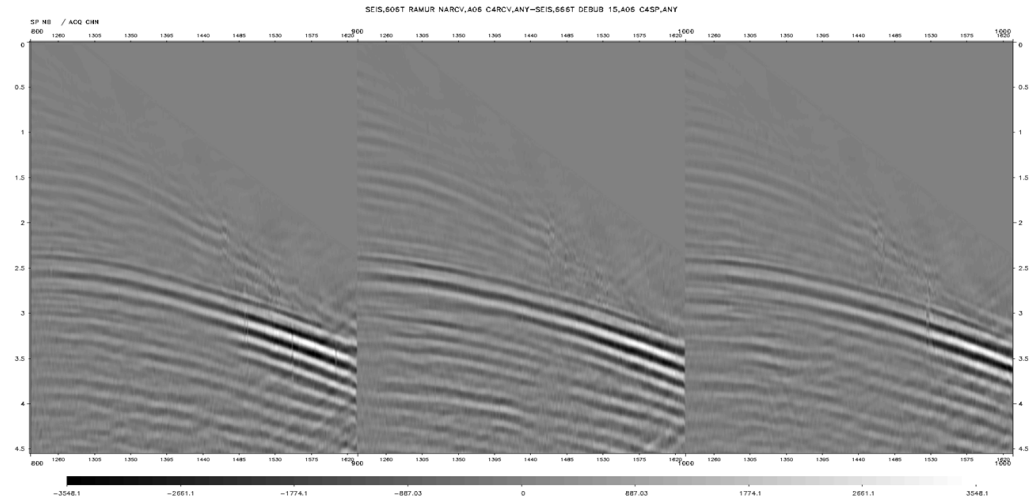

(a) *D1: Bubble model*

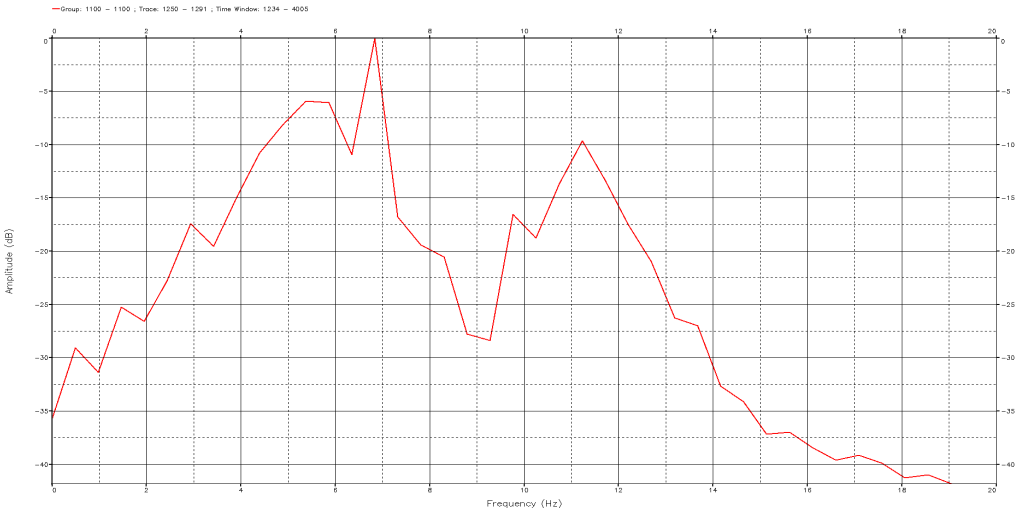

(b) *D1: Bubble model spectrum*

Figure 5.23 – *The bubble model in (a) was subtracted from the data. (b) shows the spectrum of the bubble model. Note the bubble notch at 8-9 Hz. As the figure illustrates, the bubble contains much low frequency information. Accurate modelling of the bubble will be very important for the low frequency quality. A real, more accurate, source signature would therefore be preferable.*

Secondly, the module was applied as it was designed for, with the debubble included in the wavelet shaping process. The source deghosted, debubbled and zero-phased result is included in **Fig. 5.24**.

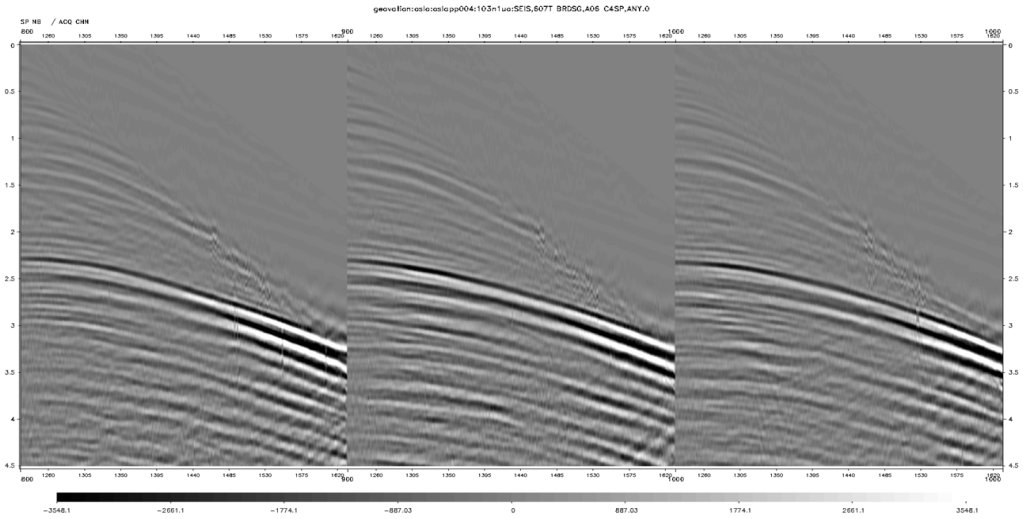

Figure 5.24 – *D1: Output after the wavelet shaping.*

A closer look on the chalk revealed that the module seems to work satisfactory for the low frequencies, illustrated in **Fig. 5.25.**

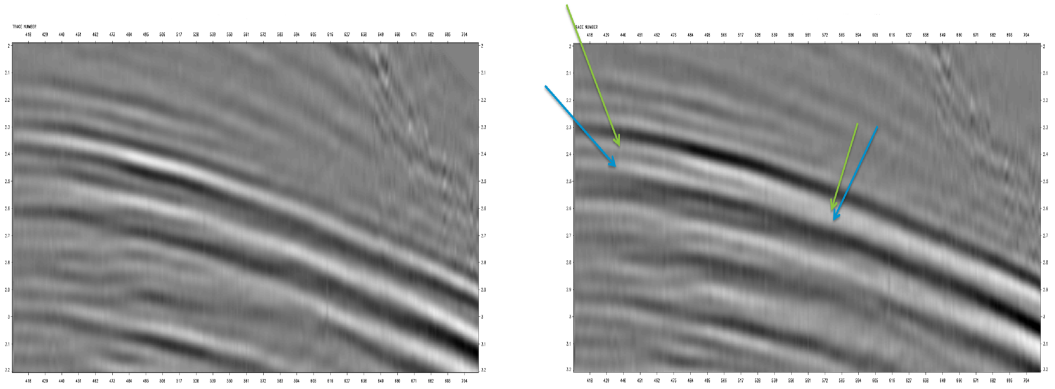

(a) *Input* **(b)** *Output*

Figure 5.25 – *D1: A close up on the chalk shows that the module successfully removes the source ghosts and is zero-phasing the wavelet with its shaping process. (a) is the input data and (b) is the output data. In (b), it is possible to distinguish between the receiver ghost (green arrow) and the multiple (blue arrow). Note also how the two tunes together against offset due to the variable-depth streamer profile. The main black peak that represents the chalk looks symmetrical with equal sidelobes, indicating that the zero-phasing is performing well. Data shown are from 2000 to 3200 ms with 300 traces displayed horizontally.*

The amplitude spectrum before and after the module was applied can be found in **Fig. 5.26** while the phase spectrum for the same data is given in **Fig. 5.27**

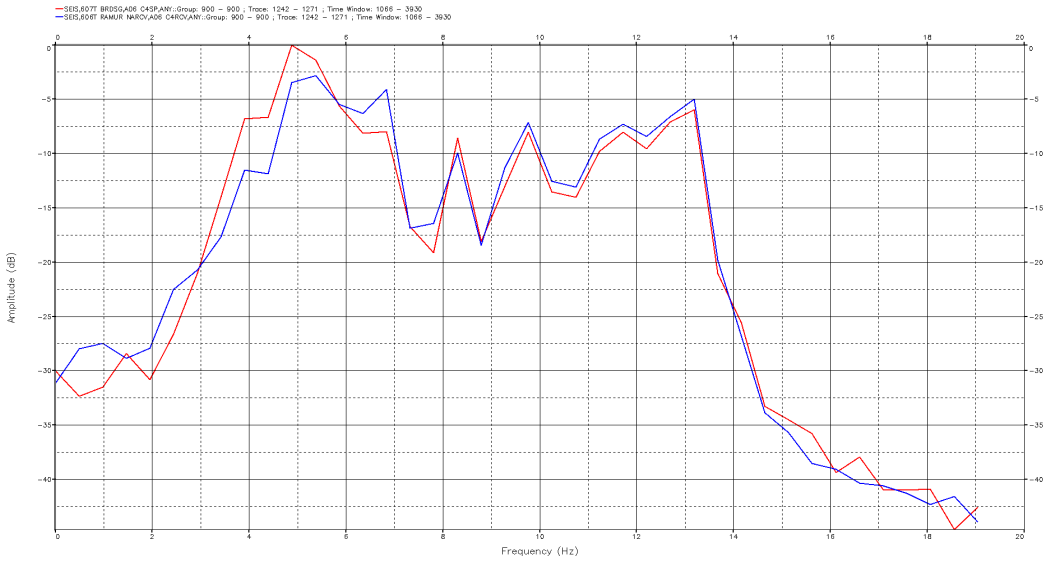

Figure 5.26 – *D1: The frequency spectrum before (blue) and after (red) shaping of the signature and debubble. Note how the amplitudes around 4-5 Hz have been strengthened in the process.*

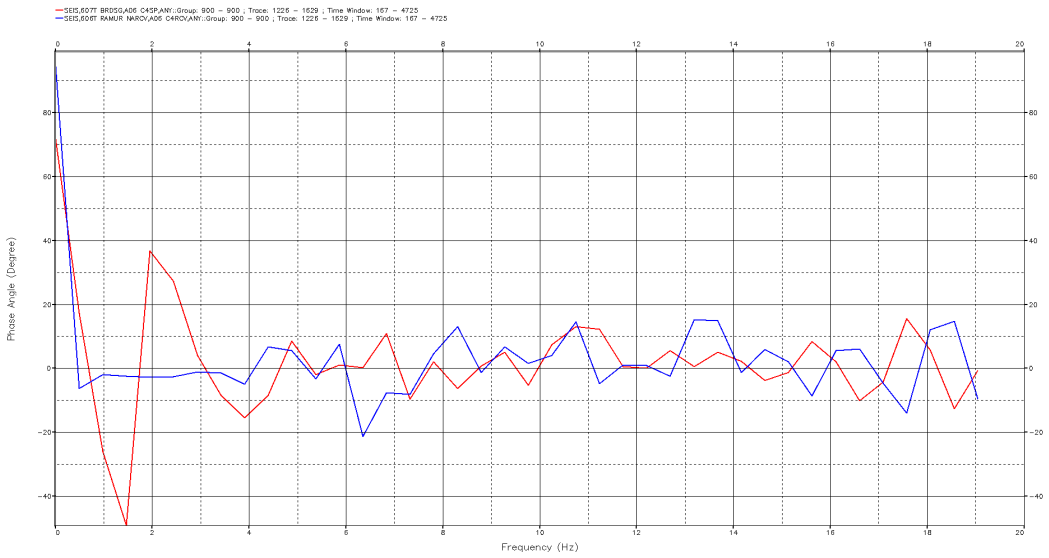

Figure 5.27 – *D1: The phase spectrum before (blue) and after (red) signature shaping and debubble. Note how the red line is keeping closer to the zero phase angle line. The high angles for the frequencies below 2.5 Hz should be neglected and are considered originating from very weak noise.*

The receiver deghosting module had parameters that were tested. Although no significant changes were found to improve the performance, it is worth mentioning that several operator windows, frequency bands, water velocities and iteration numbers were tested. In addition, filtering D2 data after deghosting to D1 range gave almost identical results. The final deghosted result is shown in **Fig. 5.28.** The chalk in **Fig. 5.29** illustrates a successful removal of the receiver ghost.

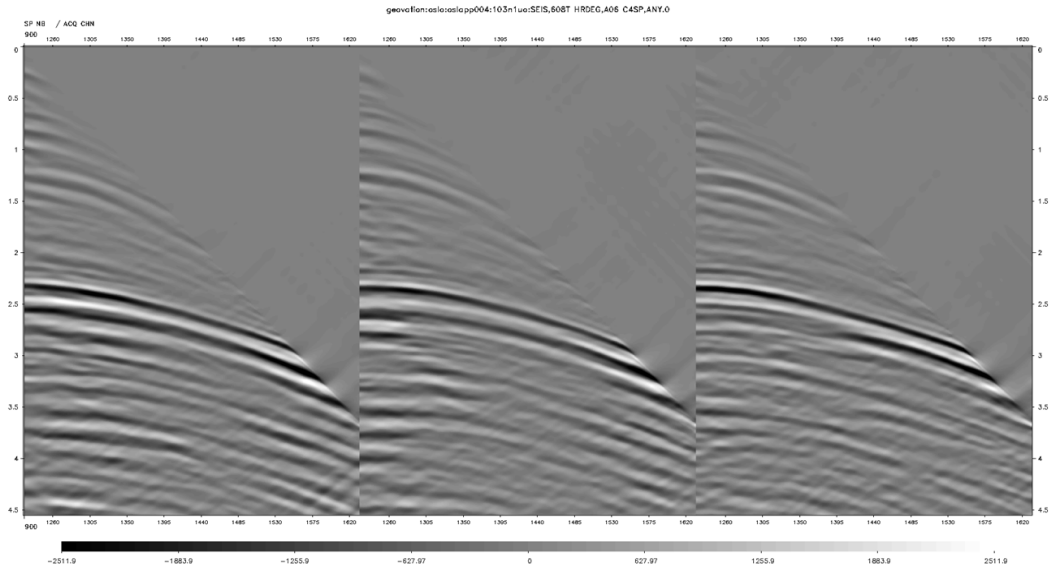

Figure 5.28 – *D1: The figure shows the shot gathers after receiver deghosting.*

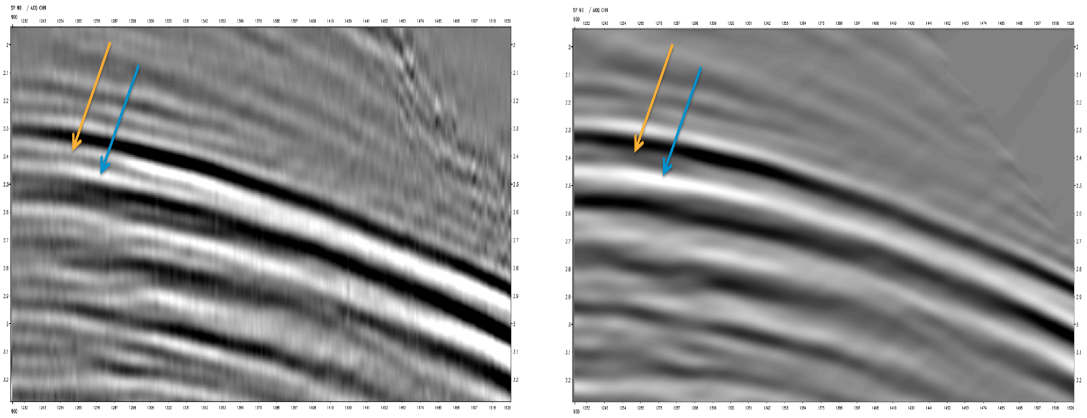

(a) *Input* **(b)** *Output*

Figure 5.29 – *D1: A close up of the chalk after receiver deghosting. (a) shows the receiver ghost as the orange arrow while the water bottom multiple is indicated by the blue arrow. (b) shows that the receiver ghost is removed and the water bottom multiple remained untouched. Data shown are from 2000 to 3200 ms with 300 traces displayed horizontally.*

An interesting test was performed as an alternative to the first method. By sorting the data in the receiver domain, the GWE method could be applied to remove the source ghost. Afterwords, the data can again be sorted in shot gathers and the same method used for the receiver deghosting. In many ways, this is more correct than shaping the signature as it actually subtracts the unwanted signal away from the data. A separate debubble subtraction was then needed before removal of the ghosts. A spectrum comparison between the alternative of shaping followed by GWE and the alternative of two times GWE is shown in **Fig. 5.30.** Since the zero-phasing not has been applied in the last alternative, it must be noted that some uncertainties are related to the spectrum comparison.

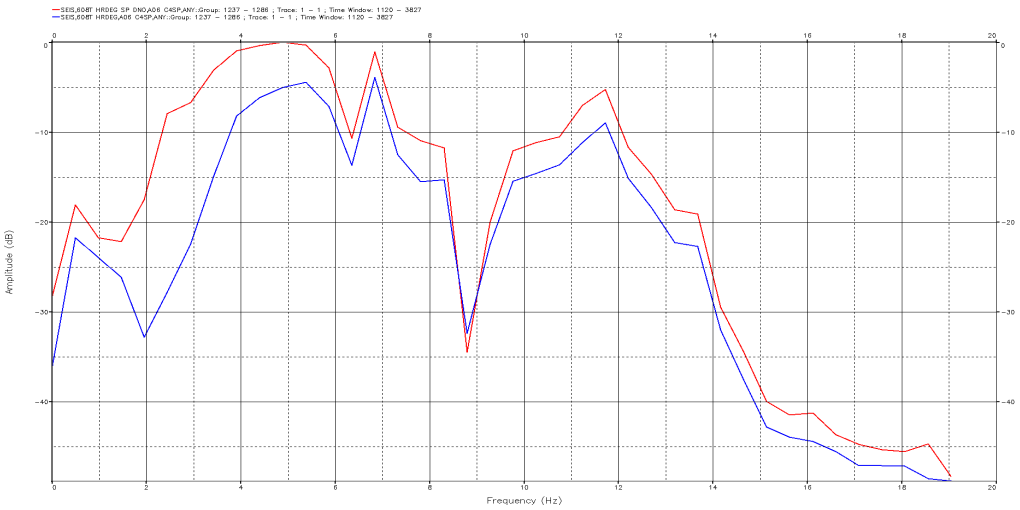

Figure 5.30 – *D1: Frequency spectrums for the two deghosting alternatives. The alternative with two times GWE (red) gives stronger amplitudes around 4-5 Hz. As some challenges are related to this comparison, no certain conclusions can be drawn based on the figure alone. However, it is interesting that the two alternatives yields differences around the lower frequencies. The horizontal axis goes from 0 to 20 Hz.*

Observations

- The signature shaping module works satisfactory for the low frequencies when neglecting that the synthetic input might be inaccurate.
- The receiver deghosting module seems to correctly remove the ghost without introducing artefacts by use of common full bandwidth parameters.
- GWE used on both ghosts gave an apparent stronger low frequency signal around 4-5 Hz.

Evaluation and continuation

Although the deghosting process appears to be successful, some uncertainties can be discussed. It is well known that the available synthetic signature models have room for improvements on the low frequency end. One reason for this has to do with difficulties in modelling the bubble. Since the bubble itself contain much of the low frequency energy, some tests were done on the synthetic signature. How the P/B changes dramatically when extracting the lower frequencies from the raw signature is shown in **Fig. 5.31.** It is clear from the figure that it will be critical to zero-phase such data adequately. Real signature shaped data would therefore potentially improve the low frequency response. However, the method used here was accepted as sufficient for removal of the source ghost, the bubble and for zero-phasing. Since this also was used in the full bandwidth processing, the continuing processing will use shaped data from the synthetic model. On the receiver side, a signature was not needed as the method is data driven. From studying how GWE affected the chalk, there is reason to believe that the method was operating satisfactory. The GWE parameters from the FBD will be used in the continuation. GWE on both sides should be explored as a possible alternative, but as it was desirable to compare to the full bandwidth flow, no further attempt to use this in the processing continuation was done.

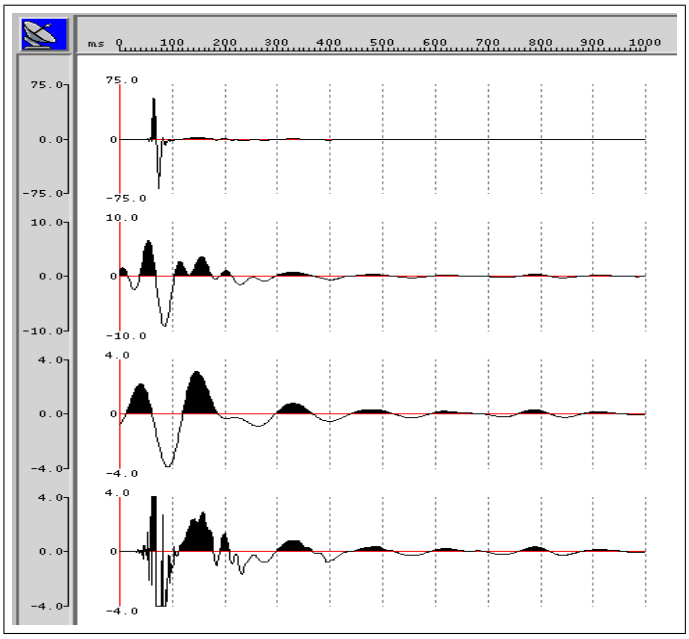

Figure 5.31 – *Modelled bubble period is close to 150 ms. The upper raw signature was filtered to 20 Hz and 10 Hz, resulting in the second wavelet and the third wavelet from the top, respectively. Note how the vertical axis change and how the P/B reduces for lower frequency content. The importance of a correct bubble model for low frequencies is then obvious. The lower wavelet is the raw signature with the same scaling as the 10 Hz filtered wavelet.*

5.2.5 Demultiple

The step is divided in modelling of the multiples and a method in how to subtract them from the data. Demultiple was assumed a critical step because much of the frequencies in the data are below the multiple tuning frequency.

Method

Because of the seabed tuning problem, a multiple modelling method based on the overall data, and not only the seabed, was needed. One appropriate technique is shallow water demultiple (SWD) (Yang and Hung, 2012). This method can be divided in three major steps. First, the primary reflection from the seabed is found from the second order water bottom multiples. Secondly, this is used to create a multiple model that can be adaptively subtracted from the input as the third step. The periodicity in the data is found from the autocorrelation. This is a mathematical operator aiming towards identifying similarities between observations as a function of time lag between them. Since the major repeating pattern in the data is the water bottom multiples, they will be targeted and also the second order multiples will be predicted from the first order multiples. The module operates with multiple traces to compute the autocorrelation. After the model has been created, it can be subtracted from the data. The common subtraction module is an adaptive method trying to increase the resemblance between the input data and the multiple model under the least squares minimum energy criteria in the time-space domain. Both the model building and the subtraction were tested. The multiple model was tested with different frequency bands as input, while the parameters in **Table. 5.5** were tested in the adaptive subtraction. A full offset shot gather displayed from 0 to 4500 ms with consistent gain is presented in the figures unless stated otherwise.

Parameters tested	**Description**	**Sensitivity**
Number of traces	The number of traces used for finding the resemblance and subtract.	Not sensitive
Sliding windows	Length of temporal and spatial elementary processing block and overlap between two successive blocks	Sensitive
Frequency split	The frequencies used in the operation can be split in intervals with different parameters	Sensitive
Iteration numbers	Number of iterations needed to optimize the adaptive subtraction	Not sensitive
Start time	The adaptive subtraction can start at a defined time	Sensitive

Table 5.5 – *Tested adaptive subtraction parameters.*

Results

SWD turned out to be a good multiple model builder for the low frequencies. The produced model from the input can be seen in **Fig. 5.32.**

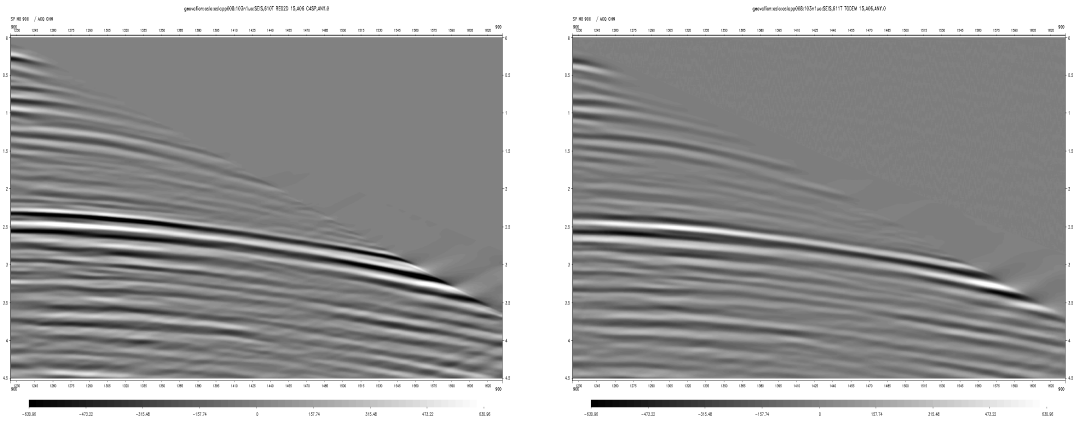

(a) *Input* **(b)** *Multiple model*

Figure 5.32 – *D1: Input (a) and multiple model (b) obtained from the SWD model builder.*

The adaptive subtraction proved to be the main issue in the demultiple step. How the removal of multiples resulted in contaminations is included in **Fig. 5.33.** This can especially be seen below the seabed and below the chalk. By changing the sliding window parameters to bigger windows compared to the full bandwidth set up, a modified version of the adaptation was achieved, which gave a visually cleaner shot gather.

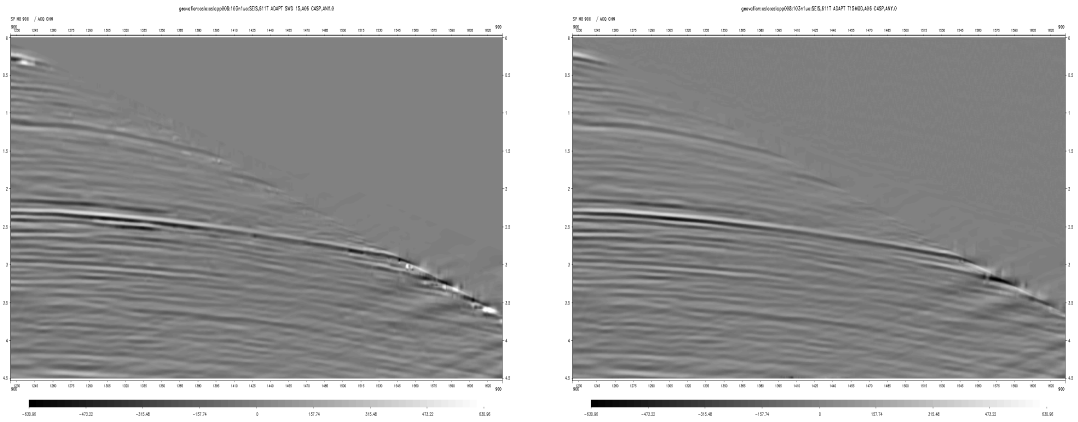

(a) *FBD adaptive subtraction* **(b)** *Modified adaptive subtraction*

Figure 5.33 – *D1: FBD parameters used in the adaptive subtraction can be seen in (a), while the demultiple result using the modified version is given in (b). The modified multiple removal gives a visually less contaminated gather.*

The same demultiple sequence was also investigated for D2. The input with produced model from the SWD method is given in **Fig. 5.34.**

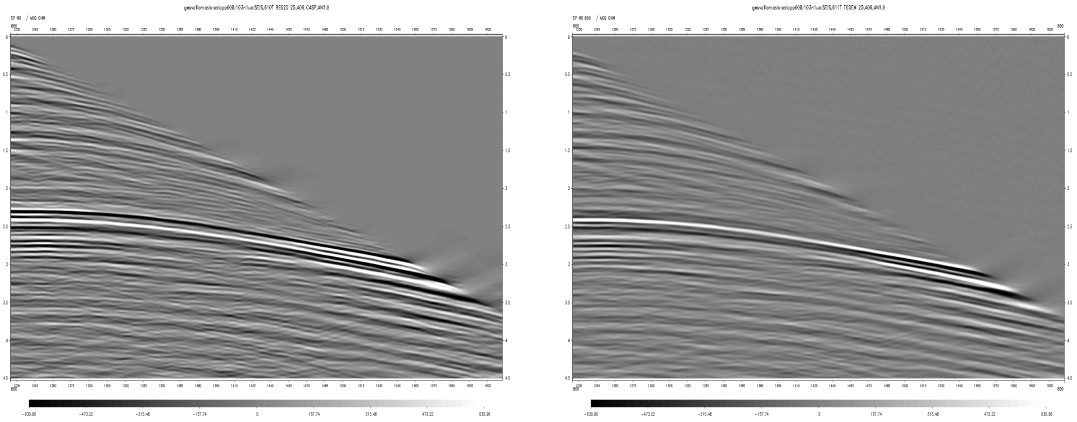

(a) *Input* **(b)** *Multiple model*

Figure 5.34 – *D2: Input (a) and multiple model (b) using the SWD model builder. Note especially how the positive (black) reflection from the chalk is excluded in the multiple model, indicating that the module works satisfactory.*

The higher frequencies in D2 help illuminating where the main multiples are located. Comparison with the D1 model shows that they corresponds well. Testing of the adjustable parameters in the adaptation revealed much of the same as for the D1 testing. Larger sliding windows provided cleaner shot gathers. However, the performance using FBD parameters was better for D2 than for D1. These results are included in **Fig. 5.35.**

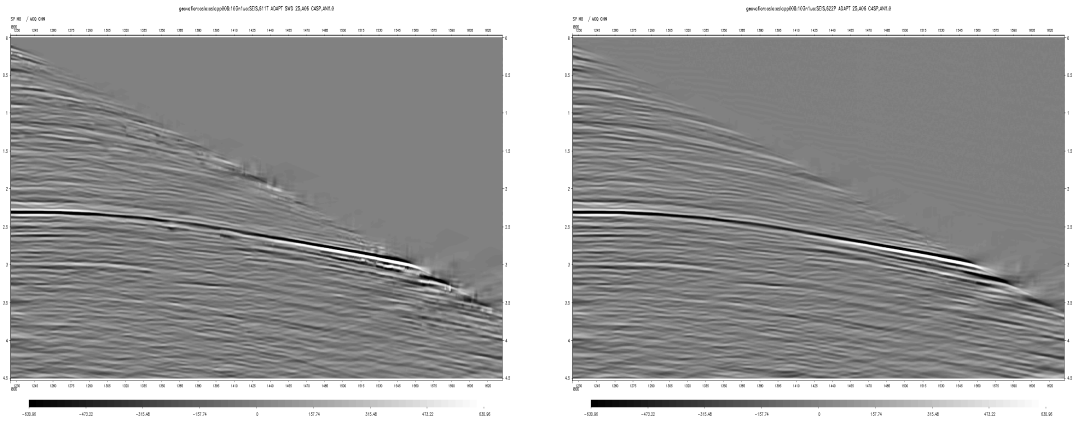

(a) *FBD adaptive subtraction* **(b)** *Modified adaptive subtraction*

Figure 5.35 – *D2: FBD parameters used in the adaptive subtraction can be seen in (a), while the demultiple result using the modified version is given in (b). Note how the multiple (white) below the chalk is removed.*

The adaptation problem was explored further by applying a low-pass filter on D2 data to compare with the D1 result. The same demultiple parameters were used for both sets. A comparison between them is shown in **Fig. 5.36.**

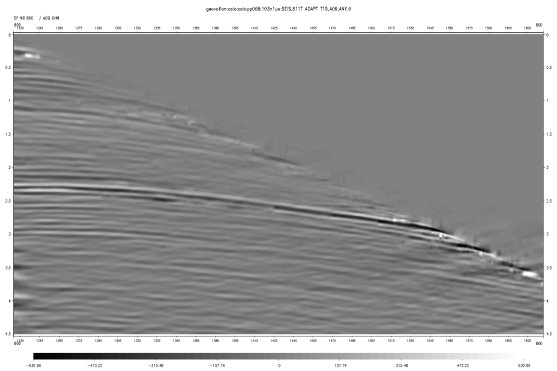

(a) *D1*

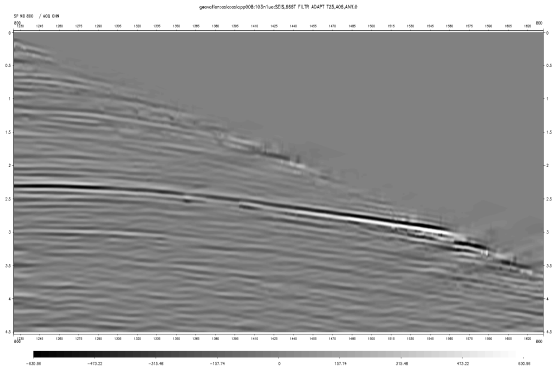

(b) *D2*

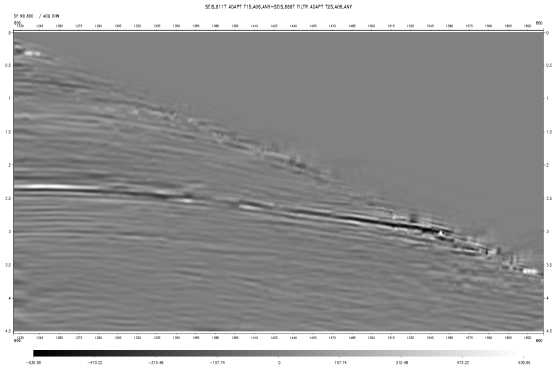

(c) *Difference between (a) and (b)*

Figure 5.36 – *(a) is the demultiple result from D1 processed data while (b) is the low-pass filtered demultiple result from D2 processed data. (a) and (b) should be approximately identical, but the difference section in (c) reveals that there are big differences. This indicates an adaptive subtraction process that heavily depends on frequency content in the input data.*

Since the deviations between the D1 demultiple result and D1 component of the D2 demultiple result were significant, it is obvious that the adaptive subtraction method depends on the frequency content of the input data. When this was observed, it was prioritized to examine more of why this was happening. A synthetic wavelet modelling was done by creating a 1D time series with both primaries, multiples and their combined response. This was achieved by convolving the synthetic signature with a known reflectivity series with multiple period close to the real period in the actual data (100ms). Bandwidths tested were 3-80 Hz, 3-20 Hz and 3-10 Hz with the idea of representing the FBD, D2 and D1, respectively. The synthetic model and the problem related to the adaptation are explained in **Fig. 5.37.**

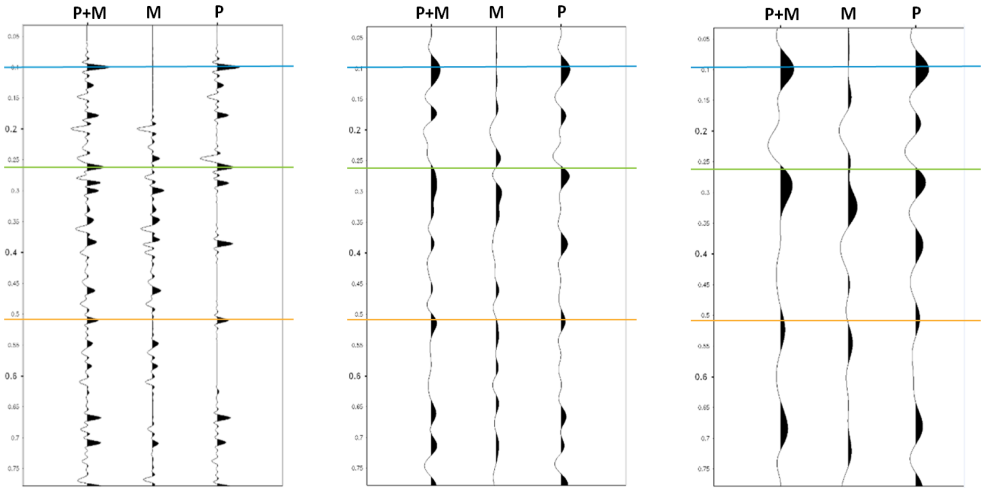

(a) *3-80 Hz* **(b)** *3-20 Hz* **(c)** *3-10 Hz*

Figure 5.37 – *Synthetic modelling of primaries and multiples (left traces), the isolated multiple component (middle traces) and the isolated primaries (right traces) for bandwidths of 3-80 Hz (a), 3-20 Hz (b) and 3-10 Hz (c). Note how the aligning of the peaks are consistent for the first event (blue line) between all the bandwidths. An apparent phase rotation can be seen (green line) between the different wavelets when the multiples are starting to interfere. The adaptive subtraction method tries to find the resemblance between the multiple trace (middle) and the combined primary and multiple trace (left). After subtraction, the primary trace (right) is obtained. In (a), the multiple model can be recognized, well seen around the first multiple (0.2 s). The situation gradually gets worse when entering into (b) where the amplitude fluctuations for the multiple trace are hard to detect with certainty in the combined trace. Absence of good resemblance between left and middle trace in (c) indicates that the adaptation process may struggle. The P and M in the headers stand for primary and multiple, respectively.*

The above figure illustrates that the adaptive subtraction not is straight forward for the lowest frequencies. In this example, since the wavelets are stationary, a subtraction without adaptive properties would of course result in the primaries in the right traces. However, in real data this is only valid where the modelled multiples are very precise.

The same adaptive subtraction that was used in the processing was tested on these wavelets. The hypothesis of the module being dependent on the frequencies in the input data and struggling below the multiple tuning frequency seemed to be correct. The ideal primary traces compared with the primary traces after the adaptive subtraction are shown in **Fig. 5.38**. Here, a time window of 400 ms, overlap of 200 ms, operator length of 22 ms and 10 iterations were used in the adaptive subtraction process.

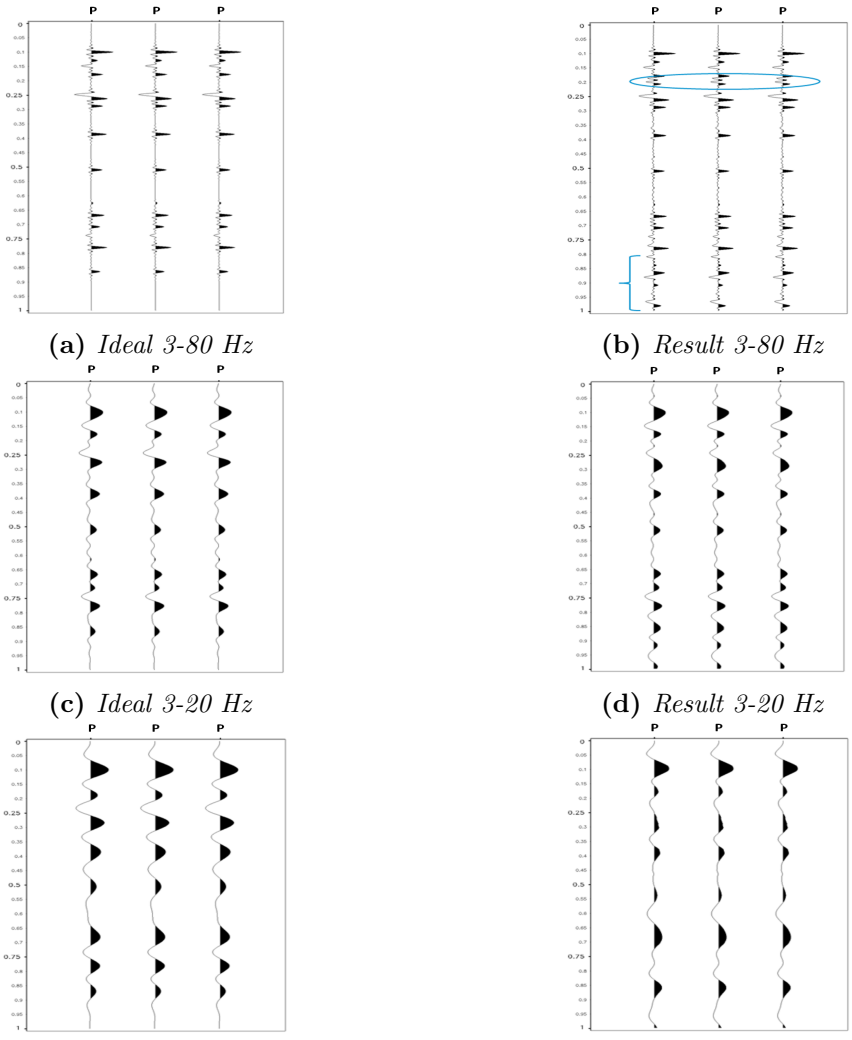

(a) *Ideal 3-80 Hz* **(b)** *Result 3-80 Hz*

(c) *Ideal 3-20 Hz* **(d)** *Result 3-20 Hz*

(e) *Ideal 3-10 Hz* **(f)** *Result 3-10 Hz*

Figure 5.38 – *Synthetic adaptive subtraction for different frequency bands using the input traces from Fig. 5.37. Three identical primary traces are displayed inside each of the figures. (a) and (b) have much similarities and the adaptive subtraction performance is considered good. Artefacts around the first multiple and the edge effects (marked in blue) are assumed introduced because of a short time window and could easily be corrected for. (c) and (d) looks quite similar, but with some minor amplitude and phase issues. (e) and (f) have differences that are not acceptable. Note especially how the representation fails in the 0.25-0.5 s interval.*

Although introducing some edge effects at the end of the trace, it is clear that the similarity between the true primaries and the adapted and subtracted primaries are acceptable for both the 3-80 Hz band and the 3-20 Hz band. However, the synthetic data reveals that the module does not not handle the 3-10 Hz data satisfactory. Low-pass filtering of the higher bandwidth wavelets was done to investigate if the low frequency response was equal for the different datasets. Filtering larger bandwidth data down to 3-10 Hz shows improved responses than seen in the isolated 3-10 Hz data. Also the 3-20 Hz data filtered to 3-10 Hz is better than the isolated 3-10 Hz result. These observations and comparisons can be seen in **Fig. 5.39** and **Fig. 5.40**.

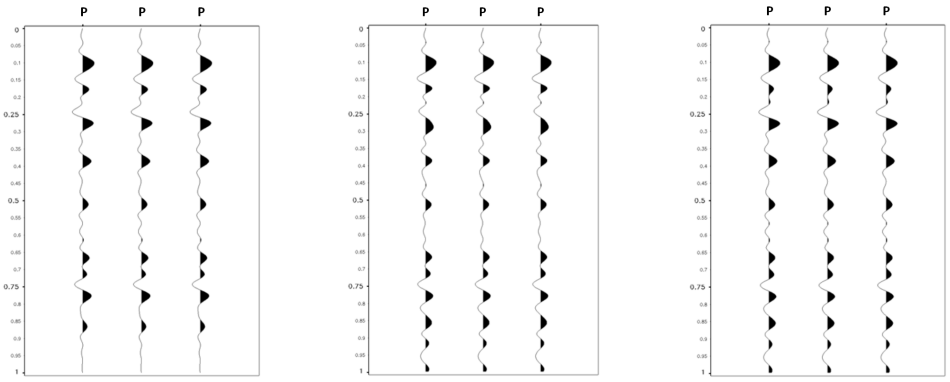

(a) *Ideal 3-20 Hz* **(b)** *Result 3-20 Hz* **(c)** *Filtered 3-80 Hz*

Figure 5.39 – *Adaptive subtraction 3-20 Hz comparison.(a) shows the ideal trace, (b) shows the result obtained from the 3-20 Hz data (repeat figure from Fig. 5.38) while (c) is the 3-80 Hz wavelet low-pass filtered to 3-20 Hz. The visual differences are seen around the first multiple (and the edge effects introduced at the end of the trace). These three wavelets are tolerably similar and the module is therefore believed to perform well in this frequency range.*

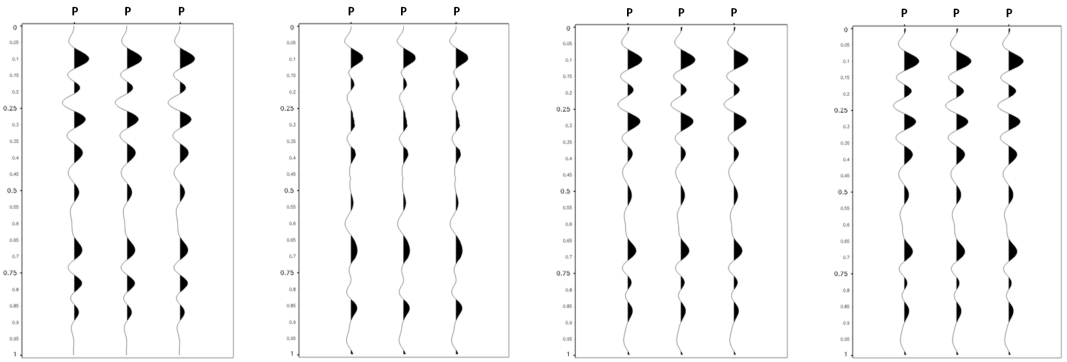

(a) *Ideal 3-10 Hz* **(b)** *Result 3-10 Hz* **(c)** *Filtered 3-20 Hz.* **(d)** *Filtered 3-80 Hz.*

Figure 5.40 – *Adaptive subtraction 3-10 Hz comparison. (a) is the ideal primary trace, (b) is the 3-10 Hz result (repeat figure from Fig. 5.38), (c) is 3-20 Hz data low-pass filtered to 3-10 Hz, while (d) is the 3-80 Hz wavelet low-pass filtered to 3-10 Hz. Both (c) and (d) have superior similarities to (a) than the result in (b).*

The last attempt to improve the demultiple step was carried out by replacing the adaptive subtraction with a direct subtraction. If such methods shall be successful, a reliable multiple model is extremely important. In this case, the SWD method proved to work very well and since it is driven by the data, the multiples line up quite correctly. Other demultiple methods might need a better statistical approach to match the model, such as the adaptation discussed here. The direct subtraction result can be seen in **Fig. 5.41.**

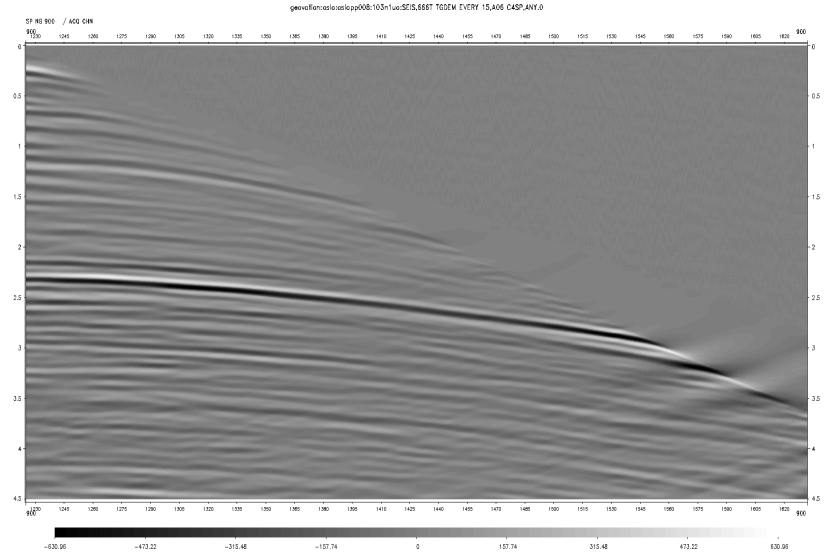

Figure 5.41 – *D1: The direct subtraction alternative seems to work better than adaptive subtraction in this case. The chalk looks more continuous and the general impression is that the section looks cleaner when produced using the adaptation module.*

Observations

- Building multiple models using the SWD technique seems like a solid option for the low frequencies.
- Adaptive subtraction has trouble for frequencies below the multiple tuning frequency. The problem is related to the adaptation stage where the module is finding it difficult to see the resemblance between input and model.
- Synthetic modelling shows that the low frequency adaptation benefits when more octaves on the high frequency side are included in the input data.
- Modifying the adaptation by increasing the sliding windows (making the adaptation milder) gives a result with seemingly less artefacts. If the available multiple model is very solid, a direct subtraction might be a better option below the multiple tuning frequency.

Evaluation and continuation

From the synthetic modelling, it can be seen that the frequency range in the input data decides the quality of the adaptation. This was exactly what was observed in the results. However, the effect illustrated in the results and the modelling indicate that low frequencies, especially below the tuning frequency, must be handled with special care. The positive reaction from increased sliding windows and the good result from the direct subtraction makes it an option to split the subtraction step into a low and high frequency band. The low part might benefit from a milder subtraction or the adaptation step can be replaced by a direct subtraction. However, a frequency split that provides the lower band with only low frequency data should be avoided due to the guiding effect the high frequencies have on the low frequencies in the adaptation. The modified parameters in the adaptive subtraction will be used in the further D1 and D2 processing.

5.2.6 Corrections

The effects of receiver motion, amplitude striping and tides were corrected for as it was for the FBD processing.

Method

The shot detected by a receiver occurs at a given time after the actual shot was fired. By this time, the streamer has moved a certain distance decided by the boat speed. To obtain shot consistent receiver locations, a time-variant spatial shift was applied to the data. This repositioning of traces will increase in importance for longer time intervals between shot fire time and receiver detection time. A constant boat speed was used.

Different sensitivity in recording equipment or inconsistency in the energy distribution can give amplitude variations along saillines. This inconsistency can be searched for and scaled to give a smooth amplitude distribution. The method will not impact any geologic variations, but corrections will be done if, for instance, a specific channel always give larger amplitudes than the surrounding channels.

The tide can be corrected for with an input table containing tide amplitudes as a function of time. Using this information, the headers can be updated with the tide value at which the shot was fired. The table used was the same as in the full bandwidth processing.

Results

The corrections are not easy to detect on the shot gathers without close study, but some time-shifts may be observed, especially at the deeper parts with long offsets. The corrected sections for D1 and D2 are given in **Fig. 5.42** and **Fig. 5.43**, respectively.

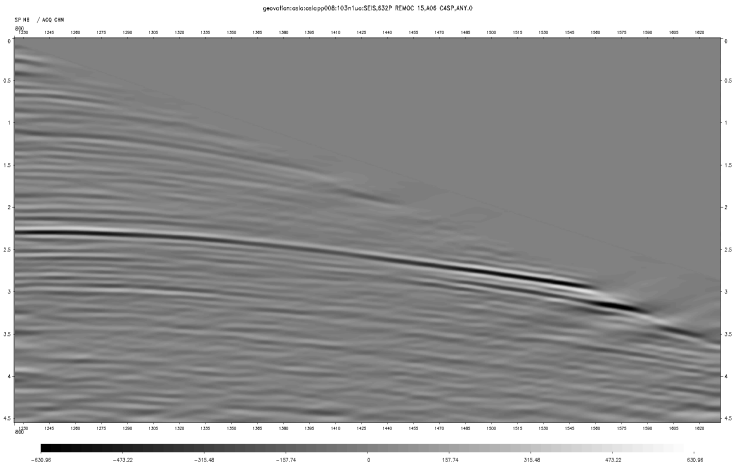

Figure 5.42 – *D1: A shot gather after applied corrections.*

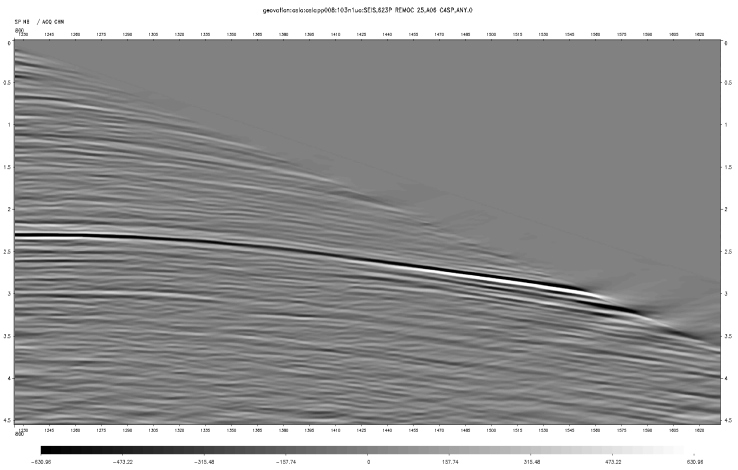

Figure 5.43 – *D2: A shot gather after applied corrections.*

Observations

- None of the used corrections introduced any challenges in the processing of low frequencies.

Evaluation and continuation

This step was neither expected nor found to produce any challenges for the low frequencies. It was however done to follow the full processing and to be able to qualitatively compare with other data after the final migration.

5.2.7 Binning and regularization

This part of the processing sequence is aiming at producing a grid with consistently placed traces throughout the whole survey.

Method

The binning step was carried out with the same grid as for the FBD processing. The grid cell dimensions were 12.5 x 25 meters in inline and crossline, respectively. The method used was a common binning process. First, the data is sorted in offset classes. Then the CMP's falling into the bin cells can be identified and their corresponding traces compared with the 4D legacy survey. The trace best matching the legacy survey is then selected into the bin cell. This was repeated for each offset class, making an ideally 81 points (81 offset classes were used) in each cell. Further, the regularization step moves the reflection points to the bin cell center and interpolates if some cells lack information. The method depends on a Fourier reconstruction of the input data before the reverse transform maps the data (in 2D) to the grid. Interpolation of missing traces can be done using the same reverse transform. Hence, after regularization the data is consistently displaced in the 2D grid. No attempt to test parameters in the binning was done as the step in many ways is more a sorting process than a signal process. The regularization was tested with several time windows, but no improvements were observed.

Results

Near, middle and far offset class spectrums after regularization can be seen in **Fig. 5.44**, while the corresponding common offset gathers are shown in **Fig. 5.45.** Although not directly showing the performance of the regularization, they will be used as input in the migration and does also illustrates the frequency differences with offset.

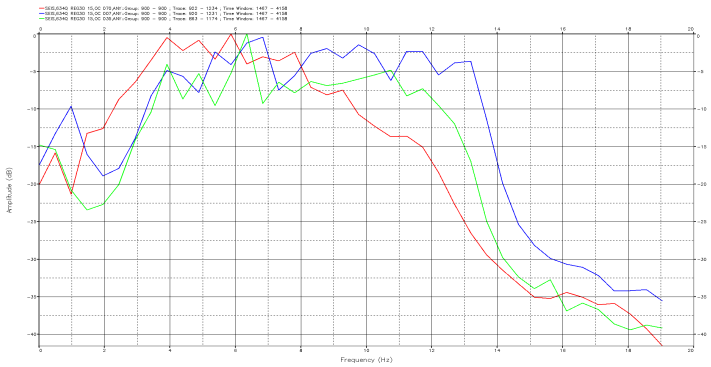

Figure 5.44 – *Note how the 3-5 Hz response apparently is better at far offset (red) than for middle offset (green) and near offset (blue). This may be because NMO stretch artificially introduces more lower frequencies at longer offset. 0-20 Hz is shown at the horizontal axis.*

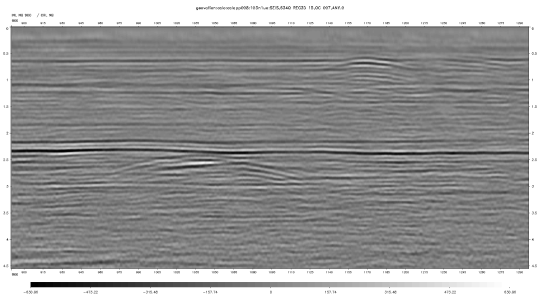

(a) *Near*

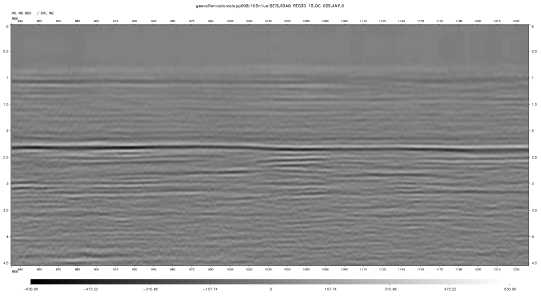

(b) *Middle*

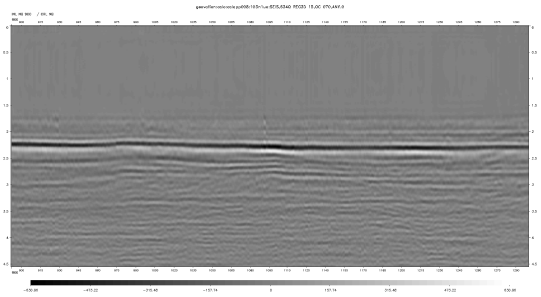

(c) *Far*

Figure 5.45 – *D1: Near (a), middle (b) and far (c) common offset gathers. Note how the critical angle limitation only allow deep recordings for the far offset class and that the section seems to have a lower frequency content than the other two due to the NMO stretch effect. Scale is 0-4500 ms with full CMP fold distance horizontally.*

Observations

- Both binning and regularization proved to work satisfactory in the used datasets.

Evaluation and continuation

Infill from the regularization was found to perform well. Since no parameters needed to be changed, D1 data and D2 data should be well comparable in the final stacks.

5.2.8 Imaging and stacks

The final step tested in the processing flow was migration. After migration, stacks were produced to compare the different datasets and to evaluate the progress made.

Method

The data was migrated with a common 3D Kirchhoff summation method. A pre-stack time migration (PSTM) version of the method was known to work satisfactory for all the frequencies in the dataset. No parameters were therefore changed compared to the full bandwidth processing, but quality control of the results were done with spectrum and stack comparisons before and after the migration.

The principle of the diffraction summation method is based on a hyperbolic mapping in the x-t domain from a single diffractor source (see Huygens principle in section 2.2.5) in the x-z domain. The traveltime of this hyperbola was given in Eq. 2.13. With a good velocity model, the diffraction points can then be searched for in the x-t domain. Summation along the traveltime equation with the obtained energy repositioned to the apex of the hyperbola will have a strong effect where the amplitude fluctuations corresponds to the actual hyperbolic moveout. For diffractions that originates from one single point source, this is exactly the case and they will therefore be collapsed into points. Reflecting surfaces can be regarded as consisting of a number of such point sources, but since destructive interference will occur from the neighbouring source points, they appear with a surface shape rather than many visible diffractions, except at the end points where no neighbours are present. Before diffraction summation, effects such as angle dependence of amplitudes, spherical spreading and wavelet shaping factors is beneficial to include in the algorithm. These factors are being compensated for in what is commonly referred to as the Kirchhoff summation method. The principle is illustrated in **Fig. 5.46.**

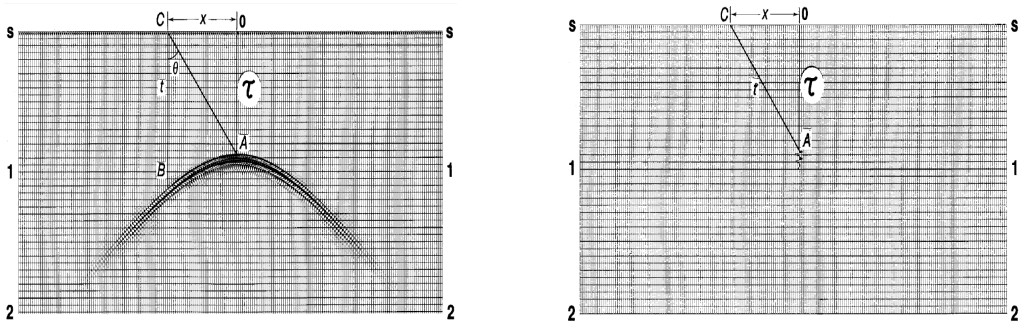

(a) *Diffraction hyperbola* **(b)** *Amplitude summation*

Figure 5.46 – *(a) A diffraction source point maps as a hyperbola in the x-t domain. Trace B is registered at the diffraction flank. (b) The energy is summed along the hyperbola and repositioned to the diffraction apex, resulting in a migrated image. Trace B will in this manner be repositioned to point A. Source: Yilmaz (2001).*

Results

As the migration method operates 3D pre-stack, the full effect is best displayed after stacking. Both the regularized data and the migrated data were stacked for comparisons. The pre and post migrated sections from processing of D1 can be seen in in **Fig. 5.47** and **Fig. 5.48.** The gain is equal in both figures.

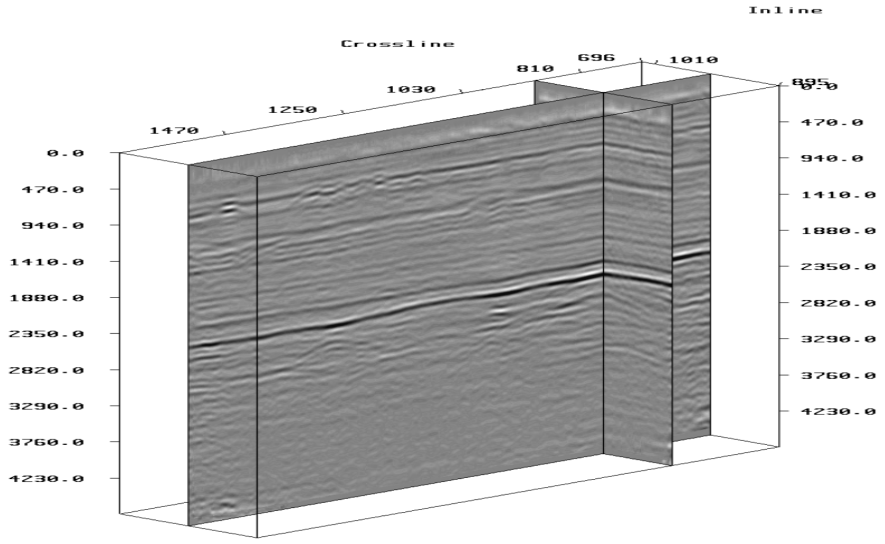

(a) *Pre migration*

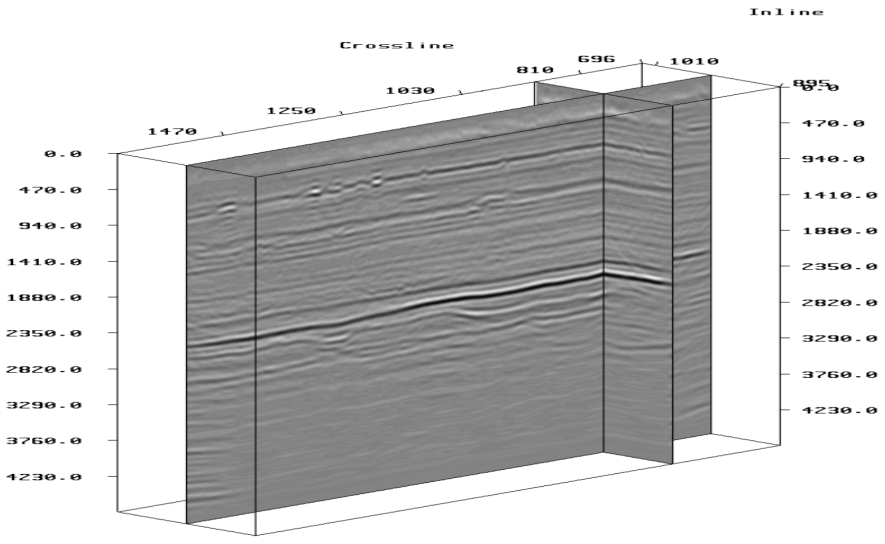

(b) *Post migration*

Figure 5.47 – *D1: Comparison of stacked data before and after migration. The diffractions in the input (a) have been focused well in the migrated section showed in (b). Note also how a possible small basin appears below the chalk at the crossline interception in (b).*

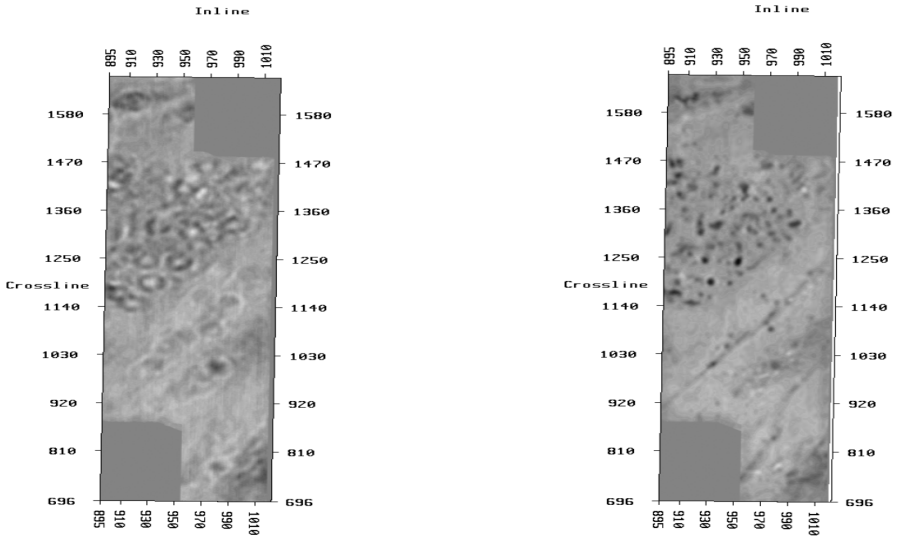

(a) *Pre migration* **(b)** *Post migration*

Figure 5.48 – *D1: The overall image seems more focused, which is proved in these 715 ms time slices of pre (a) and post (b) migration. Note how the hyperboloids in (a) collapses into points in (b).*

The time slices for the D2 processing are included in **Fig. 5.49**, while their full stacked sections are compared in **Fig. 5.50.**

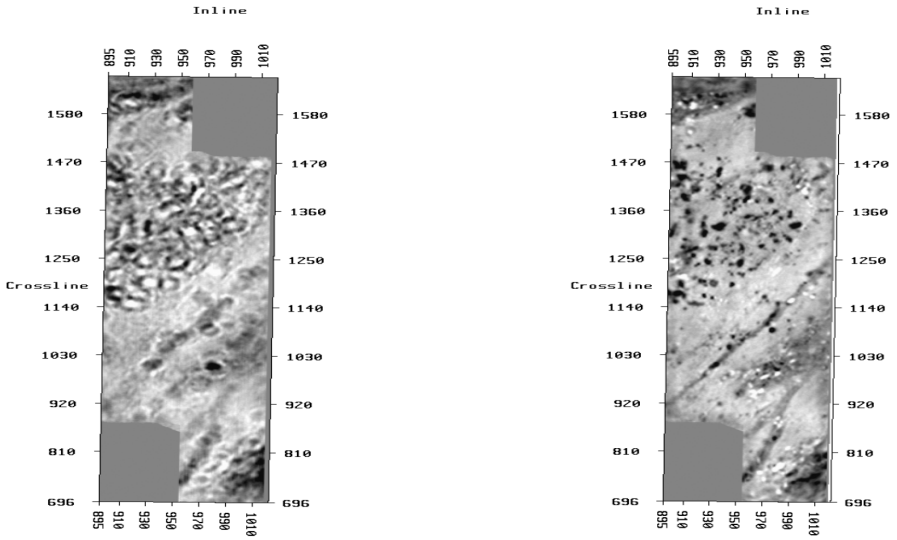

(a) *Pre migration* **(b)** *Post migration*

Figure 5.49 – *D2: Comparison of time slices at 715 ms before (a) and after (b) migration. The diffraction collapses are even better demonstrated in D2, where structures and details are revealed after migration.*

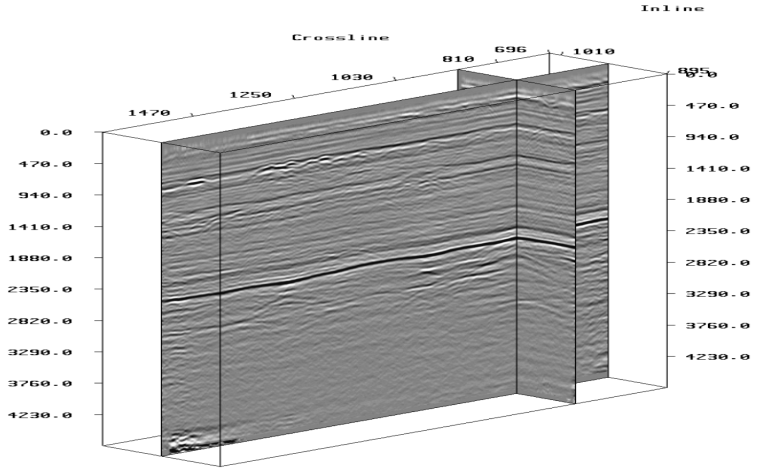

(a) *Pre migration*

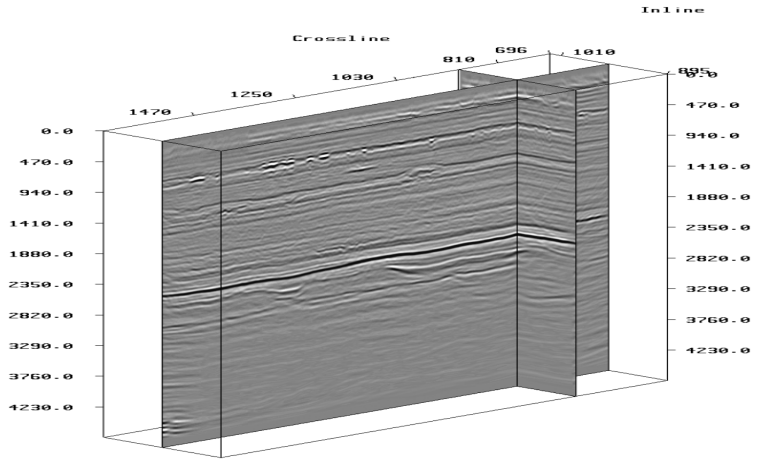

(b) *Post migration*

Figure 5.50 – *D2: Comparison of stacked data before and after migration. Note the focusing of the shallow gas accumulations around 700 ms.*

Further, now that the final processing is done, a comparison of the results can be visualized by filtering the higher bands to the lower bands and investigate possible differences. An inline of post migration D1 data is compared with the same bandwidth component of D2 and FBD in **Fig. 5.51.** Time slices were also extracted from the different datasets and a comparison is given in **Fig. 5.52.** The FBD has undergone additional minor steps throughout the processing so a concluding comparison can not be done. It is however regarded as the most correct dataset because of the guiding effect the high frequencies have in the adaptation (stated in this thesis) and the more comprehensive testing that was performed when the data was processed commercially. Hence, the processed D1 and D2 should ideally be as similar as possible to the corresponding frequency component in the FBD.

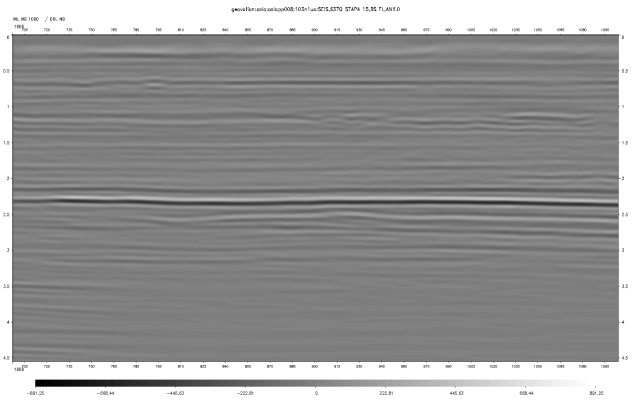

(a) *D1*

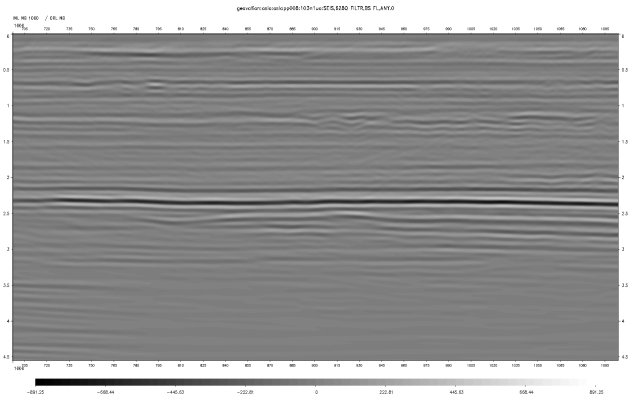

(b) *D2*

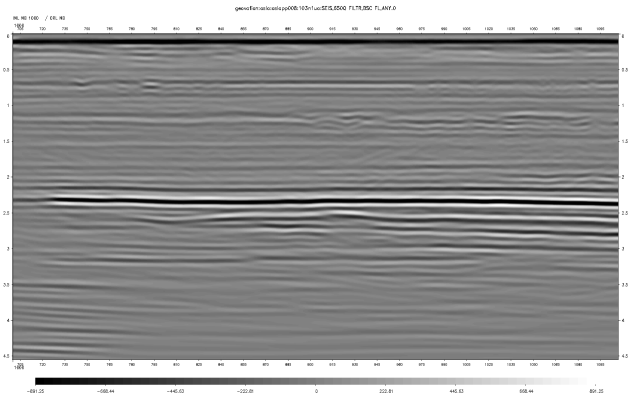

(c) *FBD*

Figure 5.51 – *Inline comparison of the D1 component of all datasets. D1 data can be seen in (a), D1 component of D2 can be seen in (b), while the same component of the FBD is given in (c). More details can be found in (b) and (c) than in (a), indicating that some data has been lost in the low frequency only processing, probably due to the adaptation problem. This assumption is strengthened by the better similarities that can be observed between (b) and (c). The full inline distance with time from 0 to 4500 ms are displayed.*

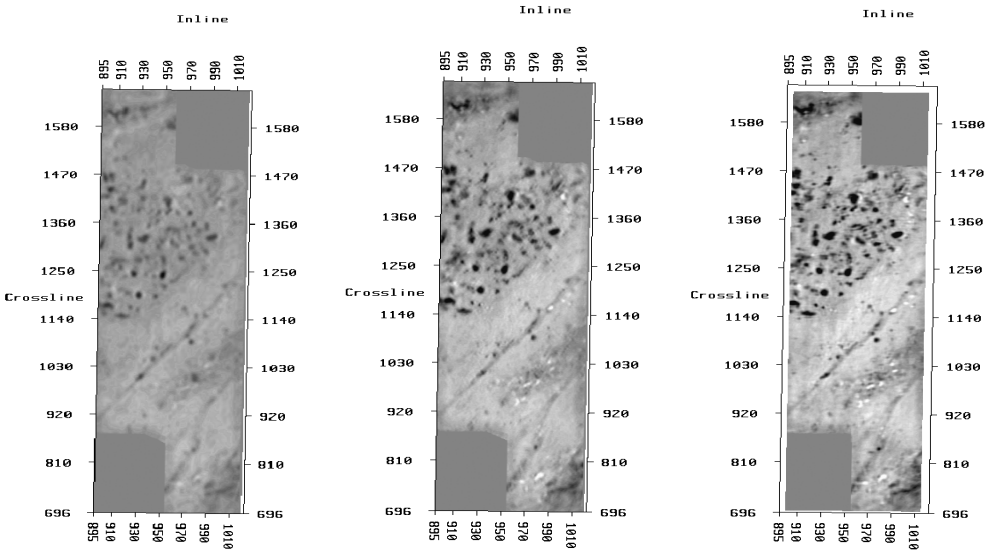

(a) *D1* **(b)** *D2* **(c)** *FBD*

Figure 5.52 – *Time slice comparison of D1 (a), D1 component of D2 (b) and D1 component of the FBD. The observations from Fig. 5.51 can be confirmed. (b) shows more similarities to (c) than (a). The differences between (b) and (c) are actually very small, indicating that the D2 processing has been successful, even at the adaptation stage. (a) seems to have lower S/N, but the main structures are visible. This indicates that the D1 processing has produced a fairly correct image, but does suffer from the adaptation artefacts.*

A spectrum comparison for D1 and D2 data before and after migration is included in **Fig. 5.53.**

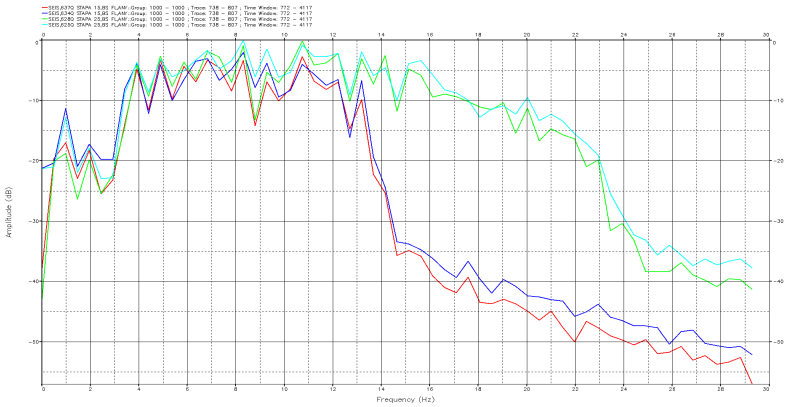

Figure 5.53 – *Frequency spectrums of pre and post migration D1 and D2 data. Blue represents pre migration from D1, red represents post migration from D1, cyan represents pre migration from D2 and green represents post migration from D2. The frequencies have been preserved well through the migration process, indicated by the similar spectrums. Horizontal axis goes from 0 to 30 Hz.*

The frequency spectrums belonging to the D1 components of all datasets are compared in **Fig. 5.54.**

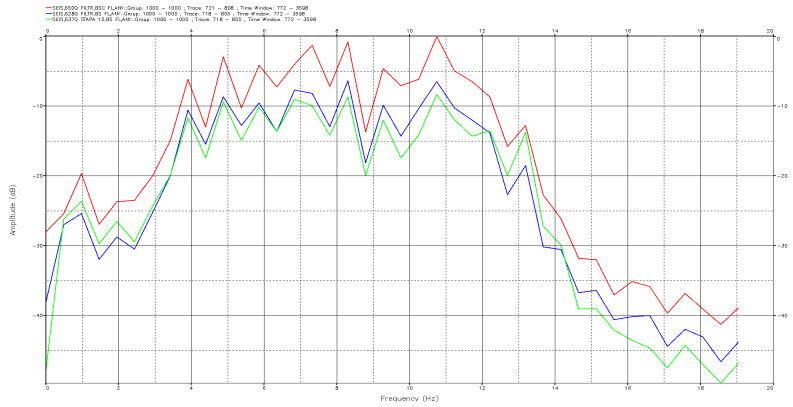

Figure 5.54 – *D1 component from all datasets. The green line (D1) and blue line (D2) correlates well. The full bandwidth representation (red) have a minor scaling difference that could have been compensated for. However, it shows consistency with the others in shapes and notches, which means that the three datasets should be quite comparable. Horizontal axis goes from 0 to 20 Hz.*

A stacked section of the post migration full bandwidth data with the velocity model included in the background is provided in **Fig. 5.55** as an attempt to express the level of resolution in the lower bandwidth data used in this processing.

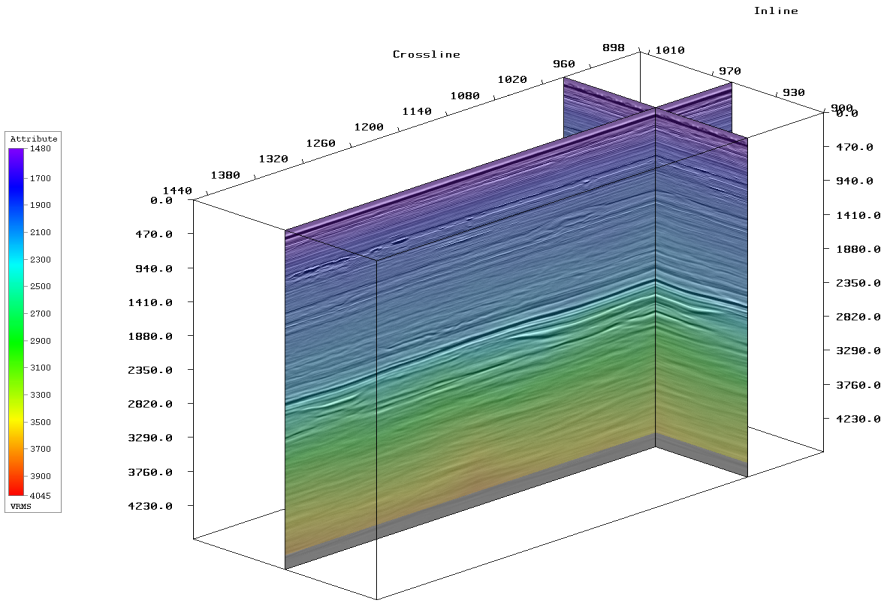

Figure 5.55 – *Full bandwidth stacked section with the velocity model that was used throughout the processing in the background.*

Observations

- Kirchhoff pre-stack time migration handles the low frequencies well, even when the input has a high-cut of 10 Hz.

Evaluation

It was not a priority to test the migration step parameter by parameter. As expected, there were no challenges of importance experienced in the process. The quality control was performed by looking at the reflector repositioning and collapses of hyperboloids. The general impression is that the data looks good and the spectrums revealed that the frequencies had been preserved. This subsection is restricted to an evaluation of the migration step in itself. A more comprehensive evaluation of the overall low frequency performance in the processing flow and the results obtained can be found in the following chapter.

Chapter 6

Discussion

Broadband acquisition and processing is now established as the premium alternative to conventional seismic in the industry. The technological frontline consists of PGS' Geostreamer, CGG's BroadSeis and WesternGeco's IsoMetrix. These companies have been able to develop their technologies due to the increasing need for high detailed images of the subsurface. While the hunt for new discoveries continue in most of the sedimentary basins that once have proved to hide hydrocarbons, the demand for innovative thinking increases for an oil company to survive. It is reasonable to assume that the majority of the classic petroleum systems in the different basins have been described and the time of the big elephants has passed. However, as the Johan Sverdrup field in the North Sea is a good example of, great value might still be hidden and could be revealed from better information. Broadband seismic is one such example of improved information and all components should be explored for full advantage of the technology. The better low frequency content is one of the major participants in the broadband success. Along with the improved low frequency data quality comes the improved resolution, penetration and inversion possibility. An interest in optimizing the information is then obvious, as it will enable the oil companies to base their crucial drill or drop decisions on a more solid basis.

At present, CGG offers BroadSeis acquisition for a 10-15 % higher price than their conventional solution. Although the general cost is higher, deeper towing can lead to less standby time, reducing the costs to even less than the described estimation. The corresponding BroadSeis processing has an approximately 20-30 % higher price than conventional processing, while broadband processing in 2 ms with BroadSource increases the price with an additional 10-15 %. The author would like to emphasize that these are only estimates that continuously varies and are depending on many factors. They indicate, however, that the total price of BroadSeis data not is far from the price of conventional acquisition and processing. Expenses related to a dry well is much higher, meaning that most of the companies will have interest of buying broadband seismic data to minimize this risk. For further development of broadband technologies, this is good

news. It also defends the topic of this thesis as the subject probably will have increased importance in future advancements.

In terms of generation of low frequencies, the limitations with the present equipment seem to be hard to overcome. The air-gun tow depth is dictated by the fundamental frequency and the ghost attenuation, but unfortunately, the two effect compensate for each other, resulting in a limited low frequency air-gun output. On land, seismic vibrators have managed to produce very low frequencies. A natural question that arise is therefore if the time has come to review other source types, also in the marine setting. The air-gun has properties that might be difficult to replace. However, one option might be to add different types of sources together or firing with a specific low frequency generator between the air-gun shots and use processing techniques to combine them. A geophysicists dream might be to construct robots with vibrators that can gather at the seafloor and emit a ghost free ideal low frequent signal. In nearer future, a further investigation of an optimal air-gun array, such as the hypercluster method, might prove valuable for the low frequencies. Even with a better source output, the signal still needs to be adequately recorded by the receiver system. Research in topics such as the superhydrophobic streamer coating and improved noise cancelling technology should be in focus. As the deepest low frequency signal is very weak, a more silent streamer environment might improve the S/N dramatically for these reflections.

One part of the seismic processing that not has been targeted much in the literature is the isolated low frequency response when subjected to the different modules. This project has attacked the low frequency behaviour in each of the processing steps with results that deserves to be discussed. An evaluation of each step was given in the previous chapter, but the overall performance and discussion around the end results will be presented here. The main deviations to the full broadband processing flow are in the denoise step, the deghosting step and the demultiple step. From the results obtained, it looks like the low frequencies can handle tougher denoising. As pointed out earlier, the S/N is often the main issue for the low frequencies. If more noise can be removed at an early stage, it has obvious advantages for the end result. Tuning of the direct wave and the seabed reflection might occur in shallow water so the low frequencies demands special attention with regards to the seabed event. This observation may provide better foundation for choosing a demultiple method, since many of the algorithms use the seabed response as input. As indicated in this thesis, the denoise algorithm may be optimized for the seabed. Using this technique, the seabed might be revealed below the unrealistic tuned first event. The data produced here show that the low frequency component of the seabed is better than in the original full bandwidth flow, but is still very limited.

Source signature shaping of the low frequency component have proved to work satisfactory, but improvements can still be achieved with a more correct signature. Much of the low frequent energy is in the bubble pulse, such that a correctly bubble model in the source signature can provided better focusing of the low frequent energy. The synthetic models often used today were made with conventional focus and the low frequency response may therefore benefit from updating these synthetic models. A better approach

will be to invest and concentrate more on near-field hydrophone measurements. With such measurements available, the low frequency behaviour does not need to be modelled and understood fully, but can be used directly to compute an accurate operator handling the shaping or deghosting process. Other ways of handling the source ghost are also a subject of interest. The apparently improved low frequency content obtained by the GWE technique on both ghosts is an observation that might help drive the industry towards non-shaping solutions. However, some shaping might be necessary to preserve a consistent phase throughout the seismic section. As experienced in the demultiple stage of the processing, the phase is a serious concern for the very low frequencies.

The SWD technique provided a good multiple model without any major adjustments. The low frequent demultiple problem was encountered when trying to adaptively subtract the model from the data. By convolving a synthetic wavelet with different frequency bands to a known reflectivity series and then perform the adaptive subtraction, the reasons for the contaminated result is believed to be understood. The representative full bandwidth modelling showed good similarities with the multiple model trace and the modelled observed trace. On the lowest bandwidth, below the multiple tuning frequency, an apparent phase rotation could be observed together with tuned amplitude fluctuations. The combined effect from these are believed to be responsible for the adaptation process to fail when finding the resemblance between multiple model and observed data. The better response obtained when including higher frequencies in the modelling and then filter down to lower frequency ranges indicate that the high frequencies are guiding the adaptation even for the lowest frequencies below multiple tuning. A split of the frequency bands into the adaptive subtraction, which has been done before, must therefore be avoided unless the input data is made to include the high frequencies. An ideal split can be to include all frequencies but only change the operators on the low frequency side to perform a milder subtraction. Better ways of finding the correspondence between the multiple model and observed trace below multiple tuning would be very beneficial for imaging of the low frequency reflectors. One idea might be to base the solution of a phase controlling process that can search for phase consistency for all frequencies located at a point in the data. If deviations are found, an attempt to correct might be done. If a consistency criteria is met, green light can be given to the subtraction. On the end point of the subtraction processes is the direct subtraction where no adaptive attempt is done. In shallow water cases with much tuning but with a solid multiple model, this might be the better solution. Test results obtained in this thesis indicate that this is the preferable solution in the Sleipner data.

The migrated stacked data was compared for the different processed frequency bands. The 10 Hz high-cut data, the below 10 Hz component of the 20 Hz high-cut data and the below 10 Hz component of the full bandwidth data were used in the comparison. The frequency spectrums of the three showed that the same frequency range was obtained. Hence, the three could be compared with each other. As expected (after making the observations in the adaptation step), the processed 10 Hz high-cut data gave results with both missing reflectors, artefacts and worse S/N than obtained from the 20 Hz high-cut

processing. This was especially demonstrated in the time slices where the 20 Hz and full bandwidth components matched very well, while the 10 Hz processed data was much more unfocused. The good performance of the 20 Hz high cut data strengthens the belief of the multiple tuning frequency being the main problem in the low frequency processing of Sleipner data. In deep water, the multiple tuning problem will vanish and the low frequency response can be expected much better. The main structures in the area were successfully imaged in all of the datasets. The way CGG have been handling the lowest frequencies up until now is therefore believed to be good. However, adjustments pointed out in this theses might provide an even better overall treatment of the low frequency content during the processing.

Chapter 7

Conclusion

Based on the results presented, a few key conclusions for low frequency processing in shallow water can be stated:

- The amount of data removed in the linear denoise procedures can be extended for the low frequencies.
- The first event is contaminated by tuning of the direct wave and the seabed reflection. Processes with a seabed wavelet input must therefore be used with special care. The linear denoise attenuation should be applied over the expected seabed for a better representation.
- Because of multiple tuning, a response below the tuning limit have amplitude and phase inconsistencies. This response is not well understood.
- The adaptation of the multiple model and input data consists of the major issue in the low frequency processing. Higher frequencies guide the adaptation, which makes an input bandwidth with frequencies above the multiple tuning frequency a requirement. A parameter split with milder adaptation on the low frequency side reduces introduced artefacts.

Chapter 8

Recommendations

Concluding this thesis, suggestions to what elements that might provide further progress in processing of low frequency data are given. Much more time could have been spent on each of the processing steps than was possible due to the obvious time limitations. From the author's point of view, special interest in three main branches might prove valuable for an even better low frequency response:

- Developing better adaptation algorithms and understand more of what can be done in cases with a high multiple tuning frequency.
- Reprocessing the full bandwidth dataset with all the low frequency recommendations from this study and to perform an inversion that can be compared to a non-optimized low frequency full bandwidth inversion. This might reveal the actual importance of the theses' findings.
- The topic of better source signatures on the low frequency side should be prioritized for future progress in deghosting and to better understand how the phase of the lowest frequencies behave.

References

Amundsen, L., 1993: Wavenumber-based filtering of marine point-source data. *Geophysics*, **58** (9), 13351348, http://dx.doi.org/10.1190/1.1443516.

Amundsen, L., B. G. Secresti, and B. Arntsen, 1995: Extraction of the normal component of the particle velocity from marine pressure data. *Geophysics*, **60** (1), 212222, http://dx.doi.org/10.1190/1.1443749.

Arntsen, B., 2011: *Geophysical Analysis Lecture Notes (course material in TPG4165).* 1st ed., NTNU.

Barr, F. J. and J. I. Sanders, 1989: Attenuation of water-column reverberations using pressure and velocity detectors in a water-bottom cable. *SEG Expanded Abstract*, 653–656, http://dx.doi.org/10.1190/1.1889557.

Beasley, C., I. Moore, D. Monk, and L. Hansen, 2012: Simultaneous sources: The inaugural full-field, marine seismic case history. *SEG Expanded Abstract*, 1–5, http://dx.doi.org/10.1190/segam2012-0834.1.

Berkhout, A., 1984: *Seismic resolution: A quantitative analysis of resolving power of acoustical echo techniques.* 1st ed., Geophysical Press, London.

Berni, A., 1985: Marine seismic system. *United State patent, no 4,520,467.*

Cambois, G., A. Long, G. Parkes, T. Lundsten, A. Mattson, and E. Fromyr, 2009: Multi-level airgun array: A simple and effective way to enhance the low frequency content of marine seismic data. *SEG Expanded Abstract*, 152–156, http://dx.doi.org/10.1190/1.3255140.

Caprioli, P., K. Özdemir, D.-J. van Manen, S. Mahat, A. Özbek, E. Kragh, and P. Christie, 2012: Combination of multi-component streamer pressure and vertical particle velocity: theory and application to data. *SEG Expanded Abstract*, 1–5, http://dx.doi.org/10.1190/segam2012-1144.1.

Carlson, D. H., A. Long, W. Söllner, H. Tabti, R. Tenghamn, and N. Lunde, 2007: Increased resolution and penetration from a towed dual-sensor streamer. *First Break*, **25** (12), 71–77.

CGG, 2013: Broadsource. http://www.cgg.com/data//1/rec_docs/2298_

12F-SV-216-V1_150dpi_BroadSource_-_Ghost-free_broadband_source_solution.pdf(accessed 24.04.2014).

CGG, 2014a: Oceanic challenger. http://www.cgg.com/data//1/rec_docs/2392_11F-AM-231-V1_150dpi_Oceanic_Challenger.pdf(accessed 15 May 2014).

CGG, 2014b: Webpage. www.cgg.com(accessed 06 June 2014).

Claerbout, J. F., 1985: *Imaging the earth's interior*. 1st ed., Blackwell Scientific Publications.

Claerbout, J. F. and S. Doherty, 1972: Downward continuation of moveout-corrected seismograms. *Geophysics*, **37** (5), 741, http://dx.doi.org/10.1190/1.1440298.

Desheng, S., Y. Ling, and X. Xiaoyu, 2009: Influential factors of post-stack seismic inversion. *International Geophysical Conference and Exposition, Beijing, China*, http://dx.doi.org/10.1190/1.3603782.

Dowle, R., 2006: Solid streamer noise reduction principle. *SEG Expanded Abstract*, 85–89, http://dx.doi.org/10.1190/1.2370392.

Dragoset, B., 2005: A historical reflection on reflections. *The Leading Edge*, **24** (s1), 46–70, http://dx.doi.org/10.1190/1.2112392.

Elboth, T., H. Hayat Qaisrani, and T. Hertweck, 2008: De-noising seismic data in the time-frequency domain. *SEG Expanded Abstract*, 2622–2626, http://dx.doi.org/10.1190/1.3063887.

Elboth, T. and D. Hermansen, 2009: Attenuation of noise in marine seismic data. *SEG Expanded Abstract*, 3312–3316, http://dx.doi.org/10.1190/1.3255547.

Elboth, T., D. Lilja, B. A. Pettersson Reif, and Ø. Andreassen, 2010: Investigation of flow and flow noise around a seismic streamer cable. *Geophysics*, **75** (1), Q1–Q9, http://dx.doi.org/10.1190/1.3294639.

Elboth, T., B. A. Pettersson Reif, and Ø. Andreassen, 2009: Flow and swell noise in marine seismic data. *Geophysics*, **74** (2), Q17–Q25, http://dx.doi.org/10.1190/1.3078403.

Elboth, T., B. A. Pettersson Reif, Ø. Andreassen, and M. B. Martell, 2012: Flow noise reduction from superhydrophobic surfaces. *Geophysics*, **77** (1), P1–P10, http://dx.doi.org/10.1190/geo2011-0001.1.

Harries, S., 2012: Reading between the lines. *GEO Ex Pro*, **9** (5), 50–52.

Hicks, E., H. Hoeber, G. Poole, and B. King, 2014: An efficient 4d processing flow for variable-depth streamer data. *The Leading Edge*, **33** (2), 172–180, http://dx.doi.org/10.1190/tle33020172.1.

Hopperstad, J., R. Laws, and E. Kragh, 2012: Hypercluster of airguns - more low frequencies for the same quantity of air. *74th EAGE Conference and Exhibition, Copenhagen*.

Huang, X., M. Kelkar, A. Chopra, and C. Yang, 1995: Wavelet sensitivity study on inversion using heuristic combinatorial algorithms. *SEG Expanded Abstract*, 1088–1090, http://dx.doi.org/10.1190/1.1887628.

Isaksen, G., R. Patience, G. van Graas, and A. I. Jenssen, 2002: Hydrocarbon system analysis in a rift basin with mixed marine and nonmarine source rocks: The south viking graben, north sea. *AAPG Bulletin*, **86** (4), 557–591, http://archives.datapages.com/data/bulletns/2002/04apr/0557/0557.htm?doi=10.1306{%}2F61EEDB48-173E-11D7-8645000102C1865D.

Kallweit, R. S. and L. C. Wood, 1982: The limits of resolution of zero-phase wavelets. *Geophysics*, **47** (7), 1035–1046, http://dx.doi.org/10.1190/1.1441367.

Kelly, S., J. Ramos-Martinez, and B. Tsimelzon, 2009: The effect of improved, low-frequency bandwidth in full-waveform inversion for velocity. *SEG Annual meeting, Houston*.

Kroode, F. t., S. Bergler, C. Corsten, J. W. de Maag, F. Strijbos, and H. Tijhof, 2013: Broadband seismic data the importance of low frequencies. *Geophysics*, **78** (2), WA3WA14, http://dx.doi.org/10.1190/geo2012-0294.1.

Kundu, P. K., 1977: *Fluid Mechanics*. 1st ed., Academic Press Inc.

Landrø, M., 2008: *Anvendt geofysikk i TPG4100 (Applied geophysics for the TPG4100 course)*. 1st ed., Norwegian University of Science and Technology (NTNU).

Landrø, M., 2011: *Seismic data acquisition and imaging (course material in TPG4190 at NTNU)*. 1st ed., Norwegian University of Science and Technology (NTNU).

Landrø, M. and L. Amundsen, 2010a: Marine seismic sources (part i). *GEO Ex Pro*, **7** (1), 32–35.

Landrø, M. and L. Amundsen, 2010b: Marine seismic sources (part iii). *GEO Ex Pro*, **7** (4), 68–72.

Landrø, M. and L. Amundsen, 2010-2011: Series on marine seismic sources (part v - part xi). *GEO Ex Pro*, **7-8**.

Landrø, M. and L. Amundsen, 2013a: Broadband seismic technology and beyond (part i). *GEO Ex Pro*, **10** (1), 78–82.

Landrø, M. and L. Amundsen, 2013b: Broadband seismic technology and beyond (part ii). *GEO Ex Pro*, **10** (2), 88–91.

Landrø, M. and L. Amundsen, 2013c: Broadband seismic technology and beyond (part iii). *GEO Ex Pro*, **10** (3), 48–52.

Landrø, M. and L. Amundsen, 2013d: Broadband seismic technology and beyond (part iv). *GEO Ex Pro*, **10** (4), 42–46.

Landrø, M. and L. Amundsen, 2014: Is it optimal to tow air guns shallow to enhance low frequencies? *Geophysics*, **79** (3), A13–A18, http://dx.doi.org/10.1190/geo2013-0348.1.

Lindseth, R., 1979: Synthetic sonic logs, a process for stratigraphic interpretation. *Geophysics*, **44** (1), 3–26, http://dx.doi.org/10.1190/1.1440922.

Loewenthal, D., L. Lu, R. Roberson, and J. Sherwood, 1976: The wave equation applied to migration. *Geophysical Prospecting*, **24** (2), 380–399, http://onlinelibrary.wiley.com/doi/10.1111/j.1365-2478.1976.tb00934.x/abstract;jsessionid=CC5F5400A02C797467086BAB1E660309.f02t04.

Lundin Petroleum, 2012: Johan Sverdrup - A New Giant in Norway. Presentation on Lundin webpage: http://www.lundin-petroleum.com/Documents/ot_JohanSverdrup_present_e.pdf (accessed 10 March 2014).

Moldoveanu, N., 2000: Vertical source array in marine seismic exploration. *SEG Expanded Abstract*, 53–56, http://dx.doi.org/10.1190/1.1816117.

Moldoveanu, N., N. Seymour, D. Manen, and P. Caprioli, 2012: Broadband seismic methods for towed-streamer acquisition. *74th EAGE Conference, Copenhagen*.

Norwegian Petroleum Directorate, 2012: Widening the range. *A Journal From The Norwegian Petroleum Directorate*, **3**, 8–11, http://www.npd.no/Global/Norsk/3-Publikasjoner/Norsk-sokkel/Nr-3-2012/Norsk_sokkel_nr_3_2012_ENGELSK_nett.pdf (accessed 10 March 2014).

Norwegian Petroleum Directorate, 2014: Well 15/9-1. http://factpages.npd.no/ReportServer?/FactPages/PageView/wellbore_exploration&rs:Command=Render&rc:Toolbar=false&rc:Parameters=f&NpdId=322&IpAddress=89.191.7.26&CultureCode=nb-no (Accessed 18 May 2014).

Özbek, A., M. Vassallo, K. Özdemir, D.-J. van Manen, and K. Eggenberger, 2010: Crossline wavefield reconstruction from multi-component streamer data: joint interpolation and 3d up/down separation by generalized matching pursuit. *SEG Expanded Abstract*, 3599–3603, http://dx.doi.org/10.1190/1.3513598.

Parkes, G. and S. Hegna, 2011a: An acquisition system that extracts the earth response from seismic data. *First Break*, **29** (12), 81–87.

Parkes, G. and S. Hegna, 2011b: The low frequency output of marine air-gun arrays. *SEG Expanded Abstract*, 77–81, http://dx.doi.org/10.1190/1.3628192.

PGS, 2011: Geostreamer gs - the ghost free solution. http://techlib.pgs.com/MediaFiles/164_TechLink_GeoStreamerGS.pdf(accessed 24.04.2014).

PGS, 2014: Ramform titan class. http://www.pgs.com/titan/(accessed 12 April 2014).

Poole, G., 2013: Pre-migration receiver de-ghosting and re-datuming for variable depth streamer data. *SEG Expanded Abstract*, 4216–4220, http://dx.doi.org/10.1190/segam2013-0541.1.

Poole, G., C. Davison, J. Deeds, K. Davies, and G. Hampson, 2013: Shot-to-shot directional designature using near-field hydrophone data. *SEG Expanded Abstract*, 4236–4240, http://dx.doi.org/10.1190/segam2013-0550.1.

Ramberg, I. B., I. Bryhni, and A. Nøttvedt, 2007: *The making of a land - Geology of Norway*. 2d ed., Norsk Geologisk Forening.

Ray, C. H. and N. A. Moore, 1982: High resolution, marine seismic stratigraphic system. *U.S Patent no 4,353,121*.

Robertsson, J. O. A., I. Moore, M. Vassallo, A. K. Özdemir, D. J. van Manen, and A. Özbek, 2008: On the use of multicomponent streamer recordings for reconstruction of pressure wavefields in the crossline direction. *Geophysics*, **73** (5), A45–A49, http://dx.doi.org/10.1190/1.2953338.

Sablon, R., T. Payen, H. Tonchia, R. Siliqi, X. Labarre, N. Salaun, and Y. Men, 2013: Ghost-free imaging combining synchronized multi-level source and variable-depth streamer. *SEG Expanded Abstract*, 72–76, http://dx.doi.org/10.1190/segam2013-0205.1.

SEG, 2006: Virtual geoscience center - biography of stephen chelminski. http://virtualmuseum.seg.org/bio_stephen_chelminski.html(accessed 12 April 2014).

Shen, H., G. Tian, T. Elboth, J. Warszawski, and D. Lilja, 2013: Theoretical study on multi-level sources. *SEG Expanded Abstract*, 61–66, http://dx.doi.org/10.1190/segam2013-0241.1.

Sheriff, R. E. and L. P. Geldart, 1995: *Exploration Seismology*. 2d ed., Cambridge University Press.

Shock, L., 1950: The progressive detonation of multiple charges in a single seismic shot. *Geophysics*, **15** (2), 208–218, http://dx.doi.org/10.1190/1.1437592.

Siliqi, R., T. Payen, R. Sablon, and K. Desrues, 2013: Synchronized multi-level source, a robust broadband marine solution. *SEG Expanded Abstract*, 56–60, http://dx.doi.org/10.1190/segam2013-0966.1.

Simm, R. and R. White, 2002: Phase, polarity and the interpreter's wavelet. *First Break*, **20** (5), 277–281, http://onlinelibrary.wiley.com/doi/10.1046/j.1365-2397.2002.00277.x/abstract.

Smith, P., J. Thekkekara, J. Branston, G. Byerley, D. Monk, and J. Towart, 2013: Towards improved time-lapse seismic repetition accuracy by use of multi-measurement streamer reconstruction. *First Break*, **31**, 73–81.

Sønneland, L., L. Berg, P. Eidsvig, A. Haugen, B. Fotland, and L. Vestby, 1986: 2d deghosting using vertical receiver arrays. *SEG Annual International Meeting, Expanded Abstracts* ***5***, 516–519.

Soubaras, R., 2012: Pre-stack deghosting for variable-depth streamer data. *SEG Expanded Abstract*, 1–5, http://dx.doi.org/10.1190/segam2012-1083.1.

Soubaras, R. and R. Dowle, 2010: Variable-depth streamer - a broadband marine solution. *First Break*, **28** (12), 89–96.

Statoil, 2014: The sleipner area. http://www.statoil.com/en/ouroperations/ExplorationProd/ncs/sleipner/Pages/default.aspx (Accessed 18 May 2014).

Tarantola, A., 1984: Inversion of seismic reflection data in the acoustic approximation. *Geophysics*, **49** (8), 12591266, http://dx.doi.org/10.1190/1.1441754.

Tenghamn, R., S. Vaage, and C. Borresen, 2007: A dual-sensor towed marine streamer: Its viable implementation and initial results. *SEG Expanded Abstract*, 989–993, http://dx.doi.org/10.1190/1.2792571.

Ursin, B., 1990: Offset-dependent geometrical spreading in a layered medium. *Geophysics*, **55** (4), 492–496, http://dx.doi.org/10.1190/1.1442860.

Wang, P., S. Ray, C. Peng, Y. Li, and G. Poole, 2013: Premigration deghosting for marine streamer data using a bootstrap approach in tau-p domain. *SEG Expanded Abstract*, 4221–4225, http://dx.doi.org/10.1190/segam2013-0225.1.

Yang, K. and B. Hung, 2012: Shallow water demultiple with seafloor reflection modeling using multichannel prediction operator. *SEG Expanded Abstract*, 1–5, http://dx.doi.org/10.1190/segam2012-0994.1.

Yilmaz, Ö., 2001: *Seismic Data Analysis*. 2d ed., Society of Exploration Geophysicists.